TRANSIENT MODEL OF PREHEATING A SUBMERGED ENTRY NOZZLE

BY

YONGHUI LI

THESIS

Submitted in partial fulfillment of the requirements
for the degree of Master of Science in Mechanical Engineering
in the Graduate College of the
University of Illinois at Urbana-Champaign, 2014

Urbana, Illinois

Adviser:

Brain G. Thomas

ABSTRACT

Adequate preheating of the submerged entry nozzle (SEN) is important to avoid problems such as thermal cracks and skulling, and depends on torch configuration, fuel, SEN geometry and other factors. A steady-state axisymmetric computational model of the flame, combustion reactions, and air entrainment has been combined with a transient model of heat transfer in the refractory walls to simulate the SEN preheating process. The model predictions match with experimental measurements of preheating with a natural-gas torch, including temperature profile across the flame, temperature histories measured inside the SEN wall, the flame shape, and the SEN outer wall temperature distribution. A Simple spread-sheet models is introduced to predict approximate flame temperature, heat transfer coefficients thermal properties, and SEN temperatures during preheating, given the air entrainment predicted from the 2D Combustion Model. Another spread-sheet model predicts SEN wall temperature histories during preheating, cool-down, and casting processes, with different temperature-dependent SEN material properties, geometries, initial conditions, and boundary conditions. The results reveal the times required to reach adequate preheating temperature and thermal patterns during each process. A parametric study of combustion during preheating found that positioning the torch at a proper distance above the SEN top, including an insulation layer and increasing refractory conductivity all increase SEN temperature and shorten preheating time.

ACKNOWLEDGMENTS

I would like to express my sincere gratitude to my research advisor, Professor Brian G. Thomas for his support, guidance and encouragement throughout this work. What I have been learning from him will definitely benefit me a lot in my future.

I would also like to thank R. Nunnington and other personnel at Magnesita Refractories for providing the measurement data, and for support from the Continuous Casting Consortium at the University of Illinois.

TABLE OF CONTENTS

Nomenclature

a: Absorption coefficient

C: Linear-anisotropic phase function coefficient

D_h: Thermal diffusivity

D_k: Mass diffusion coefficient of species k

G: Incident radiation

G_k: Generation of turbulence kinetic energy due to the mean velocity gradients

G_b: Generation of turbulence kinetic energy due to buoyancy

h: Convection coefficient

h_{in}: Internal heat transfer coefficient

h_{out}: External heat transfer coefficient

$h_k^0(T_{ref,k})$: Formation enthalpy of species k at the reference temperature $T_{ref,k}$(K)

k: Turbulence kinetic energy

$\dot{m}$: Mass flow rate

$\dot{m}_{total}$: Mass flow rate of gas mixture

$\dot{m}_{CH4}$: Mass flow rate of methane

$\dot{m}_{O2}$: Mass flow rate of oxygen

M: Molecular weight of the gas mixture

MW: Molecular weight

$\dot{n}$: Molar flow rate

$\dot{n}_{+\_O2}$: Molar flow rate of oxygen provided by entrained air

$\dot{n}_{CH4}$: Molar flow rate of methane

$\dot{n}_{O2}$: Molar flow rate of oxygen

P: Absolute pressure

P_{CH4}: Absolute pressure of methane

P_{O2}: Absolute pressure of oxygen

r: SEN radius distance in radial direction

R: Universal gas constant

R_{in}: SEN inner radius

R_{out}: SEN outer radius

S_{rad}: Radiation source term

T: Reactant temperature

T_c: Corrected thermocouple temperature

T_m: Measured thermocouple temperature

T_{CH4}: Temperature of methane

T_{O2}: Temperature of oxygen

$T_{bulk_{in}}$: SEN inner bulk temperature

$T_{bulk_{out}}$: SEN outer bulk (air) temperature

T_{in}: SEN inner wall temperature

T_{out}: SEN outer wall temperature

v_r: Velocity in radial direction

v_z: Velocity in axial direction

$\dot{V}$: Volume flow rate

$\dot{V}_{CH4}$: Volumetric flow rate of methane

$\dot{V}_{O2}$: Volumetric flow rate of oxygen

$\dot{\omega}_k$: Rate of generation of species k

Y_k: Mass fraction of gas species k

z: distance in axial direction

ρ: Gas density

μ_{eff}: Effective dynamic viscosity

ε: Turbulence dissipation energy

μ_{lam}: Laminar viscosity

μ_{tub}: Turbulent viscosity

σ: Stefan-Boltzmann constant

σ_s: Scattering coefficient

ε: Probe emissivity

Chapter 1: Introduction

Torch heating has been used extensively in industrial processes, such as the steel industry, for preheating of refractories, cutting, and scarfing. Figure 1.1 [1.1] shows a schematic of the continuous casting process. In this process, Submerged Entry Nozzle (SEN) delivers molten steel from a tundish into a continuous-casting mold. The SEN is made of different refractories, and must be preheated properly to prevent problems such as cracks from thermal shock, and freezing (skulling) of the steel during initial filling. An accurate model simulation of SEN preheating would be useful to optimize this and similar processes, which depends on fuel composition, preheating time, refractory properties and geometry, and torch configuration.

In the steel plant, a common preheating operation is to use a torch to heat up a SEN for around 2 hours. Then the SEN is transferred from the location of preheating to the caster, where it is installed under the Upper Tundish Nozzle (UTN). This stage is called the cool-down process and usually takes around 5 minutes. After that, the slide gate opens to allow molten steel to pass through it.

In the continuous casting process, clogging is caused by the buildup of non-metallic inclusions on the nozzle wall. SEN clogging decreases productivity, increases cost and decreases steel quality. Previous studies [1.2, 1.3] suggest that heat loss through the nozzle refractories may cause steel to solidify inside the nozzle, which worsens this problem In order to improve SEN quality and avoid clogging, adequate preheating is required.

For SEN preheating, a natural gas / oxygen mixture is commonly used. In this work, a comprehensive combustion model is developed and validated by measurements. In addition, the effects of stand-off distance, insulation layer, and thermal conductivity of refractory material are investigated.

In order to help users in the steel plant to understand and improve the whole process, a 1D user friendly heat transfer model system in excel spreadsheet by coding with Visual Basic Application (VBA) Macro is developed [1.4, 1.5] and has been improved [1.6, 1.7]. Adiabatic Flame Temperature Model and Heat Conduction Model are the two parts of this VBA model system.

For the Heat Conduction Model, changeable variables are refractory properties, SEN geometry, process duration (preheating, cool-down and casting) duration time, initial temperature, inner gas temperature, outer air temperature, and heat transfer coefficients. The development of the discretized governing equations is reported in Appendix A, which has been validated with FLUENT 3D transient model. The temperature dependent feature of the Heat Conduction Model is validated in Appendix B in preheating and cool down processes. Sensitivity analysis is performed for SEN steady state preheating, which is reported in Appendix C. SEN heat transfer behaviors during casting are studied by using Heat Conduction Model in Appendix D.

Figures

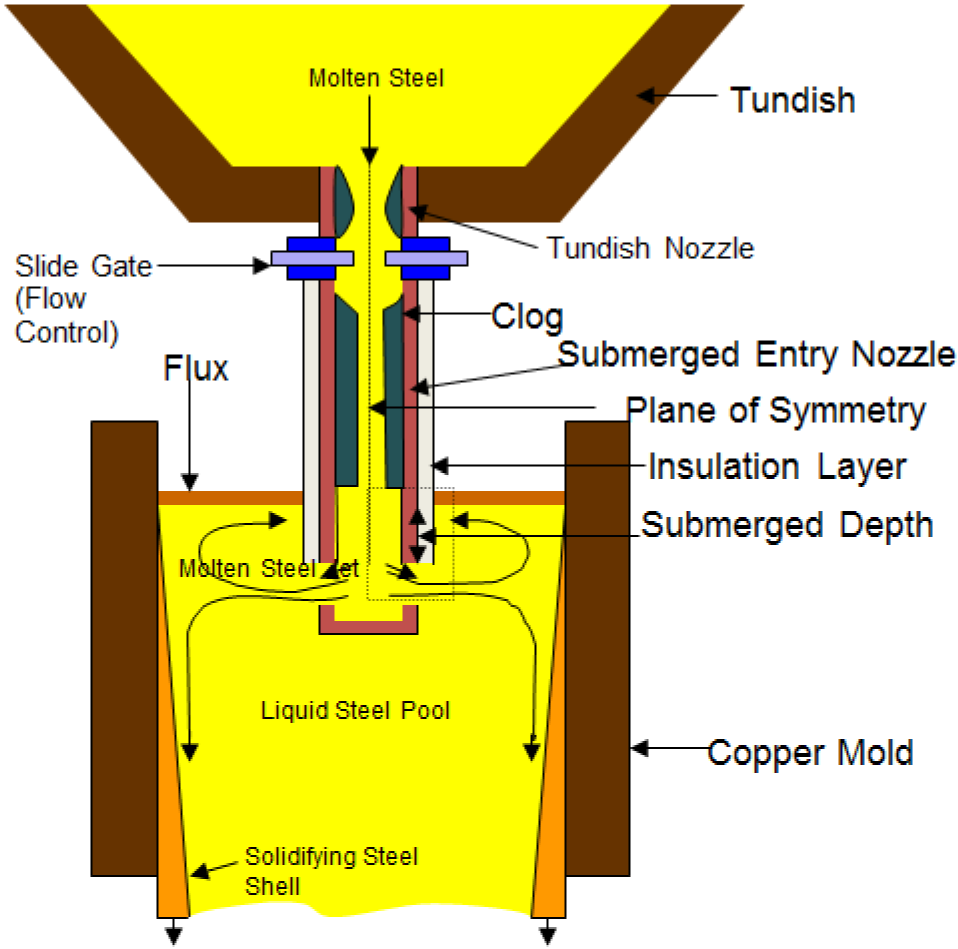

Fig 1.1 Schematic of Continuous Casting [1.1]

References

1.1 Introduction to Continuous Casting, Continuous Casting Consortium, 2014, http://ccc.illinois.edu/introduction/concast.html.

1.2 K. Rackers, Mechanism and Mitigation of Clogging in Continuous Casting Nozzles (Masters Thesis, University of Illinois, 1995).

1.3 J. Szekely and S.T. DiNovo, “Thermal Criteria for Tundish Nozzle or Taphole Blockage,” Metall. Trans., 5(March) (1974), 747-754.

1.4 V. Singh, Flame temperature VBA model, Excel software, University of Illinois at Urbana-Champaign, 2010

1.5 V. Singh, Heat Conduction VBA model, Excel software, University of Illinois at Urbana-Champaign, 2010

1.6 Y. Li, Flame temperature VBA model, Excel software, University of Illinois at Urbana-Champaign, 2014

1.7 Y. Li, Heat Conduction VBA model, Excel software, University of Illinois at Urbana-Champaign, 2014

Chapter 2: Literature Review

2.1 Fundamental research of methane and oxygen combustion

In torch heating, natural gas is a widely used fuel, often using both air and oxygen as oxygen sources for the combustion. Natural gas is mainly composed of methane, which comprises up to 94% volume fraction. Fundamental burning characteristics of methane with oxygen have been studied by several researchers, both numerically and experimentally. Research into the detailed chemical reaction mechanisms of natural gas ignition and flame has been sponsored by the Gas Research Institute (GRI), creating a comprehensive software database, GRI-Mech [2.1]. This database includes input files for another software tool, CHEMKIN^{TM} [2.2], which can be used to solve chemical equilibrium and kinetic problems, for multiple chemical species, gas concentration ranges and temperatures.

Several works have explored unconfined flames of methane / oxygen. Sreenivasan [2.3] studied unconfined methane-oxygen laminar premixed flame numerically and experimentally. Transport equations for the steady, incompressible, laminar reactive flow in axisymmetric cylindrical coordinates were discretized by the Finite Volume Method through FLUENT 6.3 [2.4] with GRI-Mech 2.11 [2.5] including 121 chemical reactions with 25 species. Predicted OH isopleths agreed with digital flame photographs, but the model over predicted measured temperature near the axis and under-predicted at farther radial locations.

Bennett [2.6] studied axisymmetric laminar co-flow diffusion flames, which are fed by non-premixed parallel input gas streams of fuel and oxygen source. Computations using a solution-adaptive gridding method with both GRI-Mech 2.11 and GRI-Mech 3.0 [2.7] chemical mechanisms predicted flame lengths, maximum centerline temperatures, radial temperatures and main species profiles that agreed well with measurements. Peak NO mass fraction predicted with

GRI-Mech 3.0 were twice as large as from GRI-Mech 2.11. Increasing the oxygen source from air to pure oxygen produced a hotter, shorter flame, even if the fuel source was diluted from 65% to 20% methane in nitrogen. This is because the hotter flame attached to the burner due to significant reactant / burner preheating. Bhadraiah [2.8] used these measurements of laminar co-flow methane-oxygen diffusion flames to compare a model with 43 combustion steps and 18 species, a model with four global reaction mechanisms, and an optically thin radiation sub-model, and had mixed findings.

For flow involving turbulent flames, Ogami [2.9] presented a numerical vortex method which incorporates chemical equilibrium, eddy-dissipation, and particle transport calculations to predict combustion of premixed methane and air. The predicted temperature and main reaction products matched with experiments. For confined combustion, Bidi [2.10] modeled turbulent premixed methane-air combustion in an axisymmetric cylindrical chamber using a chemical mechanism with 16 species and 31 reactions, and the k-ε turbulence model. Turbulent intensity was found to greatly affect flame behavior, temperature, and reaction product fractions. Silva [2.11] modeled turbulent non-premixed combustion of natural gas (methane) with air in a cylindrical chamber using the Eddy Breakup-Arrhenius model for chemical reactions, and a two-step combustion model. Compared with measurements, species mass fraction discrepancies were attributed to the preheated gases, which increased flame temperature rapidly and led to a faster consumption of reactants.

2.2 Industrial torch heating research

In addition to the above fundamental combustion studies, there is some research involving industrial torch heating, such as scarfing [2.12, 2.13], and SEN preheating. [2.14-17]. Zhou et al [2.12] developed a two-step model of heat transfer in a steel scarfing process. The model was validated with temperature measurements in the solid. It was found that the fraction of heat entering the steel from the scarfing reactions and adherent slag particles was relatively small. The heat lost by forced convection from the flame and the combustion product gases did not affect heat transfer much, relative to the scarfing reactions. Kim et al [2.13] studied the design of in-line edge scarfing nozzles by numerical analysis, using a 2D axisymmetric flow model, and species transport combustion model. The heat from the combustion gas to preheat oxygen was found to be important. Luo et al [2.14-17] modeled transient SEN temperature distributions in “combustion” and “fan type” preheating modes. Fan-type preheating was suggested to be better, in order to avoid bamboo joint shaped cracks at the neck of the nozzle.

2.3 Objectives of the Current Work

Although there are many fundamental model studies of controlled methane / air or methane / oxygen combustion flames, very few models are found of torch heating in industrial applications using realistic chemical reactions that have been validated with measurements. Thus, a combustion model has been developed in the current work to simulate torch preheating that includes methane / oxygen / air combustion and transient heat transfer in the refractory. Measured flame temperature profiles, SEN wall temperature histories, flame shape, and SEN outer wall temperatures are used to validate the computational models, which are then applied to gain new insight into torch preheating practice. In this work, the effects of stand-off distance, insulation layer, and refractory thermal conductivity on heat transfer are investigated. A user-friendly spreadsheet model system is developed to simplify the prediction of SEN preheating, cool-down, and casting.

References

2.1 Gregory P. Smith, David M. Golden, Michael Frenklach, Nigel W. Moriarty, Boris Eiteneer, Mikhail Goldenberg, C. Thomas Bowman, Ronald K. Hanson, Soonho Song, William C. Gardiner, Jr., Vitali V. Lissianski, and Zhiwei Qin Avaliable at http://www.me.berkeley.edu/gri_mech/

2.2 CHEMKIN, Reaction Design, Sandia National Laboratories, San Diego, 2013

2.3 R. Sreenivasan, An investigation of flame zones and burning velocities of laminar unconfined methane-oxygen premixed, Combustion Theory and Modeling, Vol. 16, No. 2, 2012, 199-219

2.4 ANSYS® Academic Research, Release 6.3, Software, ANSYS, Inc.

2.5 C.T. Bowman, R.K Hanson, D.F. Davidson, W.C. Gardiner Jr, V. Lissianski, G.P. Smith, D.M. Golden, M. Frenklach and M. Goldenberg, GRI-Mech Home Page, http://www.me.berkeley.edu/gri mech/flames

2.6 B. Bennett, Computational and experimental study of oxygen-enhanced axisymmetric laminar methane flames, Combustion Theory and Modeling, Vol. 12, No. 3, 2008, 497-527

2.7 G.P. Smith, D.M. Golden, M. Frenklach, N.W. Moriarty, B. Eiteneer, M. Golderberg, C.T. Bowman, R.K. Hanson, S. Song,W.C. Gardiner, Jr., V.V. Lissianski and Z. Qin, GRI version 3.0. 1999. Available online at: http://www.me.berkeley.edu/gri mech (accessed 23 March 2007).

2.8 K. Bhadraiah, Numerical Simulation of laminar co-flow methane-oxygen diffusion flames: effect of chemical kinetic mechanisms, Combustion Theory and Modeling, Vol. 15, No. 1, 2011, 23-46

2.9 Y. Ogami, Simulation of combustion by vortex method, Computers & Fluids, Vol. 39, 2010, 592-603

2.10 M. Bidi, A Numerical Investigation of Turbulent Premixed Methane-Air Combustion in a Cylindrical Chamber, Combust. Sci. and Tech., Vol. 179, 2007, 1841-1865

2.11 C. Silva, Numerical Simulation of the Combustion of Methane and Air in a Cylindrical Chamber, Vol. 5, 2006, June, 13-21

2.12 X. Zhou and B. G. Thomas, Modeling Steel Slab Heat Transfer During Scarfing Processing, Report to POSCO, Jul 2010

2.13 S. Kim and B. G. Thomas, "Design of In-line Edge Scarfing Nozzle Using Numerical Analysis", Final Report, POSCO-UIUC Joint Research, Jan 2008

2.14 H. Luo and X. Zhang, Study of preheating temperature field of submerged nozzle in burning method, Refractories, Mar 2003

2.15 H. Luo and X. Zhang, Temperature Field of Submerged Nozzle under Different Prehenating Regime, Steelmaking, Jan 2005

2.16 Y. Yang and H. Luo, Numerical Simulation of Preheating Temperature Field of Immersed Nozzle, Foundry Tech., Sep 2006

2.17 S. Liu, Temperature field of submerged entry nozzle during preheating, Steelmaking, Feb 2009

Chapter 3: Experimental Measurements

3.1 Introduction

An SEN preheating experiment was performed at Magnesita Refractories [3.1-3] which directed a turbulent flame produced from a premixed natural gas and oxygen stream downward into an SEN. In this chapter, the experimental apparatus setup, temperature measurements, and flow rate calculations are introduced. Experiment measurements are presented in Figure 3.1, 3.3, 3.4, and 3.5 and are used as validation of the combustion model.

3.2 Experimental Apparatus Setup

The entire experimental measurement system consists of:

- Tubes connected the natural gas tank and the oxygen tank to a pipe feeding the premixed gases into a burner tip;
- Flow meters in the tubes, which measure gas volume flow rate;
- Pressure gauges, which measure relative pressure in the tubes;
- W300 Rosebud burner tip supplied by ESAB19 [3.4], where the mixed gas ejects from;
- Submerged Entry Nozzle (SEN), where combustion gas in partial confined and main temperature histories are measured;
- Thermocouples, which measure gas temperature and refractory temperature;
- Data acquisition system, which collects and stores experimental data.

Flow meters and pressure gauges were installed in the tubes which connected the natural gas tank and the oxygen tank to a pipe feeding the premixed gases into a burner tip. The mixed gas ejects from a W300 Rosebud burner tip supplied by ESAB [3.4]. After traveling a short distance to the top of the SEN, and entraining surrounding air as a partially free flame, most of the combustion occurs in the confined domain inside a typical two-port SEN. The

SEN refractory is doloma-graphite (DG28XA-CT) with a 0.7mm-thick glaze layer coating on both the inner and outer surfaces of the SEN refractory to prevent oxidation. S-type thermocouples are utilized to measure the SEN wall and gas temperatures.

In Figure 3.1, the experimental set-up front view is pictured, including the flame shape during operation. In Figure 3.2, side view of the experiment setup is displayed. The burner tip is positioned 97mm above the top of the SEN, which is referred to here as the “stand-off distance”. At the burner tip, the cone-shaped flame is blue, which normally signifies high temperature and complete combustion. This flame is generated by contributions from all of the small orifices in the burner tip. As it moves downwards, the flame entrains air, cools, and extends about 300-400mm (12-16”) down the bore of SEN, based on the experimental observations [3.1].

3.3 Temperature Measurement

The gas temperature profile across the diameter of the SEN bore was measured by thermocouple No. 1, located 197mm below the top of the SEN. Figure 3.3 shows measured steady state gas temperature across the SEN inner bore. At the center of the port, gas temperature is measured by thermocouple No. 2.

As shown in Figure 3.1 and 3.2, thermocouples No. 3 and No. 5 measure temperatures inside the SEN wall at an “upper level” (197mm below the SEN top), while thermocouples No. 4 and No. 6 measure at a “lower level” (341mm below the SEN top). The temperature measurements are recorded every 10 seconds for ~115mins of this preheating experiment and ~270mins of cool-down. Figure 3.4 shows the transient SEN wall temperatures of thermocouple No. 1~6 in the preheating experiment [3.5] used to validate the Combustion model. Figure 3.5 shows an infra-red photo of the SEN outside wall, which was taken at ~50min after ignition, and is calibrated to show temperature contours.

3.4 Flow Rate and Pressure Gauge Measurement

Table 3.1 lists the flow rate and the pressure of methane and oxygen measured in the preheating experiment. SCFM means gas volumetric flow rate at standard conditions of 20 ^{o}C temperature and 101326 Pa pressure, and is transformed into actual conditions in the second column using the Ideal Gas Law. The calculated molar ratio of methane: oxygen is 5:4, which is a fuel-rich mixture, which should produce yellow or yellowish flame color, due to the excess carbon. However, the flame color observed in the experiment is blue [3.1], which indicates a high temperature and complete combustion. This was explained by reported experimental uncertainty with the flow rate measurements compared with the pressure measurements. Based on these observations, the measured methane flow rate was assumed to be too large.

Therefore, stoichiometric flow rates were assumed at the burner tip, which corresponds to a molar ratio of methane: oxygen of 1:2. Together with the Ideal Gas Law, the methane flow rate is estimated using Equation (3.1).

$$\dot{V}_{CH_4} = \frac{\dot{n}_{CH_4} P_{O_2} T_{CH_4} \dot{V}_{O_2}}{\dot{n}_{O_2} P_{CH_4} T_{O_2}} = 8.78 \times 10^{-4}\ m^3/s \tag{3.1}$$

And the oxygen flow rate is:

$$\dot{n}_{O_2} = \frac{P_{O_2} \times \dot{V}_{O_2}}{R \times T_{O_2}} = \frac{(310300 + 101325) \times 6.97 \times 10^{-4}}{8.314 \times 293.15} = 1.18 \times 10^{-1} mol/s \tag{3.2}$$

The corresponding total mass flow rate of the mixed gas exiting the burner tip is given by:

$$\dot{m}_{total} = \dot{m}_{CH_4} + \dot{m}_{O_2} = \dot{n}_{CH_4} \times 16 + \dot{n}_{O_2} \times 32 = 4.71 \times 10^{-3} kg/s \tag{3.3}$$

where $\dot{V}_{CH4}$ and $\dot{V}_{O2}$ are the volumetric flow rate of methane and oxygen respectively,

$\dot{n}_{CH4}$ and $\dot{n}_{O2}$ is the molar flow rate of methane and oxygen respectively,

P_{CH4} and P_{O2} is the absolute pressure of methane and oxygen respectively,

T_{CH4} and T_{O2} is the temperature of methane and oxygen respectively,

R is gas constant,

$\dot{m}_{CH4}$ $\dot{m}_{O2}$ and $\dot{m}_{total}$ are the mass flow rates of methane, oxygen, and total gas mixture, respectively.

Tables

Table 3.1 Experiment data flow rate and pressure [2]

	Measured flow rate (SCFM)	Measured flow rate (m^3/s)	Gauge pressure (PSI)	Gauge pressure (kPa)
O_2	6	6.97×10^{-4}	45	310.30
CH_4	7.5	2.20×10^{-3}	9	62.06

Figures

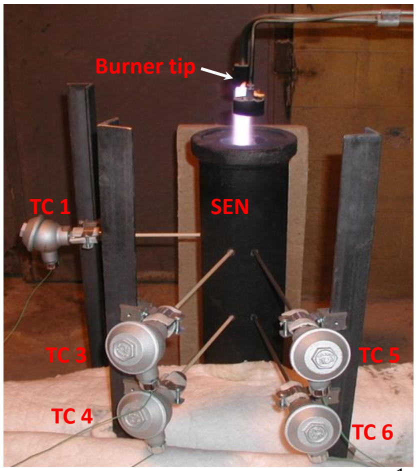

Figure 3.1 Preheating experiment setup[1] front view


Figure 3.2 Preheating experiment setup side view[1]

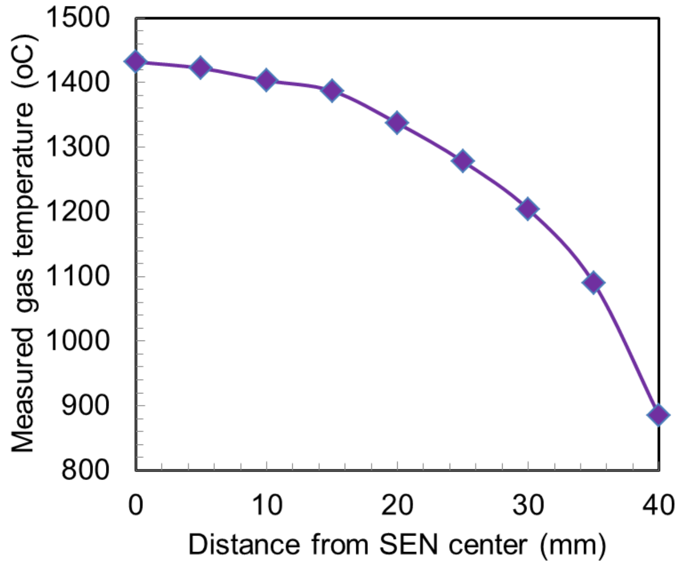

Figure 3.3 Measured gas temperature 197mm below SEN top at steady state

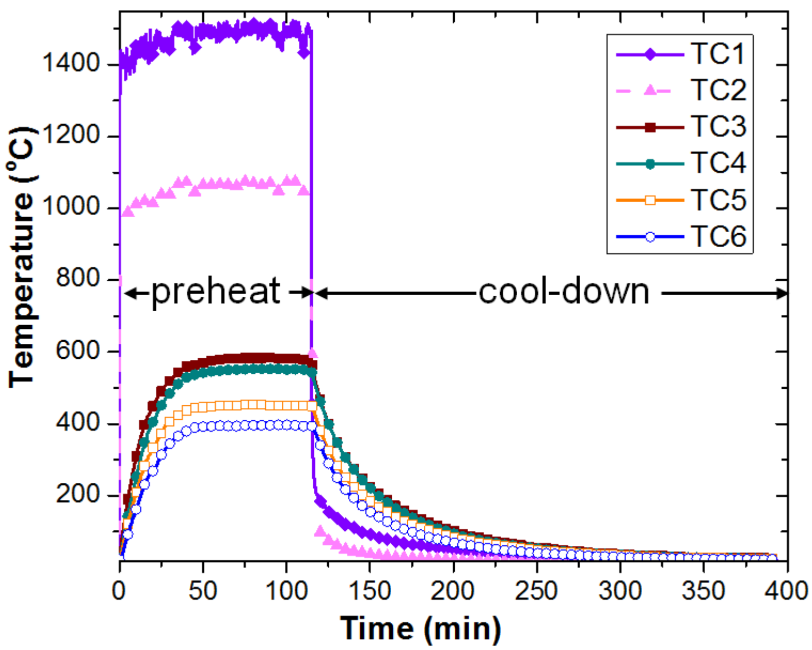

Figure 3.4 Transient temperature measurements[2]

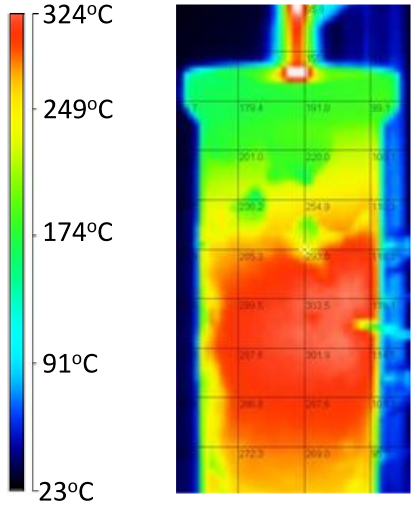

Figure 3.5 Infra-red photo of SEN outside wall[2]

References

3.1 R. Nunnington, Magnesita Refractories, private communication, Jun, Aug 2012

3.2 Magnesita Refractories, PB10 SEN Temperature Data for CCC Heat Flow Model, Report, York, March 31st, 2010

3.3 Magnesita Refractories, AG_DG thermal data_Feb 2011, Material properties measurement, 2011

3.4 ESAB welding torch W-300 Rosebud, available online at: http://esab.ca/esab/dbReplacement/pdf/17563_1143820097.pdf

3.5 Magnesita Refractories, HT_Project_Test_2_(DG28).xls, 2011

Chapter 4: Combustion Model

4.1 Introduction

A two-dimensional, axisymmetric model of non-premixed methane / oxygen / air combustion is developed for incompressible flow using FLUENT 13.0 [4.1]. The first simulation is performed to validate this model with conditions matching the experimental measurements, which include the stand-off distance of 97mm (97mm Validation Case). Then, to demonstrate a model application on torch configurations, a second simulation was performed for the same conditions, but increasing the stand-off distance to 147mm (147mm Case). And then, to demonstrate the effect of insulation layer, a third simulation was carried out for the same condition as 97mm Validation Case, but adding insulation layer at SEN outer wall (Insulated Case). At last, a fourth model was executed for the same condition as 97mm Validation Case, except using different refractory thermal properties (High-Conductivity (k) Refractory Case).

4.2 Governing Equations

The governing equations for the current 2D axisymmetric combustion model include the continuity equation (4.1), the momentum-conservation equation (4.3, 4.4), the turbulence equation (4.5-4.8), the energy conservation equation including chemical reactions (4.9-4.14), and the species transport equation (4.15).

Continuity equation:

$$\frac{1}{r}\frac{\partial}{\partial r}(r\rho v_r) + \frac{\partial}{\partial z}(\rho v_z) = 0 \tag{4.1}$$

where v_r and v_z are velocity (m/s) in the radial and axial directions, r and z. The gas density, ρ, varies pressure and temperature from the ideal gas law:

$$\rho = \frac{PM}{RT} \tag{4.2}$$

where ρ is density (kg/m^3),

M is the molecular weight of the gas mixture (kg/mol),

R is the universal gas constant (8.314 J/Kmol),

v_r is radial velocity (m/s),

v_z is axial velocity (m/s).

Axial (z) momentum conservation equation:

$$\frac{\partial}{\partial z}(\rho v_z v_z) + \frac{1}{r}\frac{\partial}{\partial r}(r\rho v_z v_r) = -\frac{\partial P}{\partial z} + \frac{1}{r}\frac{\partial}{\partial r}\left[\mu_{eff}\left(r\frac{\partial v_z}{\partial r} + \frac{\partial v_r}{\partial z}\right)\right] + \frac{1}{r}\frac{\partial}{\partial z}\left[r\mu_{eff}\left(2\frac{\partial v_z}{\partial z} - \frac{2}{3}(\nabla \cdot \vec{v})\right)\right] + \rho g \tag{4.3}$$

Radial (r) momentum conservation equation:

$$\frac{\partial}{\partial z}(\rho v_z v_r) + \frac{1}{r}\frac{\partial}{\partial r}(r\rho v_r v_r) = -\frac{\partial P}{\partial r} + \frac{1}{r}\frac{\partial}{\partial z}\left[\mu_{eff}\left(r\frac{\partial v_z}{\partial r} + \frac{\partial v_r}{\partial x}\right)\right] + \frac{1}{r}\frac{\partial}{\partial r}\left[r\mu_{eff}\left(2\frac{\partial v_r}{\partial r} - \frac{2}{3}(\nabla \cdot \vec{v})\right)\right] - 2\mu_{eff}\frac{\partial v_r}{\partial r^2} + \frac{2\mu_{eff}}{3r}(\nabla \cdot \vec{v}) \tag{4.4}$$

where P is static pressure (Pa),

μ_{eff} is effective dynamic viscosity (Ns/m^2).

Turbulent kinetic energy k:

$$\frac{\partial}{\partial z}(\rho v_z k) + \frac{1}{r}\frac{\partial}{\partial r}(r\rho k v_r) = \frac{\partial}{\partial z}\left[\left(\mu_{lam} + \frac{\mu_{tub}}{\sigma_k}\right)\frac{\partial k}{\partial z}\right] + \frac{1}{r}\frac{\partial}{\partial r}\left[r\left(\mu_{lam} + \frac{\mu_{tub}}{\sigma_k}\right)\frac{\partial k}{\partial r}\right] + G_k + G_b - \rho\varepsilon \tag{4.5}$$

Turbulent dissipation energy ε:

$$\frac{\partial}{\partial z}(\rho v_z \varepsilon) + \frac{1}{r}\frac{\partial}{\partial r}(r\rho\varepsilon v_r) = \frac{\partial}{\partial z}\left[\left(\mu_{lam} + \frac{\mu_{tub}}{\sigma_\varepsilon}\right)\frac{\partial \varepsilon}{\partial z}\right] + \frac{1}{r}\frac{\partial}{\partial r}\left[r\left(\mu_{lam} + \frac{\mu_{tub}}{\sigma_\varepsilon}\right)\frac{\partial \varepsilon}{\partial r}\right] + C_{1\varepsilon}\frac{\varepsilon}{k} - C_{2\varepsilon}\rho\frac{\varepsilon^2}{k} \tag{4.6}$$

$$\mu_{\mathrm{eff}} = \mu_{lam} + \mu_{tub}\rho C_\mu \frac{k^2}{\varepsilon} \tag{4.7}$$

$$\mu_{tub} = \rho C_\mu \frac{k^2}{\varepsilon} \tag{4.8}$$

where k is turbulence kinetic energy (kg m^2/s^2),

ε is turbulence dissipation energy (m^2/s^3),

μ_{lam} and μ_{tub} are laminar and turbulent viscosities (Ns/m^2),

G_k represents the generation of turbulence kinetic energy due to the mean velocity gradients (kg m^2/s^2),

G_b represents the generation of turbulence kinetic energy due to buoyancy (kg m^2/s^2),

σ_k, σ_ε, C_μ, $C_{1\varepsilon}$, $C_{2\varepsilon}$ are constants, 1, 1.3, 0.09, 1.44 and 1.87 respectively [4.2].

Energy conservation equation:

$$\frac{\partial}{\partial z}(v_z h) + \frac{1}{r}\frac{\partial}{\partial r}(r v_r h) = \frac{\partial}{\partial z}\left(D_h \frac{\partial h}{\partial z}\right) + \frac{1}{r}\frac{\partial}{\partial r}\left(r D_h \frac{\partial h}{\partial r}\right) + S_{rad} \tag{4.9}$$

$$h = \sum_k Y_k h_k + \frac{P}{\rho} \tag{4.10}$$

$$h_k = \int_{T_{ref,k}}^{T} C_{p,k} dT + h_k^0(T_{ref,k}) \tag{4.11}$$

$$S_{rad} = aG - 4a\sigma T^4 \tag{4.12}$$

where D_h is thermal diffusivity (m^2/s),

S_{rad} is a radiation source term (W/m^3),

Y_k is the mass fraction of gas species k,

$h_k^0(T_{ref,k})$ is the formation enthalpy (J/kg) of species k at the reference temperature $T_{ref,k}$(K),

a is the absorption coefficient (1/m),

G is the incident radiation (W/m^2),

σ is the Stefan-Boltzmann constant (5.67×10^{-8} W/m^2K^4).

P-1 radiation model has been applied, which is given by the following transport equation for incident radiation:

$$\nabla \cdot (\gamma \nabla G) - aG + 4a\sigma T^4 = 0 \tag{4.13}$$

$$\gamma = \frac{1}{(3(a + \sigma_s) - C\sigma_s)} \tag{4.14}$$

where σ_s is the scattering coefficient (1/m),

C is the linear-anisotropic phase function coefficient, set to zero value here, for isotropic scattering, which is equally likely in all directions.

Species transport equations:

$$\frac{\partial}{\partial z}(\rho v_z Y_k) + \frac{1}{r}\frac{\partial}{\partial r}(r\rho v_r Y_k) = \frac{\partial}{\partial z}\left(\rho D_k \frac{\partial Y_k}{\partial z}\right) + \frac{1}{r}\frac{\partial}{\partial r}\left(r\rho D_k \frac{\partial Y_k}{\partial r}\right) + \dot{\omega}_k \tag{4.15}$$

where Y_k is the mass fraction of species k,

D_k is the mass diffusion coefficient of species k (m^2/s),

$\dot{\omega}_k$ is the rate of generation of species k (kg/m^3s).

4.3 Model Domain, Mesh and Boundary Conditions for 4 Cases

In the experiment, the mixed gas ejects from multiple small orifices in the burner tip, where the pressure drops down to atmospheric pressure in a very short distance. To avoid the complications of locally-supersonic flow and mesh refinement problems, the model combines these two steps and simply assumes that the mixed gas exits the burner tip at atmospheric pressure, through a single, annular- shaped port with larger area of 4mm inner radius and 8mm outer radius, which is shown in Figure 4.1. The simulated area of the ports, 150 mm^2, is three times bigger than the actual, 48.7mm^2 [4.5], to account for un-modeled gas expansion through the burner tip. Moreover, the two exit ports of this bifurcated SEN are simplified as a single ring-shaped axisymmetric port in the combustion model. The SEN port area is 11102 mm^2 [6], and the assumed port length is 23mm with the 76mm outer radius. A steel can is assembled outside SEN. Due to very high heat conductivity of the steel, the can is eliminated in this model.

Figure 4.2 shows the model domain including SEN dimensions [4.6] for the 97mm Validation Case, and High-k Refractory Case. The domain has 1100 mm axial length and 400 mm radius. The commercial meshing software GAMBIT 2.4.6 [4.7] was employed to create the computational domain and to generate grids of quadrilateral cells. As shown in Figure 4.3, non-uniform grid spacing is used with finer grids near the burner tip, the SEN top, the port, and near the SEN wall and glaze layers. The minimum grid spacing is 0.25 mm in the glaze layers. (a) shows the mesh of 97mm Validation Case, which has the same mesh as High-k Refractory Case, containing 88843 cells. For the 147mm Case (b), the model domain is extended 50mm upward above the origin (z=0) in the axial direction, and contains the same number of cells. For the Insulated Case (c), the model domain is the same as 97mm Validation Case, and the mesh is finer, containing 93308 cells.

Four kinds of boundary conditions are employed in the model.

- Burner tip inlet: The boundary condition at the burner tip is defined as a mass flow inlet. The mass flow rate is calculated based on oxygen / natural gas volumetric flow rates from the measurement. The operating absolute pressure at the burner tip is 101325 Pa, and the temperature is 3104.67^{o}C. The distance from the burner tip to where the combustion starts is very short, and can be neglected in the fluid flow model. The inlet gas compositions are 33.33% methane and 66.67% oxygen, with the mass flow rate of 4.7 g/s. Emissivity of the gas mixture at the burner tip inlet is taken as 0.0351 [4.8].
- Burner side wall and SEN internal walls: Standard no slip condition for fluid flow. Heat transfer at internal walls is by conduction, which involves coupling the boundaries of the

flowing gas and solid glaze regions of the domain, and by radiation, using emissivity of 0.925[4.9].

- Domain top, bottom, and right side: All domain boundaries where air can enter or leave are defined as pressure outlets, where the oxygen mole fraction is 21.01% and the nitrogen mole fraction is 78.99%. Constant temperature 26.85^{o}C is specified at these boundaries for the atmospheric air, which entrains into or flow out of the domain. In the atmosphere, the air emissivity is very small, so emissivity 10^{-11} is chosen. The operating absolute pressure at the burner tip is 101325 Pa.
- Domain left side: This axisymmetric boundary represents the centerline axis of the SEN.

4.4 Material Properties

The temperature-dependent enthalpy of each gas species, mixture densities (PDF), specific heats of mixing, and reaction kinetics are provided via the thermodynamic database, thermo.db [4.10] file in FLUENT. The average gas viscosity 9.32×10^{-5} kg/m s and thermal conductivity 2.7006 W/m K are based on the weighted-average properties of the fuel, air and reacted gases from [4.11]. The composition-dependent absorption coefficient needed in the P1 radiation model is calculated using the weighted-sum-of-gray-gases model (wsggm). Isotropic scattering with the scattering coefficient set to zero is assumed, and the refractive index is 1. The radiation at the gas mixture burner tip is mainly non-luminous, which occurs from product species such as CO_2 and H_2O. The emissivity of the gas mixture at the burner tip (inlet) is calculated as 0.0351 [4.8], according to the calculations in References [4.8] and [4.16].

The SEN is mainly doloma-graphite with 16% porosity [4.12], but has some ZrO_2 inserted in the lower part, shown in Figure 4.2. Its inner and outer walls are coated with a glaze layerto prevent oxidation. The exterior may be insulated with kaowool flex-wrap. The densities of 16% porosity doloma-graphite, glaze and insulation are 2330 Kg/m^3, 2000 Kg/m^3, and 1920 Kg/m^3, respectively [4.14]. The glaze emissivity is 0.925[4.9]. Complete thermal properties of these solid SEN materials, density, thermal conductivity and specific heat are listed in Table 4.1 to 4.4 for doloma-graphite, glaze, and insulation, including the glaze emissivity needed for surface radiation.

4.5 Numerical Details

Combustion is modeled in this work using a turbulent, non-premixed species model with a steady flamelet state relation and non-adiabatic energy treatment. The conservation equations for mass, momentum, species and energy for steady, incompressible, turbulent reactive flow in axisymmetric cylindrical coordinates (r, z) are discretized and solved with the Finite Volume Method using the commercial computational fluid dynamic software FLUENT-ANSYS 13.0 [4.1]. A pressure based solver with operating pressure of 101325 Pa is applied. Gravitational acceleration in the axial direction (z) is included to model buoyancy effects. The standard k-ε turbulence model with enhanced wall treatment is used to describe the turbulent flow, using constants from [4.2] for turbulent flows with combustion, listing in Table 4.5. Steady laminar flamelet approach is applied to simplify the turbulent flame brush. P1 radiation model is applied. Second order upwind schemes and SIMPLE algorithm for pressure-velocity coupling are used to discretize the governing equations. To simulate natural gas combustion with oxygen and air, GRI-Mech 3.0 [4.15] natural gas combustion mechanism is applied, which is an optimized chemical reaction mechanism and best representation of natural gas flames at this time. This mechanism contains 325 reactions and 53 species. It is essentially a list of elementary chemical reactions used in calculating the species mass balances, and associated rate constant expressions for calculating $\dot{\omega}_k$. The rate constants are calculated by the modified Arrhenius equation. The convergence criterion for residual errors is 10^{-6} for the continuity, velocity, turbulence, energy and P1 radiation equations.

Tables

Table 4.1 16% porosity Doloma-Graphite thermal conductivity [4.13]

Temperature (^{o}C)	Thermal conductivity (W/m K)
26.85	10.11
226.85	7
426.85	5.23
626.85	3.84
826.85	3.2
1026.85	3.08
1226.85	3.26

Table 4.2 16% porosity Doloma-Graphite specific heat

Temperature (^{o}C)	Specific heat (J/Kg K)
25	1350
500	2210.4
750	2329.2
1000	2448
1500	2665.8

Table 4.3 Glaze thermal conductivity and specific heat [4.14]

Temperature (^{o}C)	Thermal conductivity (W/m K)	Specific heat (J/Kg K)
25	0.9	821
200	1.2	1035
550	1.67	1281
1075	1	1611
1425	0.4	1836

Table 4.4 Insulation conductivity and specific heat [4.14]

Temperature (^{o}C)	Thermal conductivity (W/m K)	Specific heat (J/Kg K)
260	0.06	1030
538	0.1	1130
816	0.14	1192

Table 4.5 Standard k-ε turbulence model constants of the Combustion Model [4.2]

Symbol / Definition	value
σ_k	1
σ_ε	1.3
C_μ	0.09
$C_{1\varepsilon}$	1.44
$C_{2\varepsilon}$	1.87
Energy Prandtl Number	0.7
Wall Prandtl Number	0.7
PDF Schmidt Number	0.7

Table 4.6 High-k Case (nearly 0% porosity) thermal conductivity and specific heat [4.14]

Temperature (^{o}C)	Thermal conductivity (W/m K)	Specific heat (J/Kg K)
25	26.5	750
500	21.8	1228
1000	17.7	1360
1500	14.6	1481

Figures

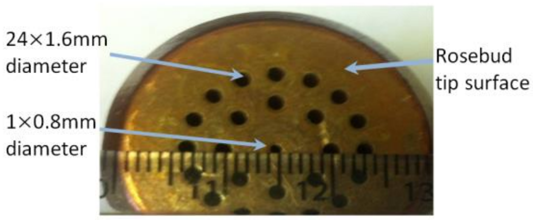

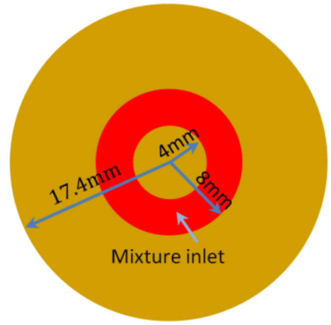

(a) photograph of W300 Rosebud tip (b) schematic of the burner used in the model

Figure 4.1 Burner tip geometry

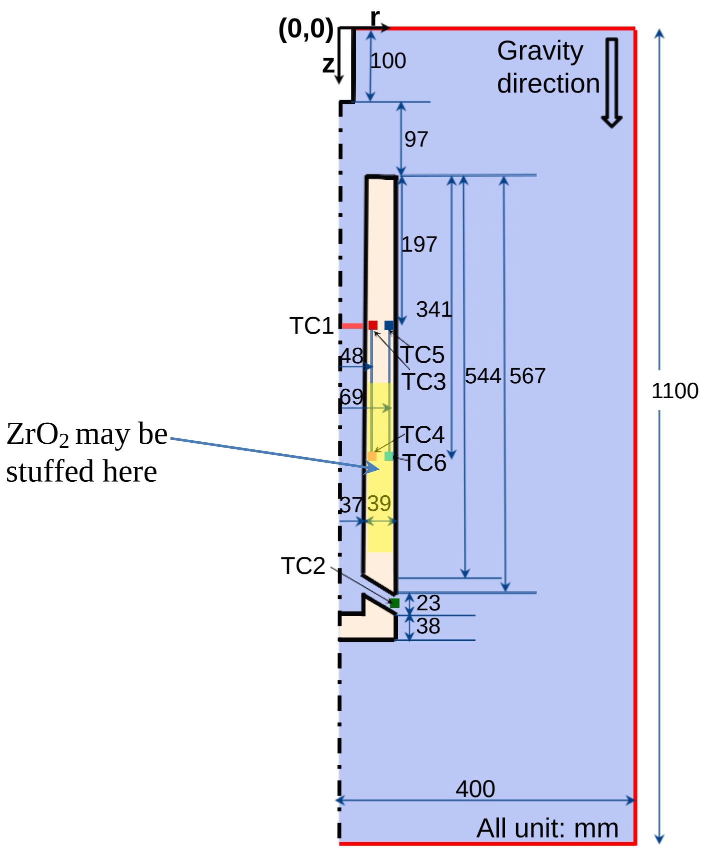

Figure 4.2 Combustion Model domain including SEN dimensions

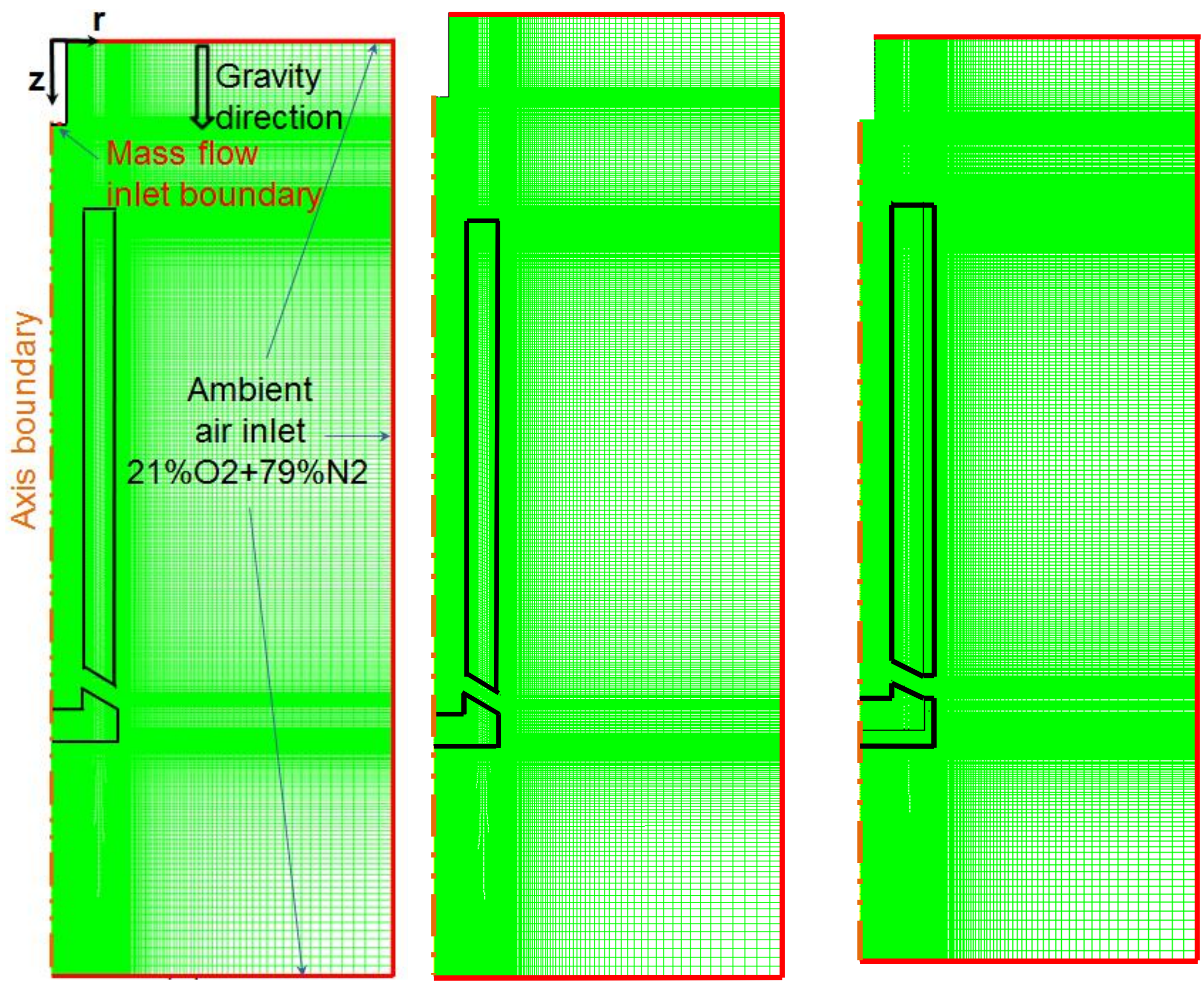

(a) 97mm Validation Case (b) 147mm Case (c) Insulated Case

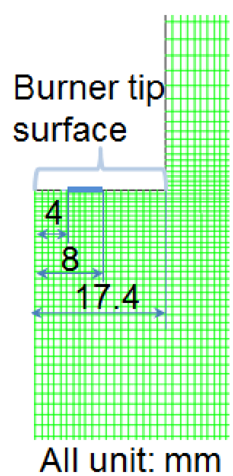

(d) zoom-in inlet

Figure 4.3 Combustion Model mesh

References

4.1 FLUENT, ANSYS Academic Research, Release 13.0

4.2 R.W. Bilger, Prog. Energy Combustion. Sci., 1, 87-109, 1976

4.3 P. Cheng. Two-Dimensional Radiating Gas Flow by a Moment Method. AIAA Journal, 2:1662-1664, 1964.

4.4 R. Siegel and J. R. Howell. Thermal Radiation Heat Transfer. Hemisphere Publishing Corporation, Washington DC, 1992.

4.5 ESAB welding torch W-300 Rosebud, available online at: http://esab.ca/esab/dbReplacement/pdf/17563_1143820097.pdf

4.6 Magnesita Refractories, HT Project Dimensions update Aug24_ 2010, blueprint and measurement, 2010

4.7 McKelvey, Richard D., McLennan, Andrew M., and Turocy, Theodore L. (2013). Gambit: Software Tools for Game Theory, Version 13.1.1. http://www.gambit-project.org.

4.8 B. Leckner, Spectral and total emissivity of water vapor and carbon dioxide, Comb. Flame, 19, 33-48, 1972

4.9 Magnesita Refractories, Emissivity Testing 9-16-11.xlsx, 2011

4.10 thermo.db, database in FLUENT, ANSYS Academic Research, Release 13.0

4.11 Charles E. Heat Transfer in Industrial combustion, p469

4.12 Magnesita Refractories, PB10 SEN Temperature Data for CCC Heat Flow Model, Report, York, March 31st, 2010

4.13 T. Shimizu, etc., Thermal conductivity of high porosity alumina refractory bricks made by a slurry gelation and foaming method, Journal of the European Ceramic Society, 2013, 3429~3435

4.14 Magnesita Refractories, AG_DG thermal data_Feb 2011, Material properties measurement, 2011

4.15 Gregory P. Smith, David M. Golden, Michael Frenklach, Nigel W. Moriarty, Boris Eiteneer, Mikhail Goldenberg, C. Thomas Bowman, Ronald K. Hanson, Soonho Song, William C. Gardiner, Jr., Vitali V. Lissianski, and Zhiwei Qin http://www.me.berkeley.edu/gri_mech/

4.16 Y. Li, Gas Emissivity Calculation Procedures, excel file, University of Illinois at Urbana-Champaign, 2014

Chapter 5: Model Validation

The Combustion Model was validated by comparing predictions of the 97mm Validation Case and Insulated Case with the corresponding experimental measurements.

5.1 Temperature across SEN

Figure 5.1 compares measured and simulated temperature profiles across SEN, including SEN inner bore, and SEN wall.

Firstly, in the nozzle inner bore, the simulated gas temperature matches the measurements, after correction with Equation 5.1. This correction accounts for the error caused by heat loss from the thermocouple junction due to radiation (to a colder environment) and the accompanying convection heat loss (due to the junction being colder). Conduction loss along the wire can be neglected for wires over 1mm long [5.1]. Equation (5.1) is used to calibrate the measurement.

$$T_c = T_m + \sigma\varepsilon T_m^4/h \tag{5.1}$$

where T_c is the corrected thermocouple temperature (^oC),

T_m is the measured thermocouple temperature (^oC),

σ is Stefan-Boltzmann constant (W/m^2K^4),

ε = 0.14 is probe emissivity (recommended for uncoated platinum Type B thermocouple),

h = 750 W/m^2K is convection coefficient for gas flowing over probe.

Secondly, temperature profiles calculated across the coated SEN wall by transient heat conduction model are compared with the measurements of thermocouples embedded in the refractory. The nozzle wall includes an “Inner Glaze” layer, the “Refractory wall” and an “Outer Glaze” layer. Due to the lower conductivity of the glaze, the temperature drops sharper at the inner and outer wall surfaces. The transient model predicts that the SEN wall heat transfer almost reaches steady state after ~50minutes of combustion preheating. The model accurately predicts thermocouples Nos.3 and 5, but over-predicts Nos. 4 and 6.

5.2 Transient Wall Temperatures

Transient temperature predictions and measurements in the SEN wall are plotted in Figure 5.2. The trends agree, but the simulation over-predicts the temperatures at thermocouple No. 3, 5, 4, and 6 by 25 ^{o}C, 32 ^{o}C, 45 ^{o}C, and 83 ^{o}C respectively. Three possible reasons could explain this slight mismatch. First, the properties of porous refractory material that contains a significant fraction of high-conductivity graphite are hard to be measured accurately. Secondly, Zirconia inserts used in the lower part of the SEN near TC4 and 6 to prevent slag corrosion, may cause lower temperature there. Thirdly, contact resistances between the thermocouple tip and the SEN wall may cause lower temperature.

A sensitivity study [5.2] in Appendix C was conducted to investigate the importance of 20 different parameters affecting the temperature distribution in the nozzle wall. From this study, the contact resistance caused by the contact-resistance gap between the tip of the thermocouple and the drilled hole in the SEN wall emerges as a likely explanation of the discrepancy between the predicted and measured temperatures.

5.3 Flame Shape

Thirdly, the predicted flame shape is compared with a close-up of the experimental flame photo in Figure 5.3. The 1600 ^{o}C temperature contour line lies on the flame rim in the photo, and shows that the predicted and observed flame shapes roughly match, although the prediction exhibits slightly more expansion along the length of the flame above the SEN.

5.4 SEN Outer Wall Temperature

Finally, Figure 5.4 compares the predicted SEN outer wall temperature contours with the infra-red photo. Both images show the same region of the SEN outer wall from the top of the SEN to 360mm below the top. The temperature contours show similar trends, where the lower region (~150mm to ~320mm below SEN top) is hotter, due to reattachment of the flame inside the nozzle. Quantitatively, the model over predicts the outer wall temperatures by ~150° C.

Overall, for the 97mm Validation Case, the model predictions are very consistent with the measurements, so the model is reasonably-well validated.

5.5 Insulated Case

Another experiment was performed with all the same conditions, except the SEN was wrapped with 6mm thick insulation at outer wall. The insulation material properties are listed in Table 4.4. The insulation layer emissivity is 0.855[5.3]. Figure 5.5 shows simulated temperature across SEN, including SEN inner bore, SEN wall, and insulation layer, comparing 2D Combustion-Model predictions and measurements at 2-hour, and also showing predictions after 4-hour of preheating. The simulation matches well with the measurements at TC 3 and 4 at 2-hour, but over predicts temperature at thermocouple Nos. 5 and 6 by 42 ^{o}C, and 143 ^{o}C respectively. From the sensitivity study in Appendix C, the contact resistance caused by the contact-resistance gap between the thermocouple tip and the drilled hole in the SEN wall emerges as a likely explanation of the discrepancy.

Figure 5.6 shows SEN wall transient temperatures comparisons between the model predictions and the measurements. The model predictions show a relative constant heating up rate compared with the measurements. From the beginning of the preheating to ~45mins, the measurements show a faster heating up rate, which is equivalent to the heat flux, and from

~45min to the end of the preheating, the measurements show a slower heating up rate. Several possible reasons could explain this mismatch during transient stage, such as insulation thermal properties inaccurate measurements, and possible issues with the radiation model. For example, the Combustion Model assumes constant emissivity for the inner and outer surfaces of the SEN. However, the emissivity is temperature dependent in the experiment.

Figures

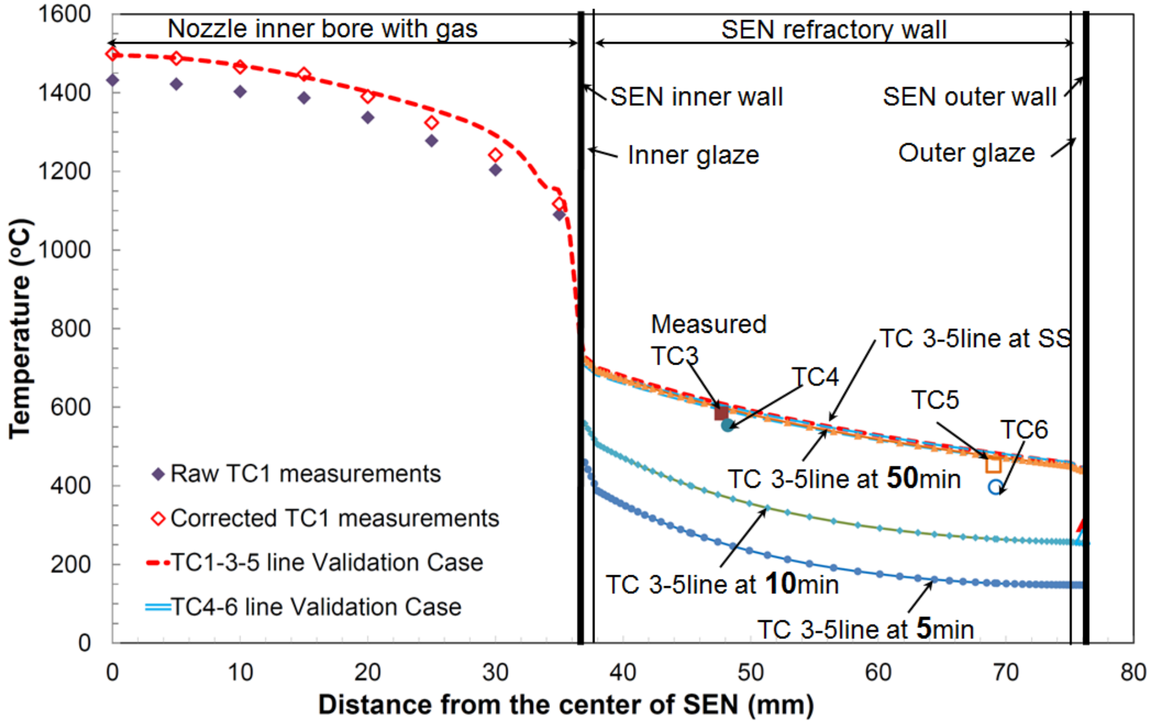

Figure 5.1 Temperature comparisons across the SEN in 97mm Validation Case

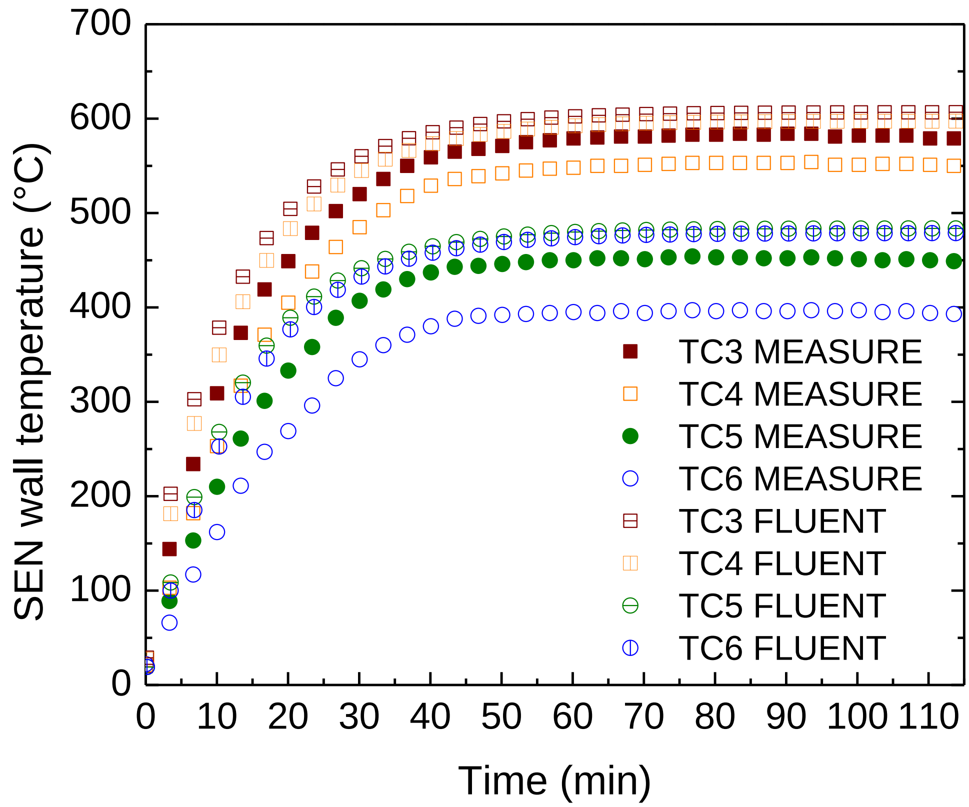

Figure 5.2 SEN wall temperature comparison between
Combustion Model (FLUENT) and measurement in 97mmValidation Case

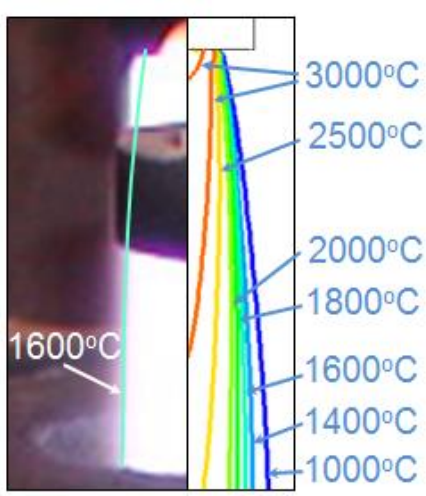

Figure 5.3 Flame shape comparisons of predicted temperature contours
and the close-up photograph in 97mm Validation Case

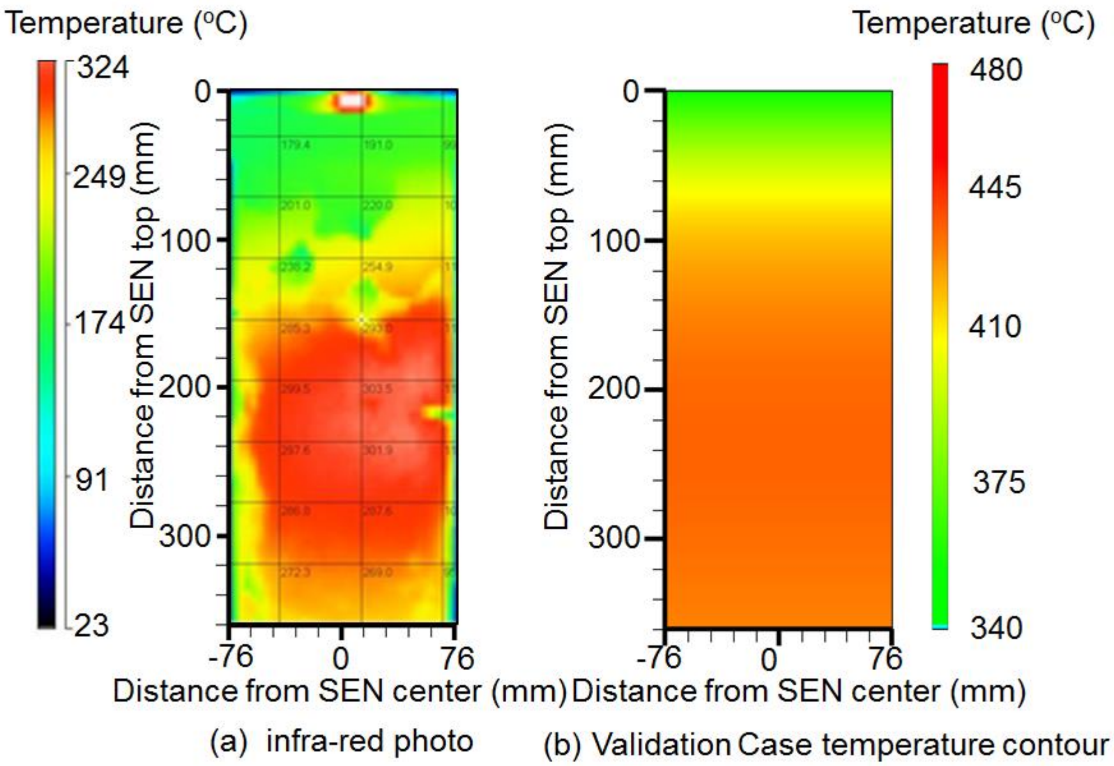

Figure 5.4 SEN outer wall temperature comparison of temperature contour and the infra-red photo in 97mm Validation Case

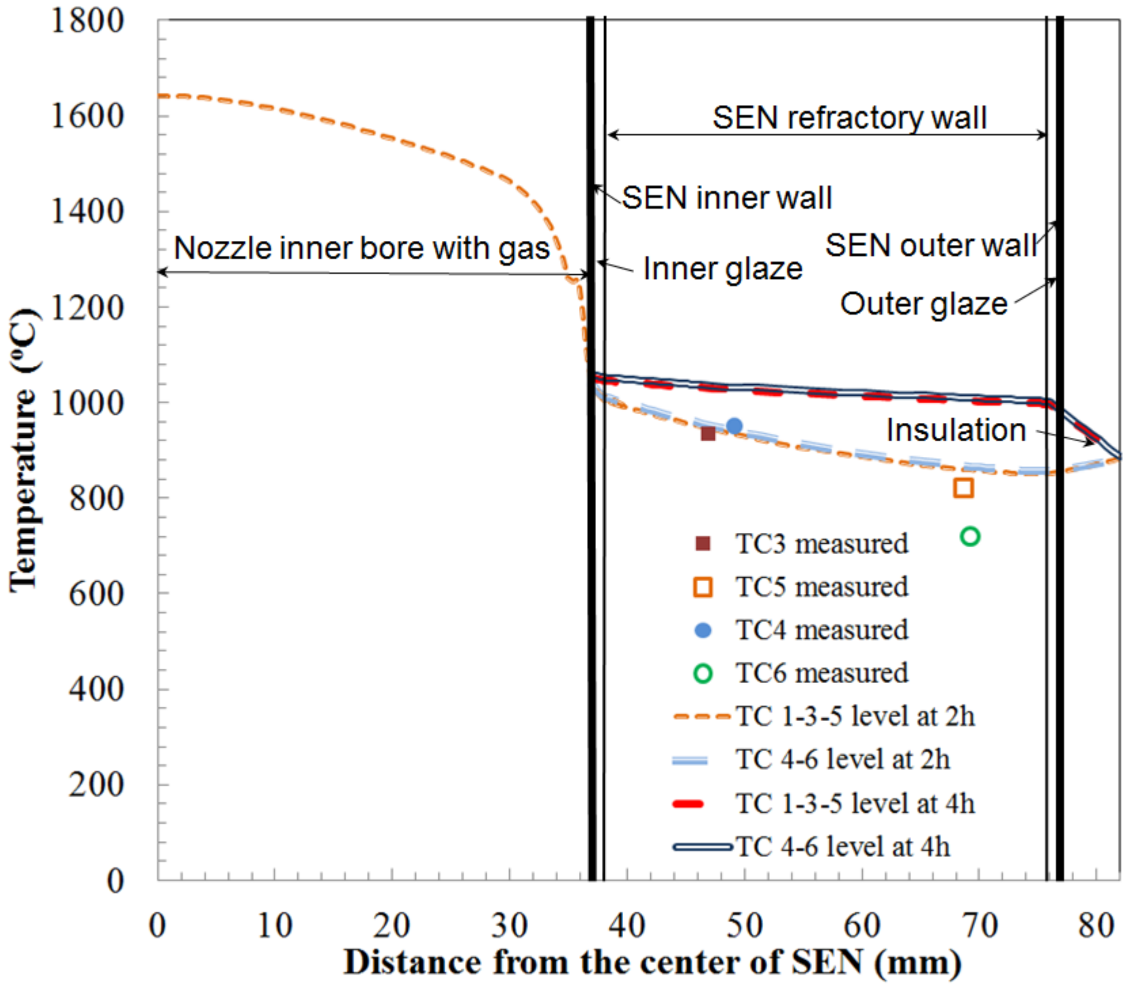

Figure 5.5 Temperatures comparison across the SEN in Insulated Case

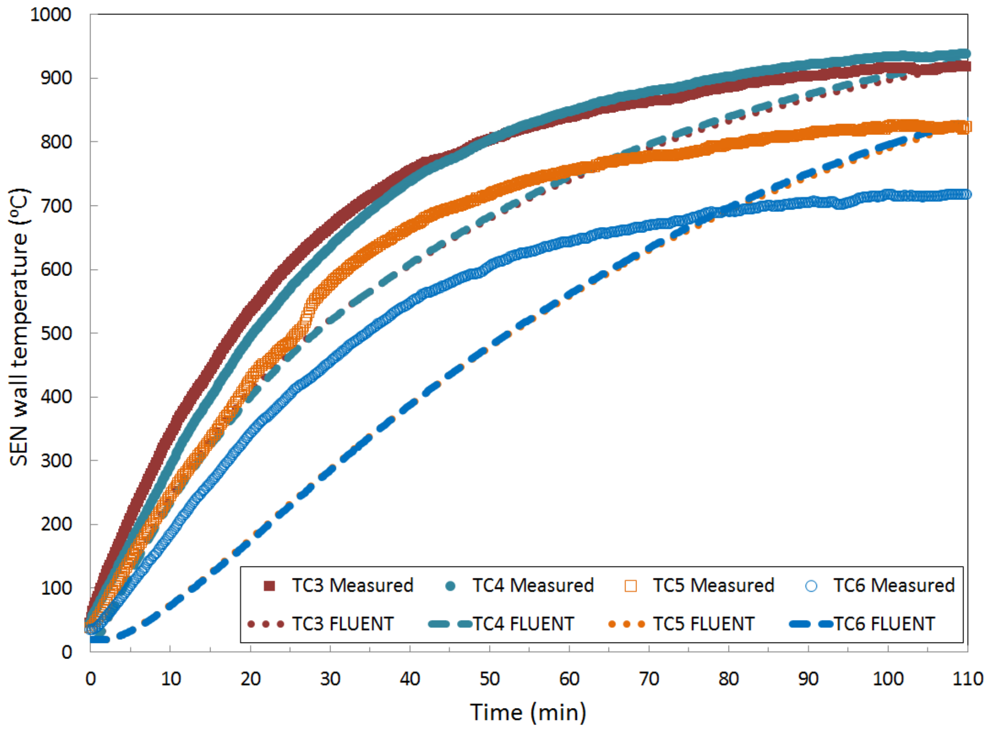

Figure 5.6 SEN wall transient temperature comparison between Combustion Model predictions and the measurements in Insulated Case

References

5.1 D. Bradley and K. J. Matthews, Measurements of high gas temperatures with fine wire thermocouples, J. Mech. Eng. Sci. 10(4), 299-305, 1968

5.2 Y. Li, Sensitivity Analysis Report of Preheat Process in SEN Nozzle at Steady State, University of Illinois, Aug 2011

5.3 Magnesita Refractories, Emissivity Testing 9-16-11.xlsx, 2011

Chapter 6: Results and Discussion

Further results from the validated model are presented: species concentration, fluid flow, gas temperature and SEN temperature. Then, a parametric study of three new cases is performed to investigate the effects of increasing the nozzle stand-off distance above the SEN, the addition of an insulation layer, and an increase of the thermal conductivity of the refractory wall material, comparing the 97mm Validation Case, 147mm Case, Insulated Case and High-k Case. Table 6.1compares the different model inputs for each case.

6.1. Species Concentration

For the 97mm Validation Case, mole fraction contours of the main species are shown in Figure 6.1. Oxygen mole fraction (a) is 67% at the burner tip inlet boundary, defined by the stoichiometric gas / fuel mixture. As combustion progresses, oxygen and CH_4 are consumed and almost depleted in the flame, as shown in (c). However, entrained air drawn into the SEN top via the Venturi effect diffuses and causes oxygen to increase to 13%~20% further down the nozzle. Nitrogen fraction (b) also indicates the effect of the entrained air. Although there is no nitrogen at the burner tip, the air drawn into the SEN increases Nitrogen to over 50%, which distributes evenly by diffusion towards the SEN bottom. Carbon monoxide fraction (d) increases in the flame region during combustion to a maximum of 15% in the flame just above the SEN. Carbon dioxide fraction (e) increases to almost 6% and then decreases, initially in a similar manner to CO. As the flame expands and air is entrained, products such as CO, CO_2, and H2O become diluted with distance down the SEN, as indicated by their decreased mole fractions. Towards the SEN bottom, the gas temperature decreases, which causes CO to transform into CO_2. Thus, the CO_2 mole fraction increases towards the SEN bottom. Water fraction (e) increases during combustion to reach a maximum of 19% above the SEN top. It decreases due to diffusion and air dilution but later increases slightly towards the SEN bottom as other non-equilibrium products such as H, OH and H_2 finally near completion of their oxidation reactions. The species contours evolve in a similar manner for the other 3 cases.

6.2 Fluid Flow Results

Figures 6.2 shows velocity vectors for all four cases. The flow exiting from the burner tip is always the fastest, due to the rapid expansion that accompanies combustion. The fast jet flow into the top of the SEN entrains air from the surroundings. As turbulent flow diffuses the jet momentum, the velocity profile across the nozzle becomes more uniform with distance down the SEN.

Direction arrows (a) in the whole domain show the flow directions of entrained air, especially at the top, bottom and right side boundaries. For the 3 cases with 97mm stand-off distance, the air enters into the domain vertically at the top boundary, and changes direction towards SEN inner-wall gradually due to the Venturi effect. In 147mm Case, the increased stand-off distance changes the gas flow distribution, especially the entrainment of air. The flame spreads more before entering the SEN, so less air is entrained. But, some air outside the SEN near the outer wall is drawn upwards and continues to flow upward past the torch. Below the SEN, flow is generally downwards, except for the Insulated Case, which has a stronger jet that causes reversed flow beneath the SEN. The mesh has been made finer in the Insulated Case, than the other three cases. It is possible that this may change the shape of the jet exiting the nozzle in this case. This shows how these results are very sensitive. Velocity vectors inside the SEN (b) show that the velocity of the entering entrained air is much smaller than the fuel stream velocity near the burner, which decreases to ~60m/s by lower in the SEN. In both figures, zoom-in vectors near the SEN top (c) show how the flow near the SEN top changes according to the entrained air flow, as it enters the high-velocity flame.

6.3 Gas Temperature

Figures 6.3 (a), (b), (c) and (d) show gas temperature profiles across the SEN inner bore at different distances below the SEN top for the 97mm Validation Case, 147mm Case, Insulated Case, and High-k Refractory Case, respectively. For all cases, the temperature drop across the SEN from the center to the inner wall is the largest at the SEN top, where cold air drawn into the top edge of the SEN causes lower temperature near the SEN inner wall. With distance down the SEN, however, the gas temperature near the wall increases due to radiation from the hot inner gases. As the gases mix, temperature profiles flatten with distance down the SEN. Towards the lower part of the SEN, some heat is released due to delayed combustion of CO into CO_2, especially towards the walls where there is slightly more oxygen, due to the air entrained down the inside walls. Thus, the average temperature at 341mm below SEN top at TC4-6 is slightly increased.

Compared with the 97mm Validation Case (a), the 147mm Case (b) shows slightly lower temperature entering the center of the SEN top because the flame is colder with the farther stand-off distance. Inside the SEN, however, the 147mm Case shows higher and more uniform gas temperatures, owing to less air entrainment and heat lost to that air, as discussed in detail in the next section.

Compared with the 97mm Validation Case (a), the Insulated Case (c) shows overall higher gas temperatures, due to less heat loss through the SEN wall.

Near the SEN inner wall, the High-k Case (d) shows similar gas temperatures with the 97mm Validation Case (a). However, the higher refractory conductivity means lower thermal resistance through SEN wall, which increases heat losses through the SEN wall. Therefore, near the SEN inner wall, the gas temperatures show slightly sharper temperature gradient.

6.4 SEN Temperature

Figure 6.4 shows temperature contours in the whole domain. For all four cases, the upper part of the SEN wall temperature is low, until the flame jet spreads enough to touch the SEN inner wall. After the flame diffuses and impinges the inner wall, the lower part of the SEN wall is heated greatly. Figure 6.5 shows a close-up of the temperature contours from the burner tip to the SEN bottom. For the 97mm Validation Case, temperature contours (a), show the hottest temperature is 3229 ^{o}C at 26mm below the burner tip, and gas temperature at the port center drops to 927 ^{o}C. For the 147mm Case (b) temperature is higher everywhere. Because the flame jet from the burner tip travels a longer distance before entering the SEN, it spreads to almost fill the SEN diameter, which reduces the air entrainment from 154% to 135%. This lessens the heat lost to heating that air. Owing to its strong effect on air entrainment, the flame shape entering the SEN is very important to temperature inside the SEN and thus to preheating efficiency.

For Insulated Case (c), the SEN wall temperature mostly stays ~1000 ^{o}C. At the TC 1-3-5 level, the temperature sudden drops from 1027 ^{o}C at insulation inner wall to 890 ^{o}C at insulation outer wall. TC1-3-5 level means the vertical distance from the SEN top to the horizontal line through TCs 1, 3, and 5. The High-k Case (d) shows a similar temperature distribution as 97mm Validation Case.

The goal of preheating the SEN is to prevent cracks caused by thermal shock during the initial stages of casting. This requires heating to as close to steel temperature (over 1500 ^{o}C) as fast as possible. This parametric study shows that all three effects investigated help towards these goals. Choosing a stand-off distance such as the 147mm Case that achieves optimal flame spreading lowers air entrainment and increases SEN temperature everywhere; adding an insulation layer lowers heat loss and keeps SEN wall temperature higher (~1000 ^{o}C); high refractory conductivity decreases the temperature gradients and lessens the danger of thermal shock during casting. From a practical view, a SEN positioned at a proper stand-off distance from the torch, with proper refractory conductivity, and wrapped with insulation layer optimize SEN preheating process.

Figure 6.6 compares the transient temperature histories of the 97mm Validation Case, 147mm Case, and High-k Refractory Case.

In Figure 6.6, for two stand-off cases, the SEN reaches steady state after ~ 60min for both cases. However, moving up the burner from 97 to 147mm above the SEN top, increases wall temperature by ~ 600 ^{o}C on average.

Figure 6.6 shows that the SEN in the High-k Refractory Case reaches steady state after ~30min, while 97mm Validation Case (lower conductivity refractory) takes about 2 times longer to reach steady state. This is expected, owing to the higher diffusivity which controls the heat-up rate. The higher conductivity causes higher heat losses through the SEN walls, which lowers steady temperatures. For the same reason, the High-k Refractory Case shows less than half of the temperature differences between TC3 and TC5 than 97mm Validation Case. The measurements in Figure 6.6 are from the measurement with 97mm stand-off distance without insulation layer. 97mm Validation Case simulates the best match with the measurement.

Tables

Table 6.1 Differences in model inputs of four cases

Model Inputs	97mm Validation Case	147mm Case	Insulated Case	High-k Case
Thermal conductivity	Table 4.1	Table 4.1	Table 4.1&4.4	Table 4.6
Specific heat	Table 4.2	Table 4.2	Table 4.2&4.4	Table 4.6
Stand-off distance	97mm	147mm	97mm	97mm
Insulation layer	No	No	Yes	No

Figures

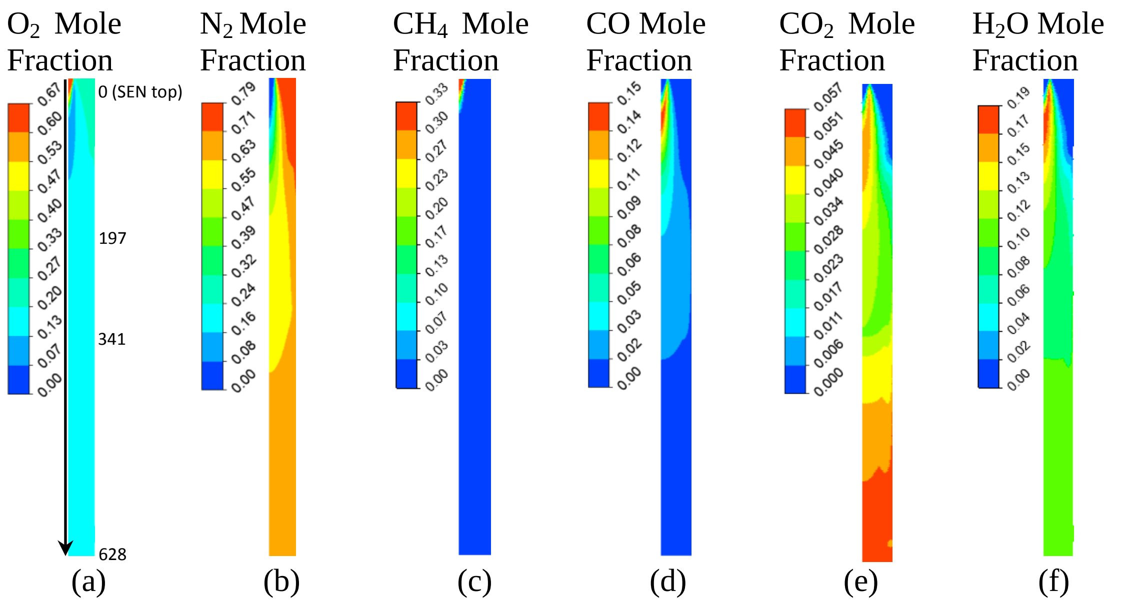

Figure 6.1 Mole fraction contours of main species (97mm Validation Case)

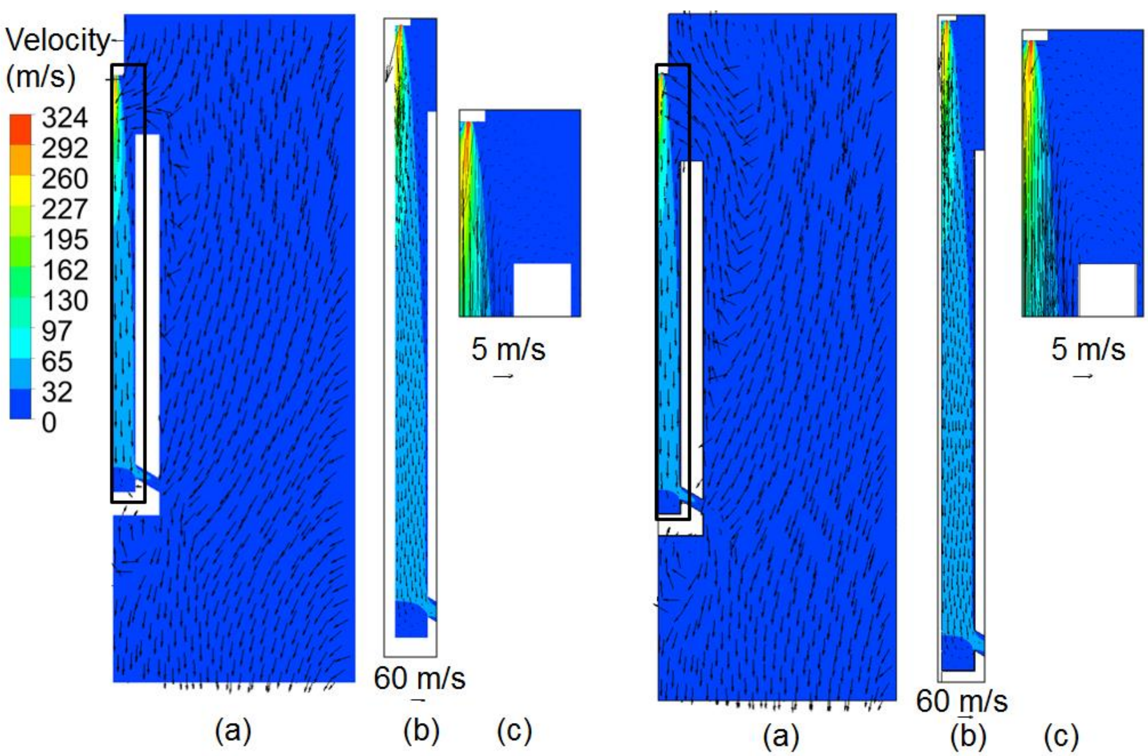

97mm Validation Case

147mm Case

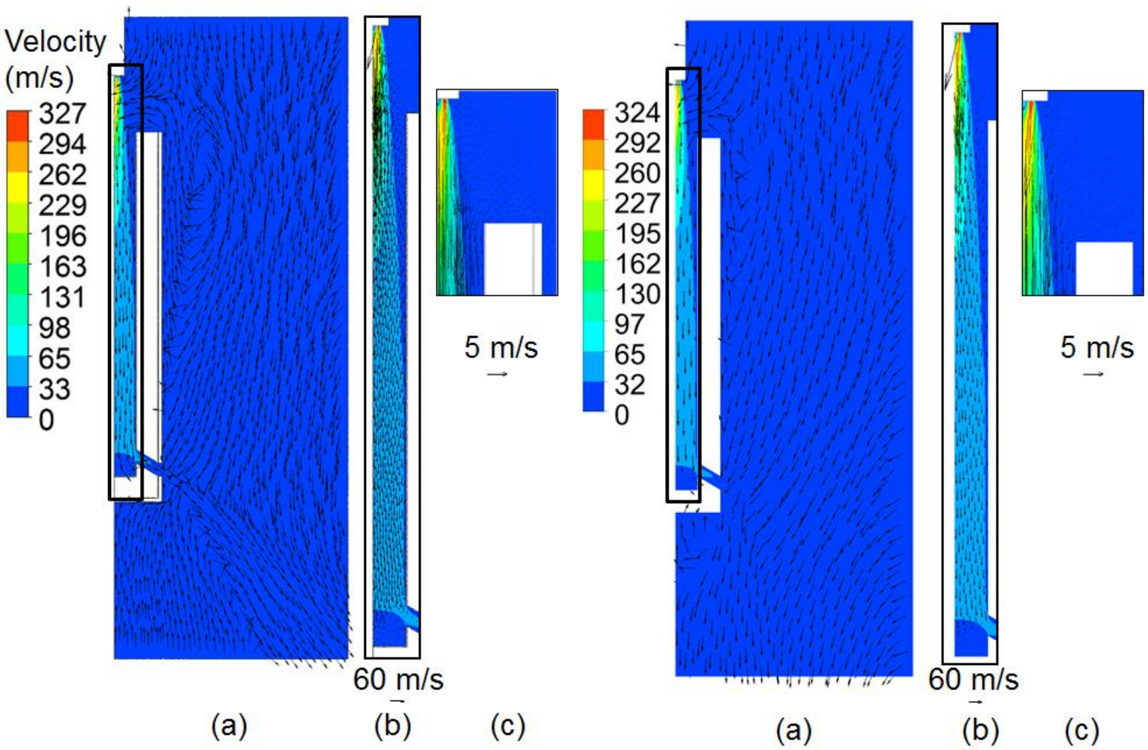

Insulated Case High-k Refractory Case

Figure 6.2 Flow pattern (a) direction arrows in the whole domain
(b) velocity vectors inside SEN
(c) zoom-in vectors near SEN top

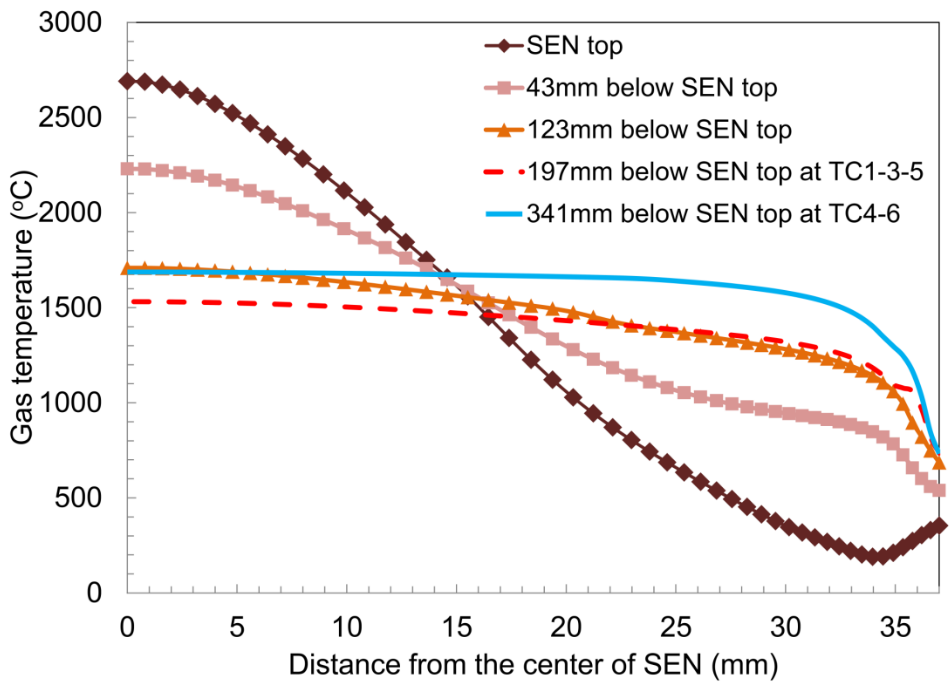

Figure 6.3 (a) Gas temperature profiles across SEN inner bore in 97mm Validation Case

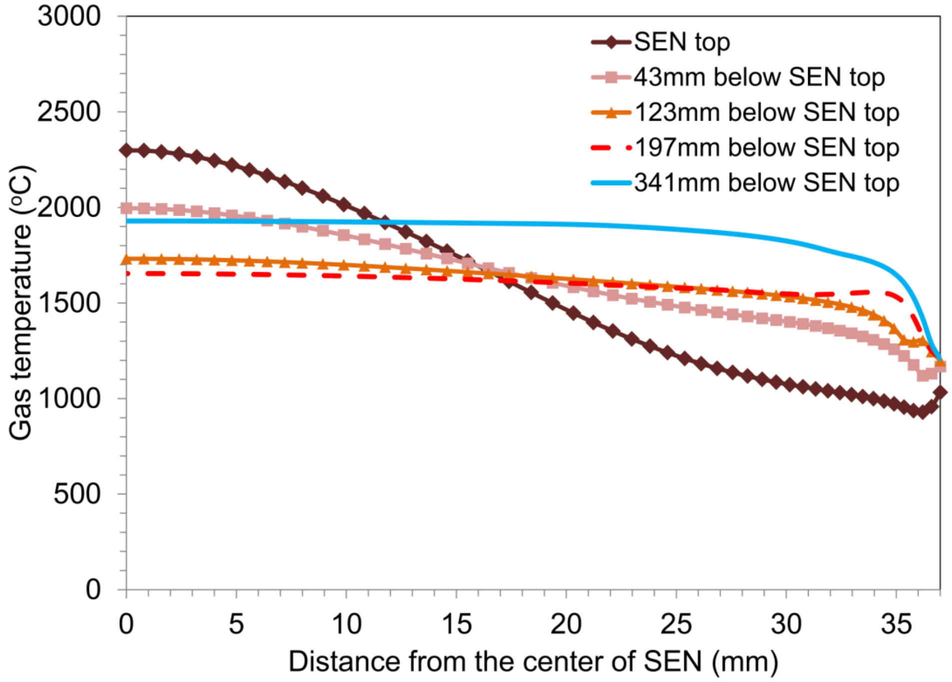

Figure 6.3 (b) Gas temperature profiles across SEN inner bore in 147mm Case

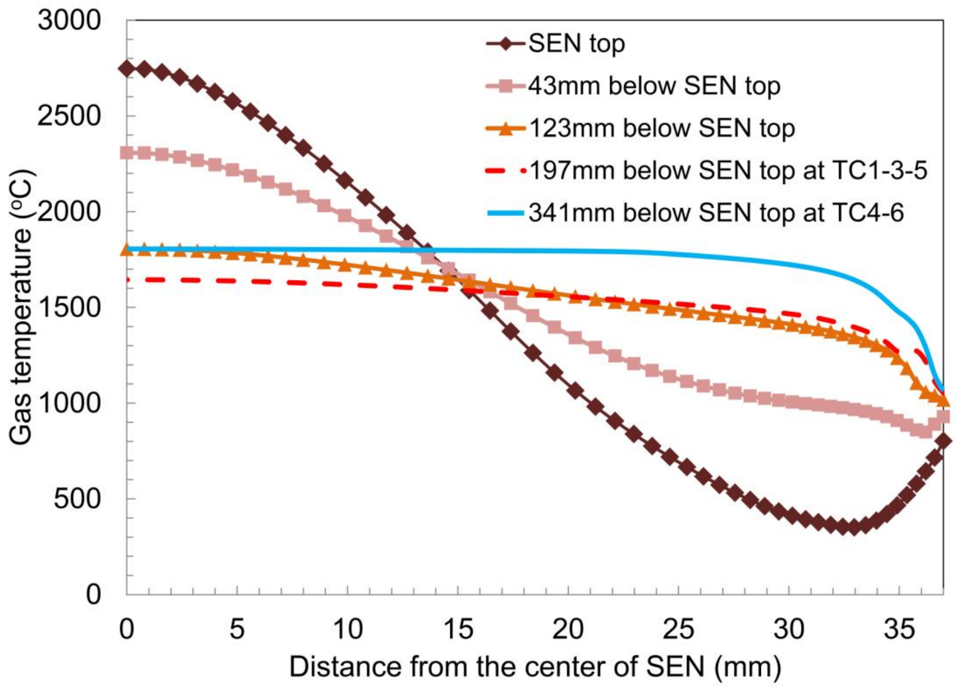

Figure 6.3 (c) Gas temperature profiles across SEN inner bore in Insulated Case

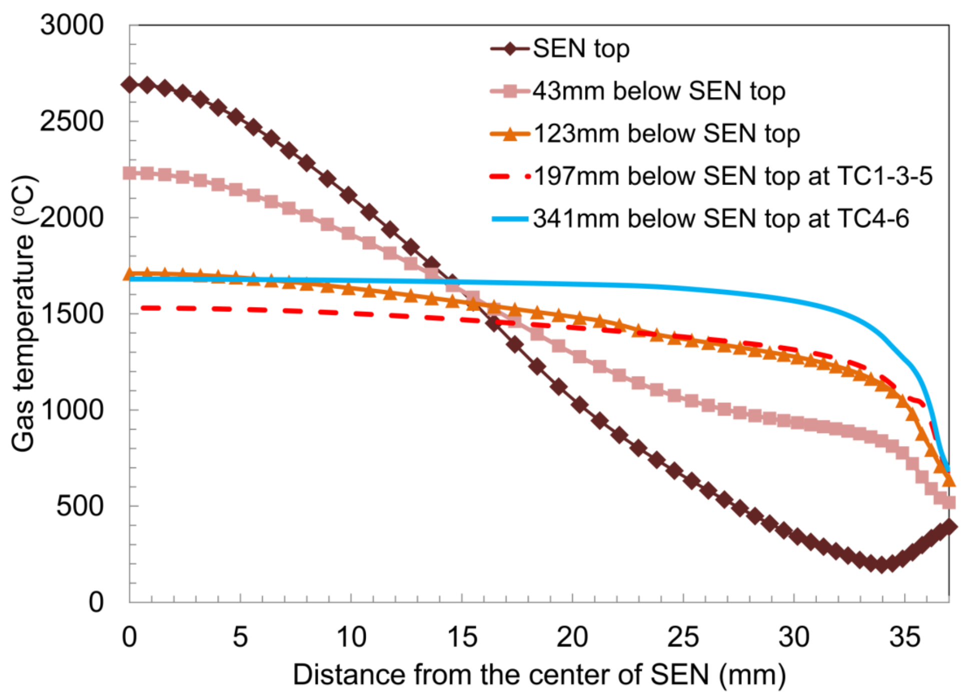

Figure 6.3 (d) Gas temperature profiles across SEN inner bore in High-k Refractory Case

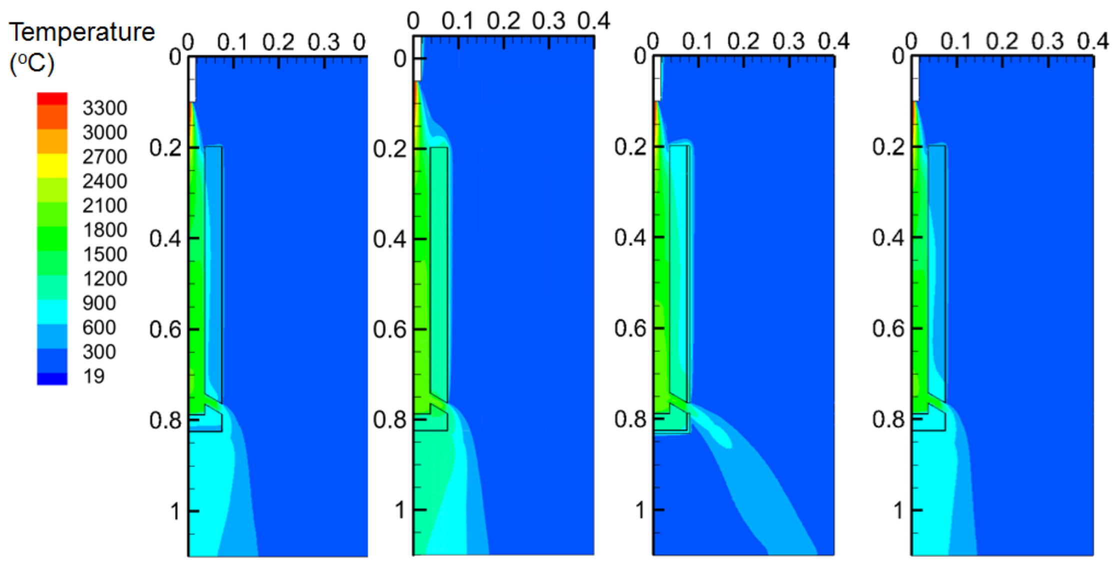

(a) (b) (c) (d)

(a) 97mm Validation Case
(b) 147mm Case
(c) Insulated Case
(d) High-k Refractory Case

Figure 6.4 Steady-state temperature contours

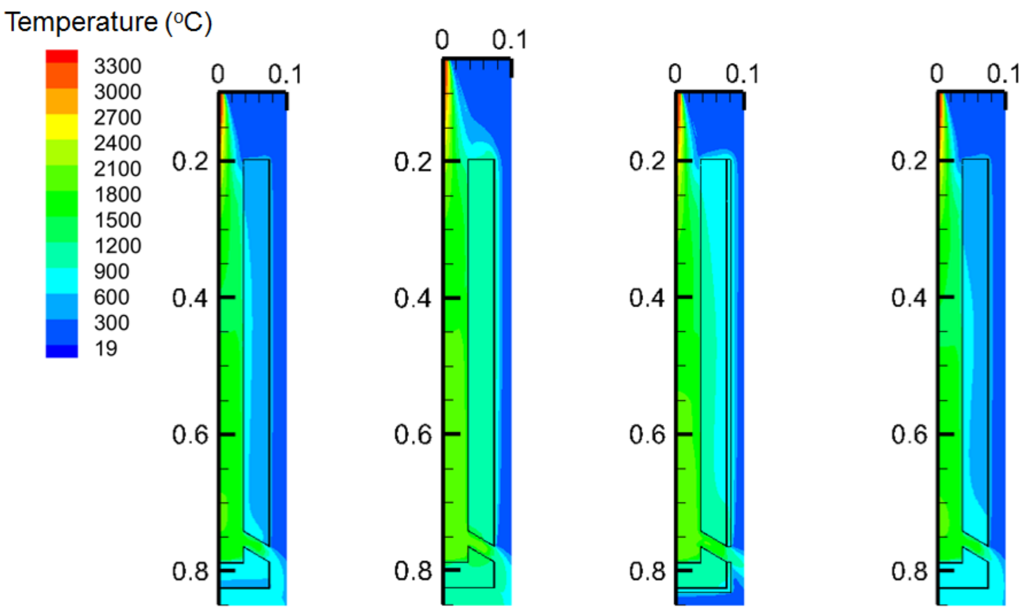

(a) (b) (c) (d)

(a) 97mm Validation Case
(b) 147mm Case
(c) Insulated Case
(d) High-k Refractory Case

Figure 6.5 Zoom in temperature contour in steady-state

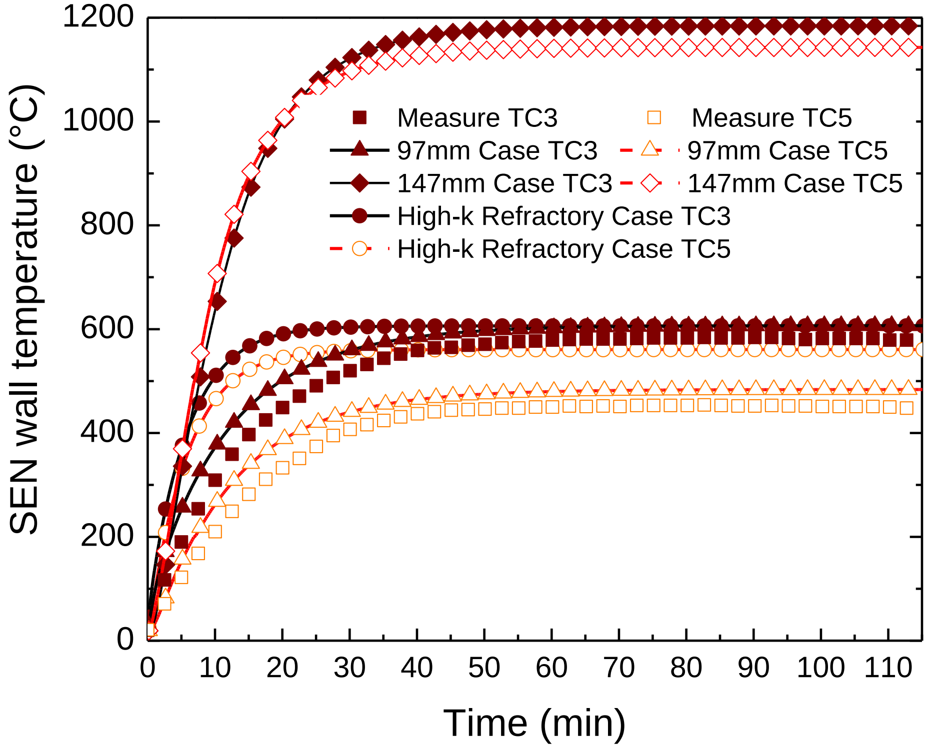

Figure 6.6 Transient temperature comparisons between 97mm Validation Case, 147mm Case and High-k Refractory Case

Chapter 7: Spreadsheet Models

7.1 Introduction

A spreadsheet model system, including a Steady-State Flame Temperature Model and a Transient SEN Heat Conduction Model, was developed by V. Singh [7.1, 7.2]. This spreadsheet model system is improved here by validating with experiment, 2D Combustion Model and Heat Conduction Model by using FLUENT (Appendix A, B) [7.3,7.4].

The Steady-State Flame Temperature Model calculates adiabatic flame temperature by a chemical equilibrium program, Gaseq [7.5], with given inputs of fuel, Oxygen Source Fraction, Air Entrainment, reactants pressure and temperature. In addition, this Flame Temperature Model provides gas-products properties, and convection coefficients at the SEN walls.

The Transient SEN Heat Conduction Model calculates SEN temperature histories by solving the 1-D axisymmetric transient heat conduction equation discretized using an explicit finite volume method. The inputs include SEN geometry, material properties, initial temperature, and inner and outer wall heat transfer coefficients. The model outputs temperature distributions across the SEN wall and transient temperature histories.

7.2 Steady-State Flame Temperature Model

Figure 7.1 shows the basic structure of Flame Temperature Model: inputs, Gaseq [7.5], and outputs. Gaseq [7.5] is a chemical equilibrium program which can predict adiabatic temperature and composition at constant pressure. With given inputs of fuel type, oxygen source, oxygen source fraction, air entrainment, reactants pressure and temperature, Flame Temperature Model predicts flame temperature, products pressure, species component, products properties, and convection coefficients at the SEN walls.

7.2.1 Definitions of Oxygen Source Fraction, Air Entrainment, and the Equivalence Ratio

Oxygen Source Fraction is defined here as the molar ratio of oxygen input with the fuel relative to stoichiometric combustion reaction oxygen input requirement of 100%. Air Entrainment is the molar ratio of extra outside air entrained relative to the amount of air that would be needed for stoichiometric combustion, neglecting the Oxygen Source. In the preheating experiment, Oxygen Source Fraction can be calculated from the pressure, the temperature, and the volume flow rate of methane and oxygen respectively. However, the amount of the entrained air can be hardly measured from the experiment. So the current 2D Combustion Model is applied to simulate the preheating process, including an output of the air entrainment.

Equations to calculate Oxygen Source Fraction and Air Entrainment are given in Equations (7.1) and (7.2). For a fuel with the general composition C_xH_y, the stoichiometric combustion reaction with a pure oxygen source is:

$$C_xH_y + (x + \frac{y}{4})O_2 = xCO_2 + \frac{y}{2}H_2O$$

$$Oxygen\ Source\ Fraction = \frac{\dot{n}_{O2}}{(x + y/4)\dot{n}_{fuel}} = \frac{\dot{m}_{O2}MW_{fuel}}{(x + y/4)\dot{m}_{fuel}MW_{o2}} = \frac{P_{O2}}{(x + y/4)P_{fuel}} \cdot \frac{\dot{V}_{O2}}{\dot{V}_{fuel}} \cdot \frac{T_{fuel}}{T_{O2}} \quad (7.1)$$

For the same general fuel with composition C_xH_y, the stoichiometric combustion reaction with air is:

$$C_xH_y + \left(x + \frac{y}{4}\right)O_2 + 3.76\left(x + \frac{y}{4}\right)N_2 = xCO_2 + \frac{y}{2}H_2O + 3.76\left(x + \frac{y}{4}\right)N_2$$

$$Air\ Entrainment = \frac{\dot{n}_{air}}{4.76\left(x + \frac{y}{4}\right)\dot{n}_{fuel}} = \frac{\dot{m}_{air}MW_{fuel}}{4.76\left(x + \frac{y}{4}\right)\dot{m}_{fuel}MW_{air}} = \frac{\dot{n}_{N2}}{3.76\left(x + \frac{y}{4}\right)\dot{n}_{fuel}}$$

$$= \frac{\dot{m}_{N2}MW_{fuel}}{3.76\left(x+\frac{y}{4}\right)\dot{m}_{fuel}MW_{N2}} = \frac{\dot{n}_{+\_O2}}{\left(x+\frac{y}{4}\right)\dot{n}_{fuel}} = \frac{\dot{m}_{+\_O2}MW_{fuel}}{(x+y/4)\dot{m}_{fuel}MW_{O2}} \quad (7.2)$$

where $\dot{n}$ is the molar rate (mole/s),

$\dot{n}_{O2}$ is the molar rate of oxygen input in the gas mixture through the burner tip (mole/s),

$\dot{n}_{+\_O2}$ is the molar rate of oxygen input by entrained air (mole/s),

P is the absolute pressure (Pa),

$\dot{V}$ is the volume flow rate (m^3/s),

T is the reactant temperature (K),

$\dot{m}$ is the mass flow rate (kg/s),

MW is the molecular weight (kg/mole).

Equation (7.2) indicates two methods to calculate the air entrainment from the results of the combustion model. Method 1 assumes that the extra mass flow rate entering the SEN at its top inlet surface is caused by the entrained air. Method 2 converts the nitrogen mass flow rate across the SEN top inlet into the corresponding entrained air. Table 7.1 lists the steps and results of both methods for the 97mm Validation Case, and they match well, considering numerical errors.

The equivalence ratio is commonly used to quantify the extent that a fuel-oxidizer mixture is fuel-rich, or fuel-lean, relative to the stoichiometric ratio. It is defined in Equation (7.3).

$$\emptyset = \frac{fuel\ to\ oxidizer\ ratio}{(fuel\ to\ oxidizer\ ratio)_{st}} = \frac{m_{fuel}/m_{ox}}{(m_{fuel}/m_{ox})_{st}} = \frac{n_{fuel}/n_{ox}}{(n_{fuel}/n_{ox})_{st}} = \frac{\dot{n}_{fuel}/\dot{n}_{ox}}{(\dot{n}_{fuel}/\dot{n}_{ox})_{st}} \quad (7.3)$$

where "oxidizer" is the total oxygen mole flow rate composed of the oxygen at the gas-mixture inlet and the oxygen from the entrained air.

$$\dot{n}_{O2} = Oxygen\ source\ fraction \times (x + y/4)\dot{n}_{fuel}$$

$$\dot{n}_{+\_O2} = Air\ entrainment \times (x + y/4)\dot{n}_{fuel}$$

In terms of the two parameters defined in Equations (7.1) and (7.2), the equivalence ratio is the inverted sum of the Oxygen Source Fraction and the Air Entrainment:

$$\emptyset = \frac{\dot{n}_{fuel}/\dot{n}_{ox}}{(\dot{n}_{fuel}/\dot{n}_{ox})_{st}} = \frac{\dot{n}_{fuel}/(\dot{n}_{O2}+\dot{n}_{+\_O2})}{\dot{n}_{fuel}/((x+y/4)\dot{n}_{fuel})} = \frac{1}{Oxygen\ Source\ Fraction+Air\ Entrainment} \tag{7.4}$$

For the 97mm Validation Case, Oxygen Source Fraction is 100% and Air Entrainment is 154%, so the equivalence ratio is 0.397. For the 147mm Case, the equivalence ratio is 0.426.

7.2.2 Adiabatic Flame Temperature Model

For the 97mm Validation Case, 2D Combustion Model outputs, which are (total gas-mixture) mass flow rate at the SEN top inlet, and Nitrogen mass flow rate at the SEN top inlet, give 154% air entrainment (using Eq. 7.2). From the measured 100% oxygen source fraction, 19^{o}C reactants temperature and 1 atm reactants pressure, the predicted flame temperature from Flame Temperature Model is 1328^{o}C. The average gas temperature at thermocouple No. 1-3-5 level is 1307 ^{o}C, which differs by only 21 ^{o}C from the Flame Temperature Model prediction. The gas product compositions are listed in Table 7.5 for 97mm Validation Case.

For the 147mm Case, the 2D Combustion Model results give 135% air entrainment. From the measured 100% oxygen source fraction, 19^{o}C reactants temperature and 1 atm reactants pressure, the Flame Temperature Model predicts a flame temperature of 1451^{o}C. This increasing trend is expected because increasing the stand-off distance gives a longer distance for the flame jet to spread before entering the SEN, which lessens the Venturi effect, and thus allows less air entrainment. With less air dilution, the gas temperature inside the SEN increases. The average gas temperature at thermocouple No. 1-3-5 level is 1587 ^{o}C, which is even larger than the Flame Temperature Model prediction. The gas product compositions are listed in Table 7.6 for 147mm Case. Specifically, the Flame Temperature Model predicts mole fractions of 0.00136% CO and

6.30620% CO_2. The 2D Combustion Model predicts 2.04% CO and 4.33% CO_2 at the TC 1-3-5 level.

From Figures 7.5 and 7.6, the two models predict similar amount of gas products, but not exactly the same, since two models use different reaction mechanisms. For the Flame Temperature Model, equilibrium reactions are used. For 2D Combustion Model, non-equilibrium reactions are applied. Compared with 97mm Validation Case, gas product compositions in 147mm Case show more CO_2 transforms into CO, predicted by Flame Temperature Model and 2D Combustion Model.

Thus, the simple spread-sheet model can predict the flame temperature approximately without needing the sophisticated chemical reactions and thermal hydraulic models. The flame temperature and corresponding heating inside the SEN is controlled by the air entrainment.

7.3 Transient Heat Conduction Model

7.3.1 Model set up

A spreadsheet model is developed to predict the transient temperature distribution in the SEN, using a Finite Volume Method discretization. Since heat conduction in axial direction is negligible, the heat conduction is simplified as 1D through the SEN wall in the radial direction. This model is user friendly, as it allows users to change model inputs: SEN geometry (number of layers and material for each layer); ambient, initial and gas temperatures; heat transfer coefficients at inner and outer wall; preheat time; and material properties. Two further cases are studied with this Heat Conduction Model: 97mm Validation Case and Can Case. Firstly, the Heat Conduction Model is validated with experiment measurement. Then in the parametric study, outer glaze layer is replaced with steel can to investigate the effect of steel can. The main interface of this Heat Conduction Model is displayed in Figure 7.3.

The governing equations and boundary conditions are listed in Equation (7.5)-(7.7). The discretization equations for the cell at the interior, inner wall, and outer wall are developed in Appendix A. This Heat Conduction Model has been validated with 3D heat conduction model, with temperature dependent properties materials in each layer. The validation details are represented in Appendix A and B.

$$\frac{\partial}{\partial t}(\rho C T) = \frac{1}{r}\frac{\partial}{\partial r}\left(rk\frac{\partial T}{\partial r}\right) \tag{7.5}$$

$$-\frac{k}{r}\frac{\partial}{\partial r}(rT)\bigg|_{r=R_{in}} = h_{in}\left(T_{bulk_{in}} - T_{in}\right) \tag{7.6}$$

$$\frac{k}{r}\frac{\partial}{\partial r}(rT)\bigg|_{r=R_{out}} = h_{out}\left(T_{bulk_{out}} - T_{out}\right) \tag{7.7}$$

where R_{in} is the SEN inner radius (m),

R_{out} is the SEN outer radius (m),

h_{in} is the internal heat transfer coefficient (W/m^{2}K), including radiation and convection heat transfer coefficients),

h_{out} is the external heat transfer coefficient (W/m^{2}K), including radiation and convection heat transfer coefficients),

$T_{bulk_{in}}$ is the SEN inner bulk temperature (^{o}C),

$T_{bulk_{out}}$ is the SEN outer bulk (air) temperature (^{o}C),

T_{in} is the SEN inner wall temperature (^{o}C),

T_{out} is the SEN outer wall temperature (^{o}C).

7.3.2 Model input

In the 97mm Validation Case, the Heat Conduction Model inputs, given in Table 7.2 and Table 7.3 are from the 97mm Validation Case experiment and the 2D Combustion Model, such as air entrainment prediction, internal and external heat transfer coefficients (HTC), average inner gas temperature. Internal and external heat transfer coefficients (including the effect of radiation) at TC 1-3-5 are taken from 2D Combustion Model output profiles along the SEN wall shown in Figure 7.4. At the TC 1-3-5 level, which is 197mm below SEN top, the inner wall HTC is 112 W/m^{2}K, and the outer wall HTC is 66 W/m^{2}K. At the TC 4-6 line, which is 341mm below SEN top, the inner wall HTC is 107 W/m^{2}K, and the outer wall HTC is 67 W/m^{2}K. Table 7.2 lists main inputs, and SEN geometries and number of nodes in each layer are listed in Table 7.3. Material properties are the same as listed in Tables 4.1-4.4.

Inner gas bulk temperature at TC 1-3-5 from 2D Combustion Model is calculated based on Equation (7.8) as 1307^{o}C.

$$\bar{T} = \frac{\sum_{r=0}^{r=R} 2\pi r T dr}{\pi R^2} \qquad (7.8)$$

where r is the SEN radius (mm),

T is the gas temperature (^{o}C) from Combustion Model at corresponding radius (r),

R is the SEN inner bore radius, which is 37.5mm in measurement.

The convergence criterion used to define the time step size in this 1D explicit Heat Conduction Model is given in Equations (7.9), 0.48, which is smaller than 0.5, is used in Equation (7.10) . In the 97mm Validation Case, the smallest cell size is 0.14mm at glaze layer, so the time step is 0.014s. Modeling 115min of preheating with the Heat Conduction Model takes 2mins to run on 4GB 64-bit Operating System.

$$\frac{D_h d_t}{d_x d_x} < \frac{1}{2} \qquad (7.9)$$

$$d_t = 0.48 D_h \, d_x^2 \qquad (7.10)$$

where D_h is thermal diffusivity (m^2/s),

d_t is time step (s),

d_x is smallest cell size (m).

7.3.3 Model output

Figure 7.5 shows SEN wall temperature histories predicted by the Heat Conduction Model in 97mm Validation Case. Since TC 3 and TC 4 are closer to SEN inner wall, temperatures at TC 3 and TC4 are about 650°C, about 200°C higher than TC 5 and 6. The same inner gas temperature is used for TC 1-3-5 level and TC 4-6, but due to higher HTC at the TC 1-3-5 level at steady state, TC 3 and TC 5 are hotter than TC 4 and TC6, by 13°C and 8°C respectively.

Figure 7.6 compares SEN wall temperature from the Heat Conduction Model with the measurements in 97mm Validation Case. Overall, the Heat Conduction Model over predicts SEN wall temperature. The Heat Conduction Model predicts similar heating rates for the beginning ~40mins. Then the model temperature increases faster, finally over-predicting at steady state. The largest over-prediction is 98°C at TC 4 and the smallest is 24°C at TC5. Many uncertainties can cause error at that range, such as refractory material property variations, heat transfer coefficient differences, emissivity of the inner gas and outer wall (which are not inputs to the Heat Conduction Model, but are outputs from the 2D Combustion Model), etc.

Figure 7.7 shows SEN wall temperature comparison between Heat Conduction Model and Combustion Model (FLUENT) in 97mm Validation Case97mm Validation Case97mm Validation Case . Both models show similar heating up rate at transient stage before 40mins. Heat Conduction Model predicts higher TC 3 and TC 4 temperatures, but predicts lower TC 5 and TC 6 temperatures.

7.3.4 Parametric study

A simulation was conducted to investigate the effect of the outside steel can, typically used to protect the nozzle in service. Conditions are the same as the experimental case, listed in Table 7.2, except that the outer glaze layer is replaced with a 3mm-thick steel layer to represent the can. The domain geometry including number of nodes in each layer is listed in Table 7.4. Figure 7.8 shows SEN wall temperatures predicted by Heat Conduction Model in Can Case. This figure shows that replacing the outer glaze layer with a steel can causes SEN refractory temperatures to decrease overall. TCs 3 and 4 are about 250 °C lower, and TCs 5 and 6 are about 75 °C lower. The Can Case takes ~30mins to reach steady state, which is less than the 97mm Case (~40mins). This case shows that the glaze layer is very influential, by raising the steady state temperature of SEN wall.

Tables

Table 7.1 Air Entrainment of 97mm Validation Case calculated from Combustion Model Results

Method 1		Method 2	
Mass flow rate at the burner tip	4.71 g/s	Nitrogen mass flow at the burner tip	0 g/s
Mass flow rate at the SEN top inlet	29.66 g/s	Methane mass flow at the burner tip	0.94 g/s
Entrained Air mass flow rate	24.96 g/s	Nitrogen mass flow rate at the SEN top inlet	19.15 g/s
Air Entrainment	153.7%	Air Entrainment	154.4%

Table 7.2 Heat Conduction Model Main Inputs of 97mm Validation Case97mm Validation Case97mm Validation Case97mm Validation Case

Heat Conduction Model Input Conditions	Value
Initial temperature	19 ^{o}C
Inner gas temperature	1307 ^{o}C
Ambient temperature	19 ^{o}C
Internal HTC at TC1-3-5	112 W/m^{2}K
External HTC at TC 1-3-5	66 W/m^{2}K
Internal HTC at TC4-6	107 W/m^{2}K
External HTC at TC 4-6	67 W/m^{2}K
Emissivity of inner glaze	0
Emissivity of inner flame	0
Thermal properties	Table 4.1-4.4
Preheat time	115 min

Table 7.3 Heat Conduction Model Domain of 97mm Validation Case97mm Validation Case97mm Validation Case97mm Validation Case

Layer	Material	Thickness (mm)	Number of Nodes
1	Material Glaze	0.7	5
2	Material Doloma Graphite	37	58
3	Material Glaze	0.7	5

Table 7.4 Heat Conduction Model Domain in steel Can Case

Layer	Material	Thickness (mm)	Number of Nodes
1	Material Glaze	0.7	5
2	Material Doloma Graphite	37	58
3	Steel	3	5

Table 7.5 Gas Compositions Calculated for 97mm Validation Case (154% Air Entrainment)

Product	Compositions (%)	
	Flame Temperature Model	2D Combustion Model
N_2	65.48254%	63.54%
O_2	17.34764%	17.34%
H_2O	11.3146%	9.20%
CO_2	5.66185%	4.42%
NO	0.17373%	0.18%
OH	0.01854%	0.03%
O	0.00061%	2.75%
CO	0.00027%	0.02%
H_2	0.00018%	0.70%
H	0.00001%	1.83%
CH_4	0.00000%	0.00%

Table 7.6 Gas Compositions Calculated for Insulated Case (135% Air Entrainment)

Product	Compositions (%)	
	Flame Temperature Model	2D Combustion Model
N_2	63.89589%	62.66%
O_2	16.88163%	16.57%
H_2O	12.59121%	9.25%
CO_2	6.30620%	4.33%
NO	0.27434%	0.23%
OH	0.04621%	1.34%
O	0.00233%	1.58%
CO	0.00136%	2.04%
H_2	0.00078%	0.55%
H	0.00005%	1.45%
CH_4	0.00000%	0.00%

Figures

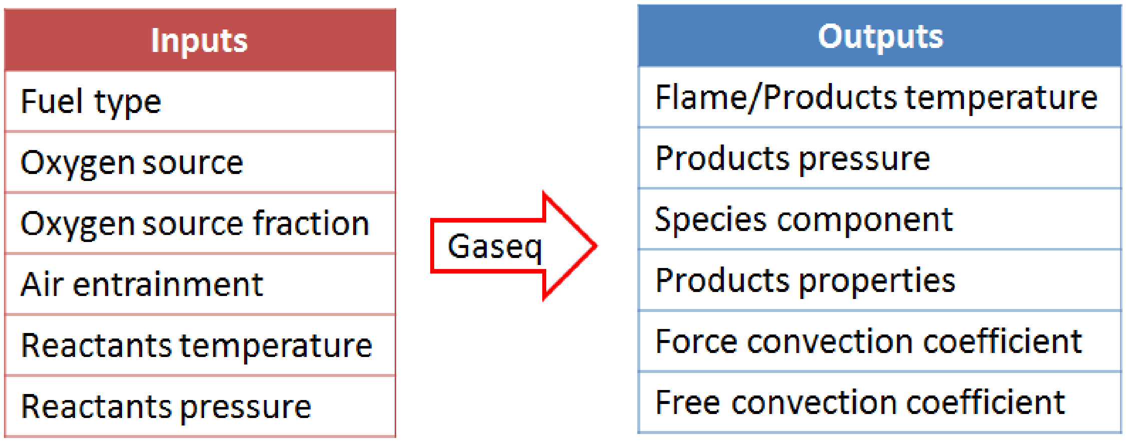

Figure 7.1 Flame Temperature Model basic structure

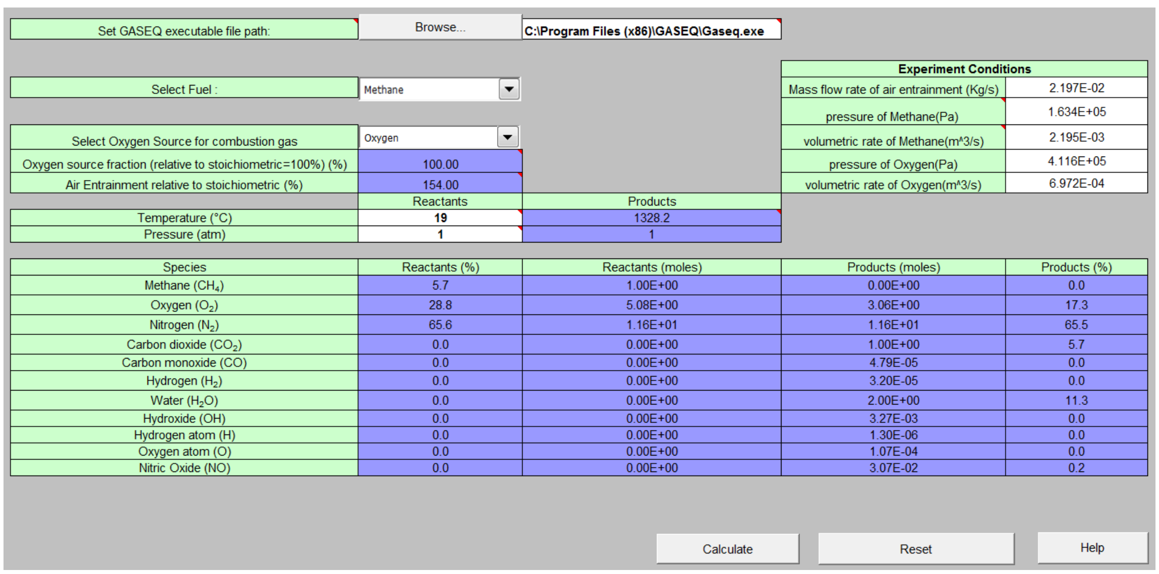

Figure 7.2 Flame Temperature Model main interface

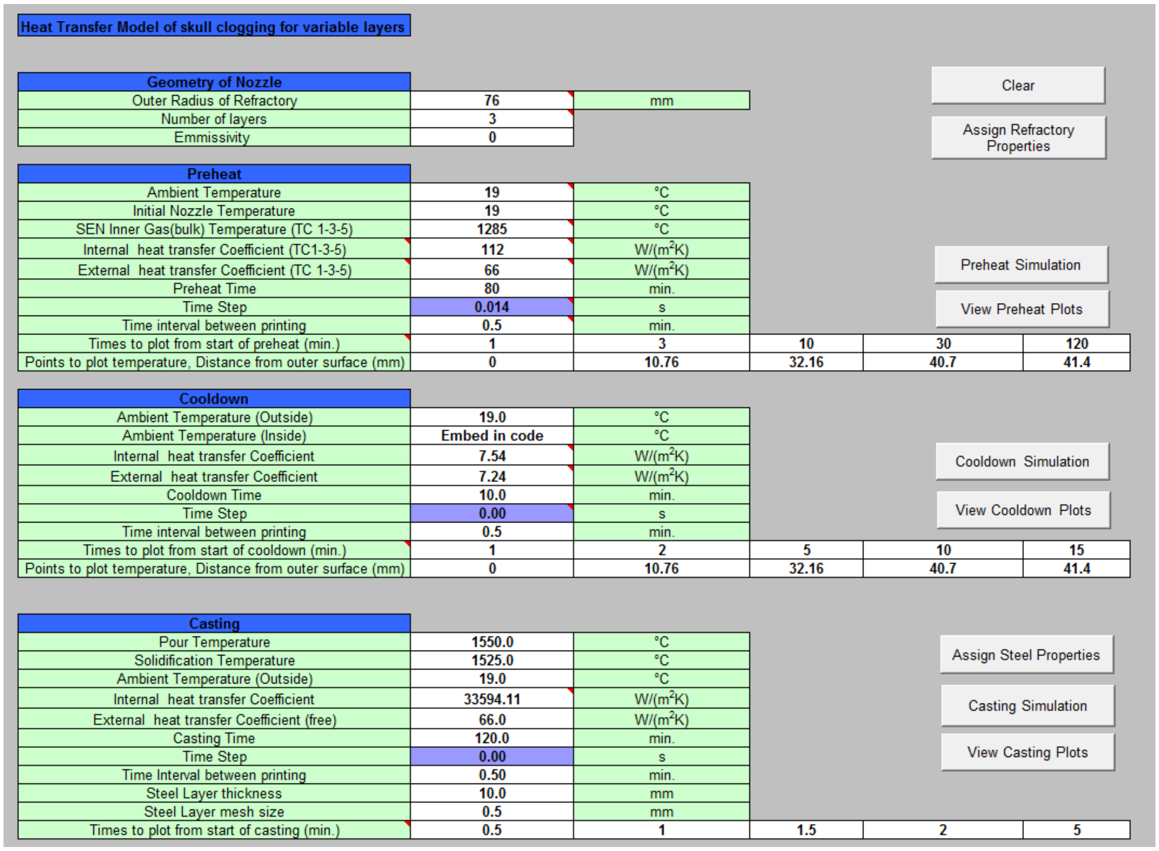

Heat Transfer Model of skull clogging for variable layers					
Geometry of Nozzle					
Outer Radius of Refractory	76	mm			
Number of layers	3				
Emmissivity	0				
Preheat					
Ambient Temperature	19	°C			
Initial Nozzle Temperature	19	°C			
SEN Inner Gas(bulk) Temperature (TC 1-3-5)	1285	°C			
Internal heat transfer Coefficient (TC1-3-5)	112	W/(m^{2}K)			
External heat transfer Coefficient (TC 1-3-5)	66	W/(m^{2}K)			
Preheat Time	80	min.			
Time Step	0.014	s			
Time interval between printing	0.5	min.			
Times to plot from start of preheat (min.)	1	3	10	30	120
Points to plot temperature, Distance from outer surface (mm)	0	10.76	32.16	40.7	41.4
Cooldown					
Ambient Temperature (Outside)	19.0	°C			
Ambient Temperature (Inside)	Embed in code	°C			
Internal heat transfer Coefficient	7.54	W/(m^{2}K)			
External heat transfer Coefficient	7.24	W/(m^{2}K)			
Cooldown Time	10.0	min.			
Time Step	0.00	s			
Time interval between printing	0.5	min.			
Times to plot from start of cooldown (min.)	1	2	5	10	15
Points to plot temperature, Distance from outer surface (mm)	0	10.76	32.16	40.7	41.4
Casting					
Pour Temperature	1550.0	°C			
Solidification Temperature	1525.0	°C			
Ambient Temperature (Outside)	19.0	°C			
Internal heat transfer Coefficient	33594.11	W/(m^{2}K)			
External heat transfer Coefficient (free)	66.0	W/(m^{2}K)			
Casting Time	120.0	min.			
Time Step	0.00	s			
Time Interval between printing	0.50	min.			
Steel Layer thickness	10.0	mm			
Steel Layer mesh size	0.5	mm			
Times to plot from start of casting (min.)	0.5	1	1.5	2	5

Figure 7.3 Heat Conduction Model main user interface

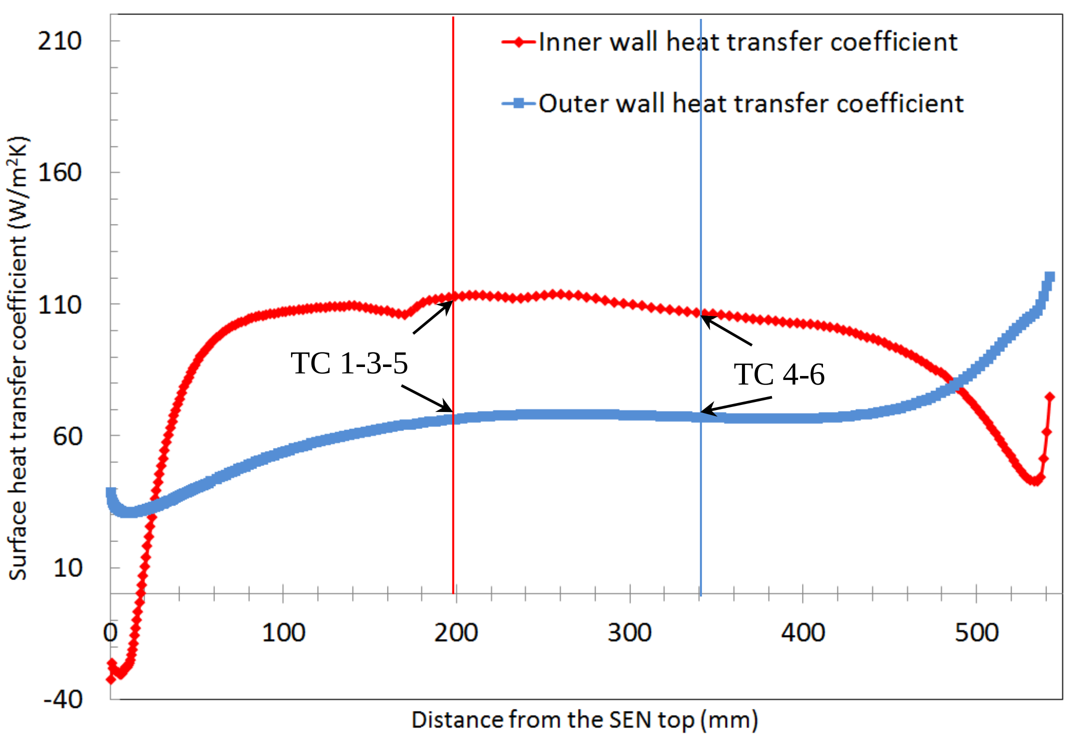

Figure 7.4 Heat transfer coefficients along SEN inner and outer wall

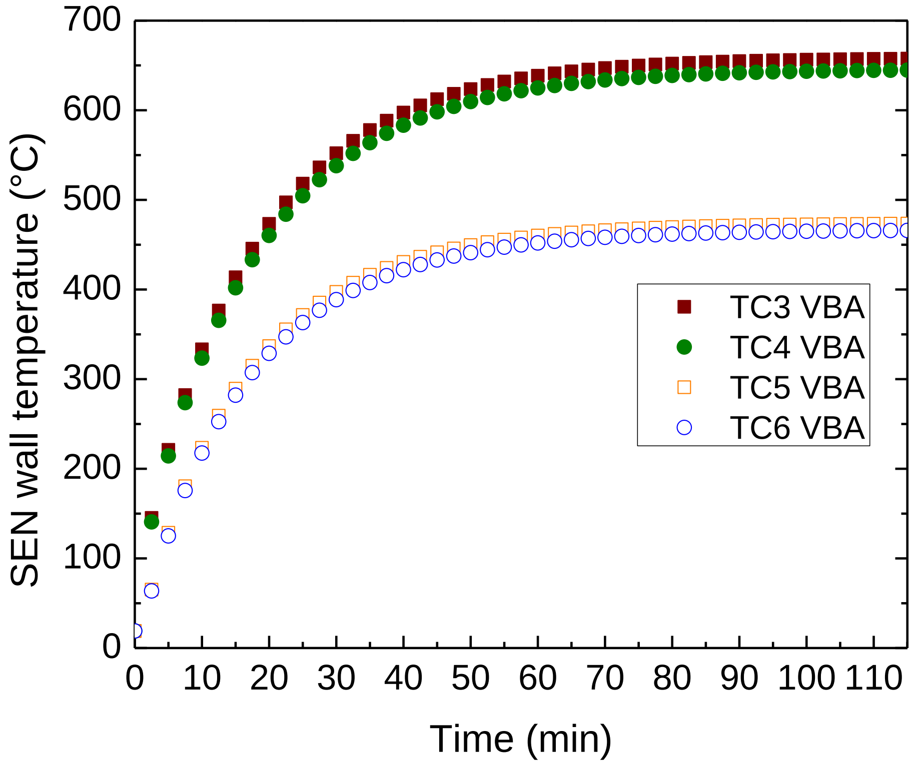

Figure 7.5 SEN wall temperature of Heat Conduction Model (VBA) in 97mm Validation Case

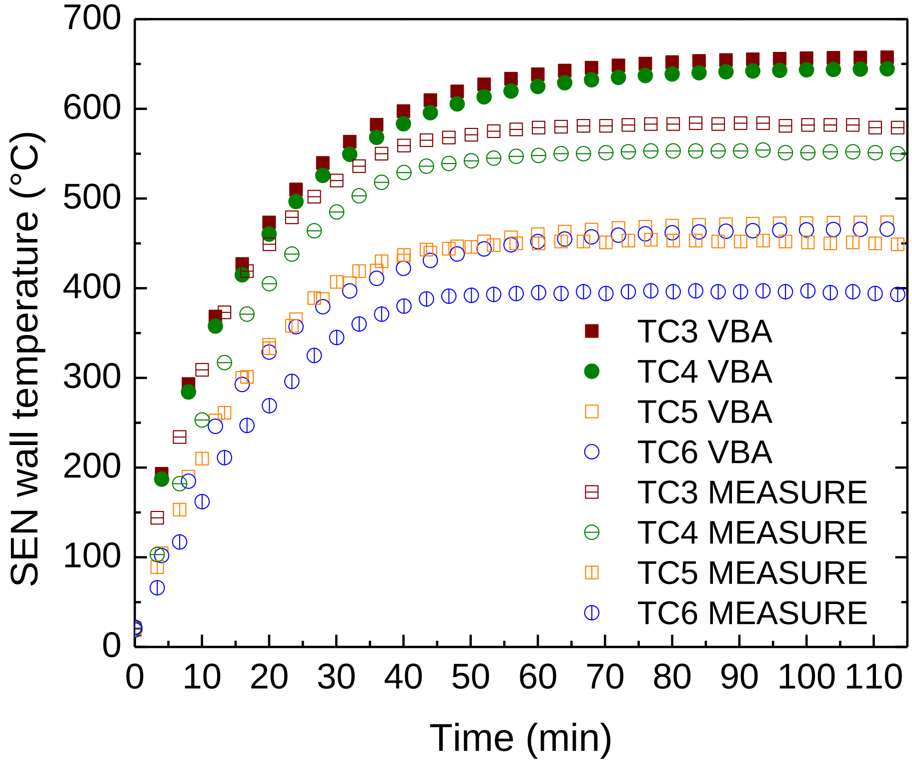

Figure 7.6 SEN wall temperature comparison between
Heat Conduction Model (VBA) and measurement in 97mm Validation Case

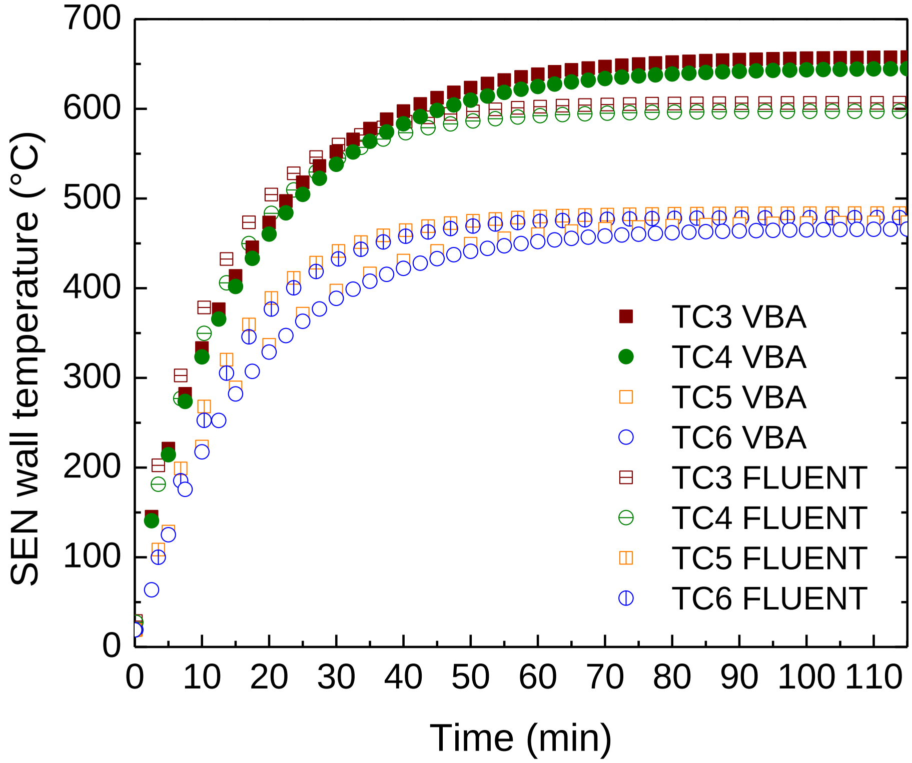

Figure 7.7 SEN wall temperature comparison between
Heat Conduction Model (VBA) and Combustion Model (FLUENT) in 97mm Validation Case

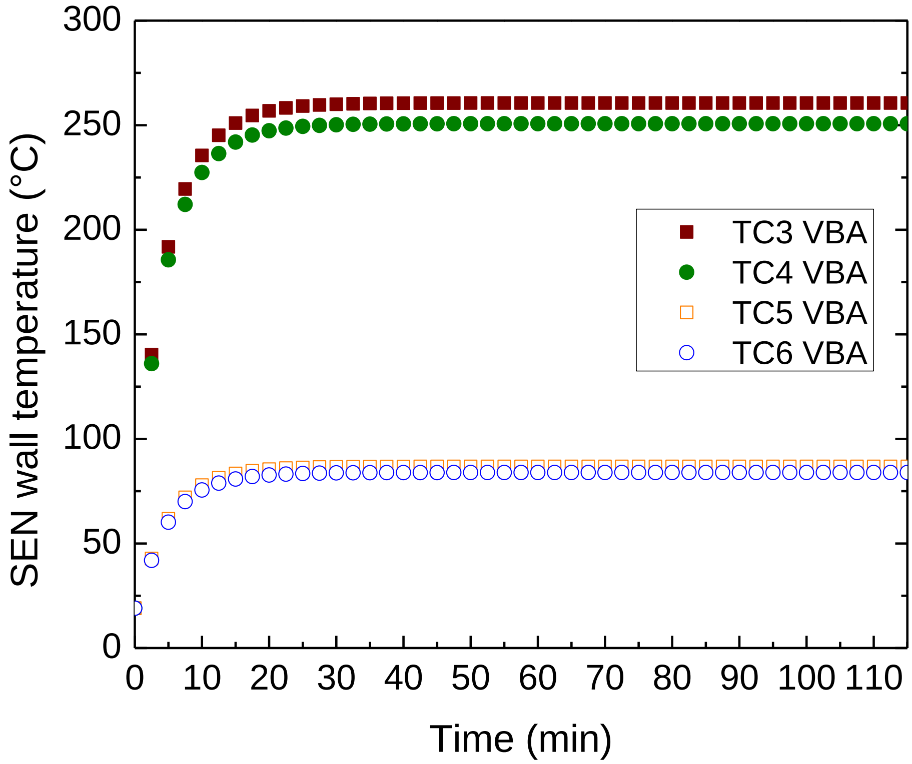

Figure 7.8 SEN wall temperature predicted by Heat Conduction Model (VBA) in Can Case

References

7.1 V. Singh, Flame temperature VBA model, Excel software, University of Illinois at Urbana-Champaign, 2010

7.2 V. Singh, Heat Conduction VBA model, Excel software, University of Illinois at Urbana-Champaign, 2010

7.3 Y. Li, Flame temperature VBA model, Excel software, University of Illinois at Urbana-Champaign, 2014

7.4 Y. Li, Heat Conduction VBA model, Excel software, University of Illinois at Urbana-Champaign, 2014

7.5 Gaseq, Chemical equilibrium program, available at http://www.gaseq.co.uk/

Chapter 8: Conclusions

In this work, a 2D axisymmetric model of nozzle preheating is developed using FLUENT with GRI-Mech 3.0 and includes 325 non-equilibrium chemical reactions with 53 species to simulate methane combustion. The finite-volume computational model simulates steady-state fluid flow, heat transfer, and combustion in the gas and transient heat conduction in the SEN walls. Simple user-friendly spread-sheet models to predict flame and SEN temperature are validated and improved.

- The model predictions match experimental measurements of a methanae torch preheating experiment, including the temperature profile across the flame, temperature histories measured inside the SEN wall, the flame shape, and the SEN outer wall temperature distribution.
- Heat Conduction Model can predict SEN wall temperature histories has been validated, with the ability of changing SEN materials, geometries, initial conditions, and boundary conditions by users.
- The validated model was then applied to investigate the effects of stand-off distance, insulation, and wall conductivity.
- Moving the burner further above the SEN top, to give the flame enough distance to spread to fill the SEN diameter, leads to higher SEN temperature and shorter preheating time, due to less air entrainment.
- Adding an insulation layer causes higher SEN wall temperatures and milder temperature gradients.
- Increasing refractory conductivity causes milder gradient at SEN.

- To optimize preheating, a proper stand-off distance, stoichiometric fuel composition, proper refractory thermal properties , and insulation layers are recommended.
- A simple spread-sheet model of the adiabatic flame temperature is shown to accurately predict the gas temperature inside the SEN, based on knowing the air entrainment.

Appendix A

A. Discretized governing equation in 1D Heat Conduction VBA Model

This appendix is to develop discretized governing equations for 1D Heat Conduction VBA Model in the SEN wall with multiple layers using the VBA macros in MS excel, and validate it by comparing with FLUENT 3D Transient Model. Finite Volume Method is used to derive discretized governing equations on the interface cell of two different material, interior cell and boundary cells. Based on the derived governing equations, the code in Heat Conduction VBA Model is changed. The results from Heat Conduction VBA Model are compared with FLUENT Transient Model, with constant material properties in three layers, and match within 0.5% error.

Method

Preparation:

- r is the radius of a sector;
- z is the thickness of the sector;
- w and e are located on the boundary of cell P;
- W and E means the center point of the west cell and east cell of cell P;
- The volume of a sector = $\frac{1}{2}r^2\varphi z$;
- Heat conduction direction cross section area = $r\varphi z$;
- $r_e = r_p + \frac{1}{2}\delta r_{PE}$;
- $r_w = r_p - \frac{1}{2}\delta r_{PW}$;
- The volume of P cell $= \frac{{r_e}^2\varphi z}{2} - \frac{{r_w}^2\varphi z}{2}$.

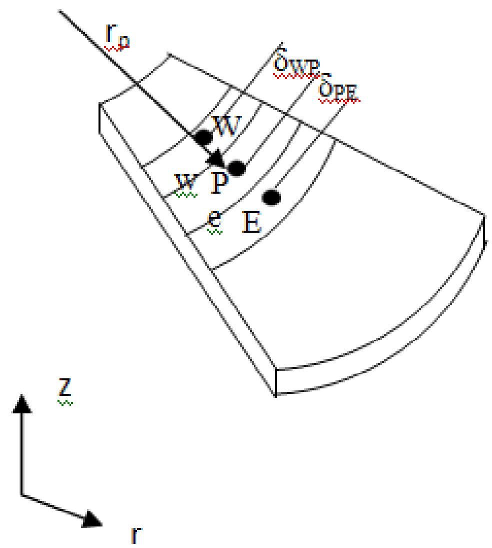

Fig A.1 Notation of Finite Volume Method

1. Finite Volume Equation for Interface Cell

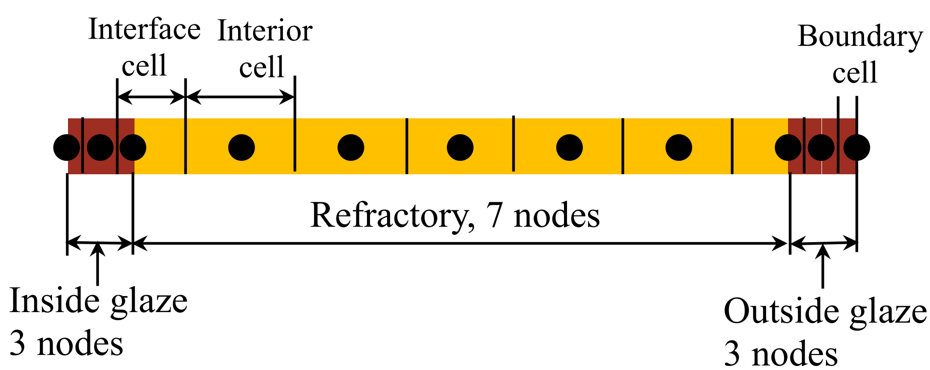

Fig A.2 Cells schematic map on 1D Heat Conduction VBA Model

Derivation

Heat conduction governing equation:

$$\frac{\partial}{\partial t}(\rho c_p T) = \frac{1}{r}\frac{\partial}{\partial r}(rk\frac{\partial T}{\partial r})$$

Finite Volume method derivation:

$$\int_t^{t+\Delta t}(\int_{cv}\frac{\partial}{\partial t}(\rho c_p T)dV)dt = \int_t^{t+\Delta t}(\int_{cv}\frac{1}{r}\frac{\partial}{\partial r}(rk\frac{\partial T}{\partial r})dV)dt \qquad (A.1)$$

Gauss's Divergence theorem:

$$\int_{cv} div(\overline{a})dV = \int_A \vec{n}\ \vec{a}\ dA$$

In cylindrical coordinate:

$$div(\vec{a}) = \frac{1}{r}\frac{\partial}{\partial r}(r\vec{a})$$

$$\int_{cv} \frac{1}{r}\frac{\partial}{\partial r}\left(rk\frac{\partial T}{\partial r}\right)dV = \int_{cv} div\left(k\frac{\partial T}{\partial r}\right)dV = \int_A \vec{n}\ k\frac{\partial T}{\partial r}\ dA$$

$$= \left(k\frac{\partial T}{\partial r}\ A\right)|_e - \left(k\frac{\partial T}{\partial r}\ A\right)|_w$$

$$= \left(k_e\frac{\partial T}{\partial r}|_e\ r_e\ \varphi\ z\right) - \left(k_w\frac{\partial T}{\partial r}|_w\ r_w\ \varphi\ z\right)$$

$$= k_e\frac{\partial T}{\partial r}|_e\ r_e\ \varphi\ z - k_w\frac{\partial T}{\partial r}|_w\ r_w\ \varphi\ z$$

$$= k_e\frac{T_E - T_P}{\delta r_{PE}}\ r_e\ \varphi\ z - k_w\frac{T_P - T_W}{\delta r_{PW}}\ r_w\ \varphi\ z$$

Integrate from t to t + Δt:

$$\int_t^{t+\Delta t} T_P^{n+1}dt = (\theta T_P^{n+1} + (1-\theta)T_P^n)\Delta t$$

$$\theta = 0\ is\ explicit\ method, \theta = 1\ is\ fully\ implicit\ method.$$

$$T_P^n\ means\ temperature\ at\ t, T_P^{n+1}\ means\ temperature\ at\ t + \Delta t.$$

The right side of Eq. (A.1) is equal to:

$$\varphi\ z\int_t^{t+\Delta t}\left(k_e\frac{T_E - T_P}{\delta r_{PE}}\ r_e - k_w\frac{T_P - T_W}{\delta r_{PW}}\ r_w\right)dt$$

$$= \varphi\ z\ (k_e\frac{(\theta T_E + (1-\theta)T_E^{n+1}) - (\theta T_P + (1-\theta)T_P^{n+1})}{\delta r_{PE}}\ r_e - k_w\frac{(\theta T_P + (1-\theta)T_P^{n+1}) - (\theta T_W + (1-\theta)T_W^{n+1})}{\delta r_{PW}} r_w)\Delta t$$

$$= \varphi\ z\ \Delta t(\theta\left(\frac{k_e r_e}{\Delta r_{PE}}T_E^{n+1} - \frac{k_e r_e}{\Delta r_{PE}}\ T_P^{n+1} - \frac{k_w r_w}{\Delta r_{PW}}\ T_P^{n+1} + \frac{k_w r_w}{\Delta r_{PW}}\ T_W^{n+1}\right) +$$

$$(1-\theta)(\frac{k_e r_e}{\Delta r_{PE}}T_E^n - \frac{k_e r_e}{\Delta r_{PE}}\ T_P^n\ - \frac{k_w r_w}{\Delta r_{PW}}\ T_P^n + \frac{k_w r_w}{\Delta r_{PW}}\ T_W^n))$$

The left side of Eq.(A.1) is equal to:

$$\int_{cv}\left(\int_{t}^{t+\Delta t}\frac{\partial}{\partial t}\left(\rho C_p T\right)dt\right)dV=\int_{cv}\rho C_p\left(T_P^{n+1}-T_P^{n}\right)dV=\int_{cv}\rho C_p T_P^{n+1}dV-\int_{cv}\rho C_p T_P^{n}dV$$

$$=\varphi z\left[\rho_w C_{pw}T_P^{n+1}\left(\frac{r_p^2-r_w^2}{2}\right)+\ \rho_e C_{pe}T_P^{n+1}\left(\frac{r_e^2-r_p^2}{2}\right)\right]-$$

$$\varphi z\left[\rho_w C_{pw}T_P^{n}\left(\frac{r_p^2-r_w^2}{2}\right)+\ \rho_e C_{pe}T_P^{n}\left(\frac{r_e^2-r_p^2}{2}\right)\right]$$

$$=\ \varphi z\left[\rho_w C_{pw}\left(\frac{r_p^2-r_w^2}{2}\right)+\rho_e C_{pe}\left(\frac{r_e^2-r_p^2}{2}\right)\right]\left(T_P^{n+1}-T_P^{n}\right)$$

From figure A.1, it is clear that

$$T_W^n=T_{P-1}^n$$

$$T_E^n=T_{P+1}^n$$

Set $\theta=0$ for the explicit method. Let right side to be equal as left side of Eq.1.The discrete finite volume equation comes out after arranging as following.

$$T_p^{n+1}=T_p^n+\frac{\left[\frac{k_e r_e}{\Delta r_{PE}}\left(T_{P+1}^n-T_p^n\right)-\frac{k_w r_w}{\Delta r_{PW}}\left(T_p^n-T_{P-1}^n\right)\right]\Delta t}{\left[\rho_w C_{pw}\left(\frac{r_p^2-r_w^2}{2}\right)+\rho_e C_{pe}\left(\frac{r_e^2-r_p^2}{2}\right)\right]}\qquad (A.2)$$

Eq.2 is the governing equation of the interface node, which also can apply for interior cell. ρ (density) and C_p (heat capacity) is the material properties of the cell. For interface cell, ρ and C_p should be the average value of the two material in the same cell.

2. Using Finite Volume Method for interior cell

Because there is only one material of the interior cell, $k_w=k_e$.

$r_e=r_p+\frac{1}{2}\delta r$, $r_w=r_p-\frac{1}{2}\delta r$, $\delta r_{PE}=\delta r_{PW}=\delta r=\Delta r$.

Simplified interior governing equation is derived by plugging the above four equations into Eq.2.

$$T_p^{n+1} = \left(1 - \frac{2\alpha\Delta t}{\Delta r^2}\right)T_p^n + \alpha\Delta t\left[\left(\frac{1}{\Delta r^2} - \frac{1}{2r_p\Delta r}\right)T_{p-1}^n + \left(\frac{1}{\Delta r^2} + \frac{1}{2r_p\Delta r}\right)T_{p+1}^n\right] \qquad (A.3)$$

Where $= \frac{k}{\rho c_p}$.

3. Using Finite Volume Method for inside boundary cell

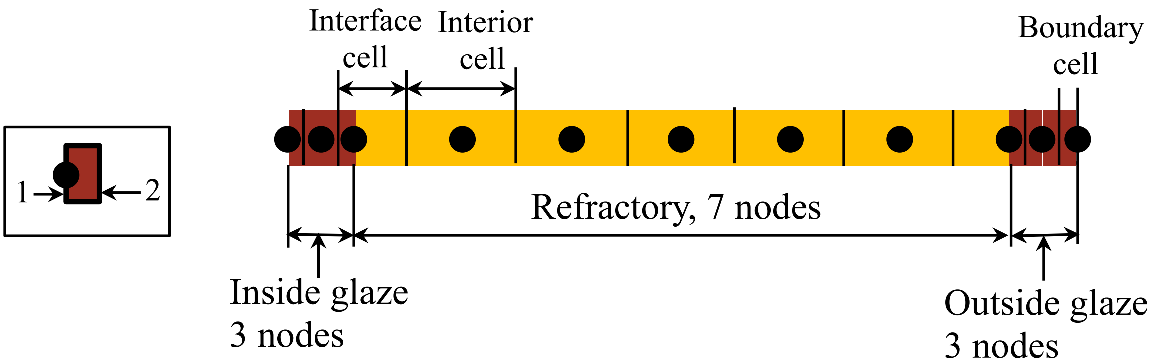

FigA.3 Schematic of inside boundary

Heat balance for inside first cell:

$$\rho C_p V\frac{\partial T}{\partial t} = -kA_2\frac{\partial T}{\partial r}|_2 + h_g A_1 \Delta T|_1$$

$$\rho C_p \varphi z\frac{r\Delta r}{2}\frac{T_1^{n+1} - T_1^n}{\Delta t} = k\varphi z\left(r + \frac{\Delta r}{2}\right)\left(\frac{T_2^n - T_1^n}{\Delta r}\right) + h_g r\varphi z(T_{gas} - T_1^n)$$

$$T_1^{n+1} = T_1^n + \frac{2k\Delta t}{\rho C_p r\Delta r}(r + \frac{\Delta r}{2})\frac{T_2^n - T_1^n}{\Delta r} + \frac{2\Delta t h_g(T_{gas} - T_1^n)}{\rho C_p \Delta r}$$

$$T_1^{n+1} = (1 - \frac{2k\Delta t}{\rho C_p r\Delta r^2}\left(r + \frac{\Delta r}{2}\right) - \frac{2\Delta t h_g}{\rho C_p\Delta r})T_1^n + \frac{2\Delta t h_g}{\rho C_p \Delta r}T_2^n + \frac{2k\Delta t}{\rho C_p r\Delta r^2}\left(r + \frac{\Delta r}{2}\right)T_{gas} \qquad (A.4)$$

Eq.(A.4) is the inside boundary governing equation derived by finite volume method. h_g is the inside convective heat transfer coefficient and T_{gas} is the gas temperature.

4. Using Finite Volume Method for out boundary node

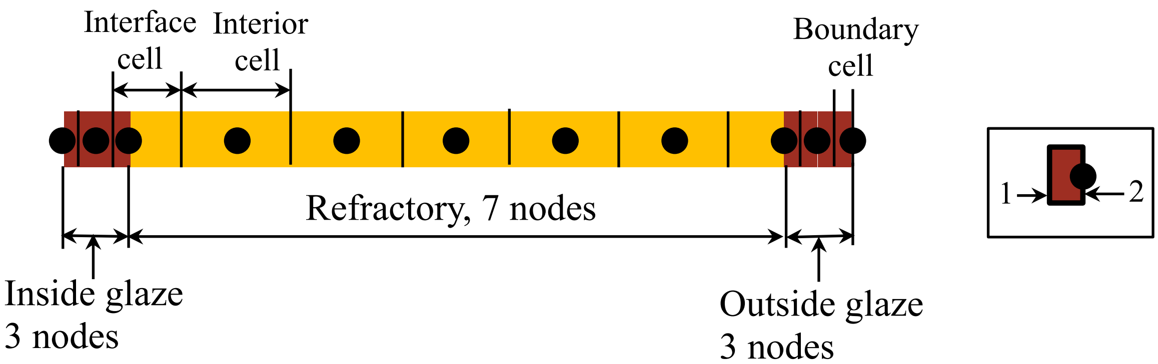

Fig A.4 Schematic of outside boundary cell

Assume the last node number is m. Heat balance for outmost cell:

$$\rho C_p V \frac{\partial T}{\partial t} = kA_1 \frac{\partial T}{\partial r}|_1 - h_a A_2 \Delta T|_2$$

$$\rho C_p \frac{r\Delta r}{2} \frac{T_m^{n+1} - T_m^n}{\Delta t} = k(r - \frac{\Delta r}{2}) \left(\frac{T_{m-1}^n - T_m^n}{\Delta r}\right) - h_a r(T_m^n - T_{air})$$

$$T_m^{n+1} = T_m^n + \frac{2\Delta tk}{\rho C_p r\Delta r}\left(r - \frac{\Delta r}{2}\right)(\frac{T_{m-1}^n - T_m^n}{\Delta r}) + \frac{2\Delta th_a(T_{air} - T_m^n)}{\rho C_p \Delta r}$$

$$T_m^{n+1} = \left(1 - \frac{2\Delta tk}{\rho C_p r\Delta r^2}\left(r - \frac{\Delta r}{2}\right) - \frac{2\Delta th_a}{\rho C_p \Delta r}\right) T_m^n + \frac{2\Delta tk}{\rho C_p r\Delta r^2}\left(r - \frac{\Delta r}{2}\right) T_{m-1}^n + \frac{2\Delta th_a}{\rho C_p \Delta r} T_{air} \qquad (A.5)$$

Eq (A.5) is the out boundary governing equation derived by finite volume method. h_a is the outside convective heat transfer coefficient and T_{air} is the air temperature outside the nozzle.

Eq.(A.1) is the governing equation to solve the transient heat transfer process. Based on this governing equation, using finite volume method, we can get the Eq.(A.2) to Eq.(A.5), which conclude interface, interior and inside outside boundary cells. The basic idea of finite volume method is the heat goes into the cell should be equal to the heat comes out the cell. In the one dimension project, we can only consider the heat flux on r direction.

Inputs and Results

Two cases are performed in this study. In Case 1, the nozzle is only made by refractory, which shown in Table 1 Case 1(glaze has the same properties as refractory). In Case 2, glaze layer is coated at nozzle inner and outer wall, listed in Table 1 Case 2. For 1D Heat Conduction VBA Model and 3D FLUENT Transient Model, the same nodes numbers are applied as listed in Table A.1. All inputs for both cases are listed in Table A.2. Comparing transient temperatures, the error is less than 0.5%. Temperature comparisons for two models at SEN inner and outer wall are plotted in Figure A.5 and A.6 for Case 1 (only refractory) and Case 2 (3 layers).

	VBA and FLUENT Model nodes
inner glaze coating layer	4
wall refractory	37
outer glaze coating layer	4

Table A.1 Nodes numbers for 1D Heat Conduction VBA Model and 3D FLUENT Transient Model

Test conditions		**Input value**	
Initial temperature		20℃	
Inside temperature		600 ℃	
Outside temperature		20 ℃	
Inside heat transfer coefficient		70 W/m^2K	
Outside heat transfer coefficient		20 W/m^2K	
Inside radius		38 mm	
Thickness of glaze layer		1 mm	
Outside radius		76 mm	
Refractory	Heat conductivity	20 W/m K	
	Density	2460 kg/m^3	
	Specific heat	1500 J/kg K	
Glaze		**Case 1**	**Case 2**
	Heat conductivity	20 W/m K	1 W/m K
	Density	2460 kg/m^3	2400 kg/m^3
	Specific heat	1500 J/kg K	1000 J/kg K

Table A.2 Input conditions

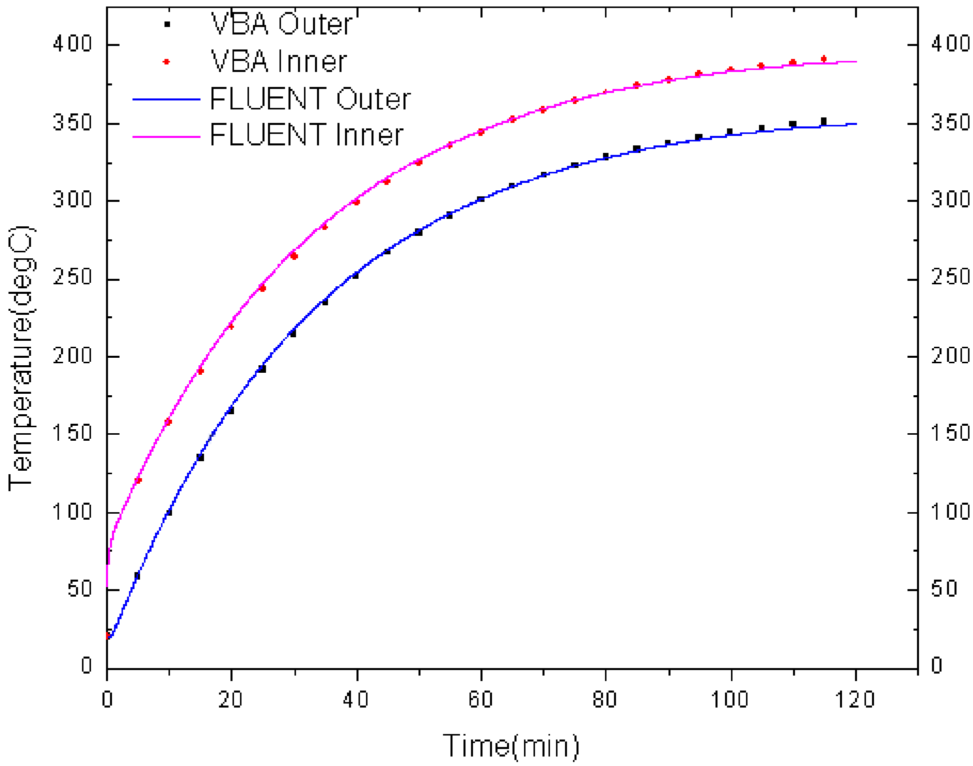

Fig A.5 Comparison of 3-layer VBA model and 3-D FLUENT model predictions of transient temperature in 1-layer nozzle at inner and outer surface

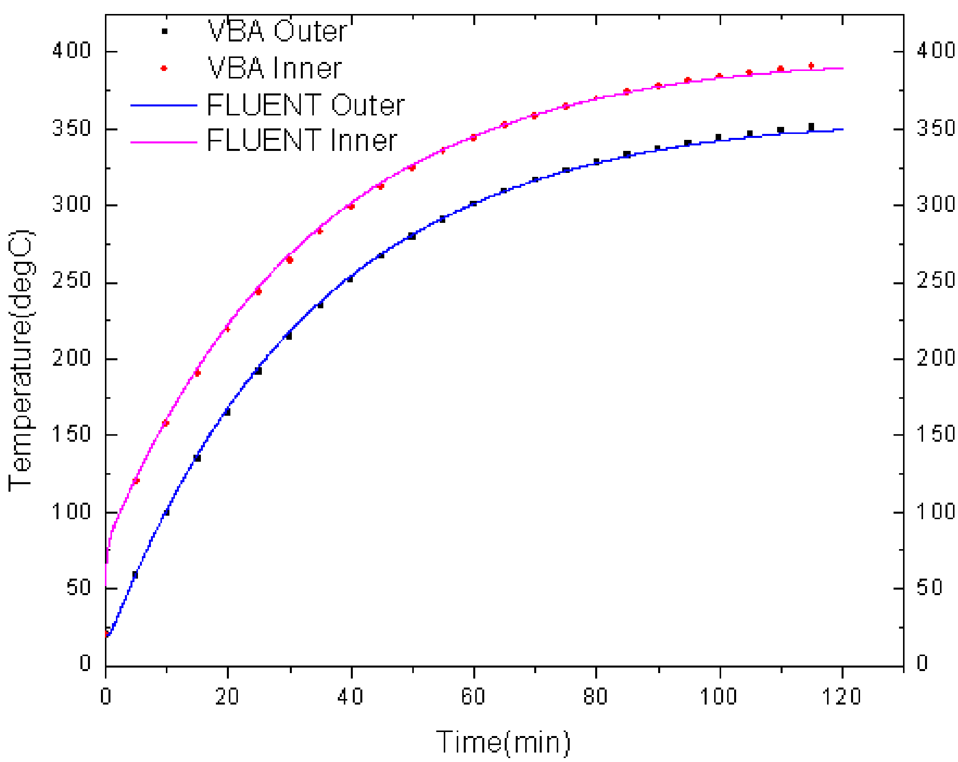

Conclusion

The complete finite volume cell equations for 1-D cylindrical transient heat conduction with layers of different materials and temperature-dependent properties that have been implemented into the final Excel/VBA model are presented.

The model is tested for SEN preheating with 3 layers with different constant properties. The VBA Model results match with FLUENT using an identical mesh within 0.5% error for two cases.

Nomenclature

Symbol	Variable	Unit
V	volume	m^3
t	time	s
Δt	time step	s
r	radius	m
r_w	west node radius	m
r_e	east node radius	m
Δr	neighbor node distance	m
Δr_{PE}	east side node distance	m
Δr_{PW}	west side node distance	m
T	temperature	℃
T_p^{n+1}	temperature of node p at new(n+1) time step	℃
T_p^n	temperature of node p at old (n) time step	℃
T_{gas}	inside gas temperature	℃
T_{air}	outside air temperature	℃
ρ	density	kg/m^3
C_p	specific heat	J/kg K
k	heat conductivity	W/m K
k_w	west side cell conductivity	W/m K
k_e	east side cell conductivity	W/m K
h_g	inside gas convective coefficient	W/m^2K
h_a	out air convective coefficient	W/m^2K

Appendix B

B. Heat Conduction VBA Model comparison with FLUENT UDF Model in preheating and cool down process (Considering temperature dependent properties)

The purpose of this appendix is to validate VBA heat transfer model with FLUENT[1] model with temperature dependent properties in both preheating and cool down processes. Because both processes are considered, the User Defined Function(UDF) is used in FLUENT model to change inner SEN gas/air temperature and heat transfer coefficient in two processes.

Method

Please check "Yonghui VBA Model Governing equation 20120412.docx" file for the theory of VBA heat transfer model. Use Run 2 conditions (inner SEN gas/air) to compare FLUENT and VBA heat transfer Model.

The code of UDF FLUENT model:

```
/*****************************************************************
   UDF makes time dependent inner temperature of SEN in preheating process(t<115min) and
cool down process( 115min<t<392min)
*****************************************************************/
#include "udf.h"
#define TIMEPRE 6900
DEFINE_PROFILE(inner_temperature,thread,i)
{
  real x[ND_ND];
  real y;
  real t=CURRENT_TIME;
  face_t f;

  begin_f_loop(f,thread)
{
F_CENTROID(x,f,thread);
y=x[1];

if(t<TIMEPRE)
F_PROFILE(f,thread,i)=1673.15;
else
F_PROFILE(f,thread,i)=293.15+126*exp(-0.000292*(t-TIMEPRE));
}
  end_f_loop(f,thread)
```

```
}

DEFINE_PROFILE(heat_transfer_coefficient,thread,i)
{
  real x[ND_ND];
  real y;
  real t=CURRENT_TIME;
  face_t f;

  begin_f_loop(f,thread)
{
F_CENTROID(x,f,thread);
y=x[1];

if(t<TIMEPRE)
F_PROFILE(f,thread,i)=400;
else
F_PROFILE(f,thread,i)=20;
}
  end_f_loop(f,thread)
}
```

Input

	Preheat	**Cool down**
Inner gas temperature(K)	1673.15	T=20+126exp(-0.000292(current time –preheat time))
Outer air temperature(K)	293.15	293.15
Inner h_convection (W/m^2K)	400	20
Outer h_convection(W/m^2K)	400	20
Initial temperature(K)	293.15	293.15

Table.B.1 Run 2 conditions

* From "temperature plot for five experiments.xlsx"

Material	Glaze		
Density	2000 kg/m^3		
Properties used in VBA	Temperature(degC)	Thermal conductivity (W/m K)	Specific Heat (J/kgK)
	25	0.8555	835.0425
	200	1.2926	1031.0565
	550	1.5409	1345.6037
	1075	0.8312	1768.4251
	1425	0.0119	2130.1868
Properties used in FLUENT (SI unit)	$k(T)=-0.4856+0.0059T-(5e-6)T^2+(e-9)T^3$		
	$Cp(T)=406.77+1.6781T-0.0009T^2+(3e-7)T^3$		

Table.B.2 Inner and outer layer of SEN

Material	Doloma Graphite
Density	2330 kg/m^3

<table>
<tr><td rowspan="6">Properties used in VBA</td><td>Temperature(degC)</td><td>Thermal conductivity (W/m K)</td><td>Specific Heat (J/kg K)</td></tr>
<tr><td>25</td><td>26.4528</td><td>753.3534</td></tr>
<tr><td>500</td><td>21.8180</td><td>1252.3953</td></tr>
<tr><td>750</td><td>19.7412</td><td>1360.4835</td></tr>
<tr><td>1000</td><td>17.9143</td><td>1422.9122</td></tr>
<tr><td>1500</td><td>15.0106</td><td>1598.2917</td></tr>
<tr><td rowspan="2">Properties used in FLUENT (SI unit)</td><td colspan="3">$k(T)= 29.823-0.0119T+(2e\text{-}6)T^2$</td></tr>
<tr><td colspan="3">$Cp(T)=125.61+2.6275T-0.0019T^2+(5e\text{-}7)T^3$</td></tr>
</table>

Table.B.3 Middle layer of SEN

Location	Radius
inner glaze	38mm
Inner DG	39mm
Outer DG	75mm
Outer glaze	76mm

Table.B.4 Geometry

In order to simulate preheat first and cool down process later, the User Defined Function is used for the inner gas/air temperature (wall boundary) and heat transfer coefficients.

Results

The following figures show temperature comparison of FLUENT model with VBA heat transfer model.

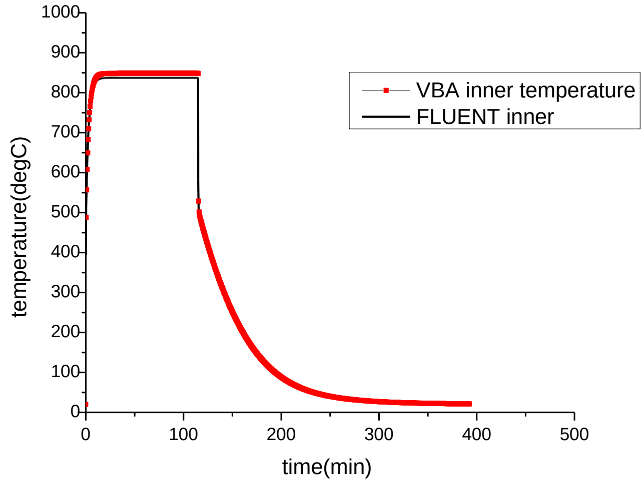

Fig B.1 Inner SEN temperature comparison of VBA and FLUENT Model

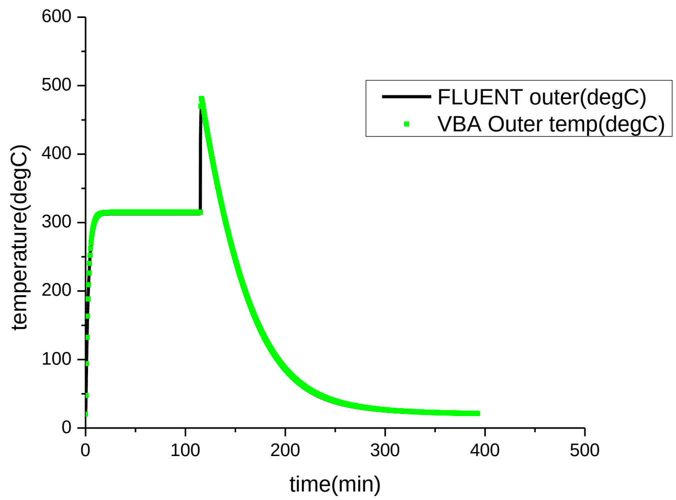

Fig B.2 Outer SEN temperature comparison of VBA and FLUENT Model

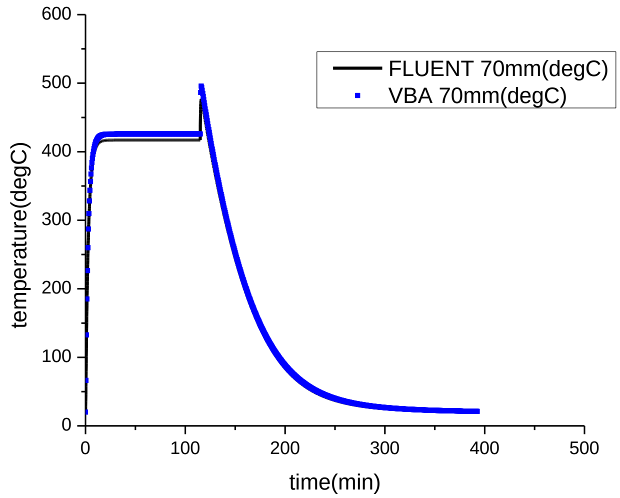

Fig B.3 Temperature at Radius 70mm from centre of SEN VBA
and FLUENT Model comparison

Conclusion

From the figures, the VBA heat transfer model in temperature dependent properties has been validated by FLUENT udf model in preheating and cool down processes.

Appendix C

C. Sensitivity Analysis Report of Preheat Process in SEN Nozzle at Steady State

This sensitivity study is necessary to know which parameter in Yonghui's steady state model affects the temperature inside the nozzle wall most. People often use sensitivity test method to analysis the effect of parameters.

Method

The steady state model is set up in the thermal resistance method. These are the equations being used in the steady state model as follows.

$$TR_{\_in\_total} = \frac{1}{2\pi R_i (h_{\_in\_convect} + h_{\_in\_radi})}$$

$$TR_{\_out\_total} = \frac{1}{2\pi R_o (h_{\_out\_convect} + h_{\_out\_radi})}$$

$$TR_{refractory} = \frac{Ln(\frac{R_{\_out\_refractory}}{R_{\_in\_refractory}})}{2\pi k_{refractory}}$$

$$TR_{\_in\_glaze} = \frac{Ln(\frac{R_{\_in\_refractory}}{R_{\_in\_glaze}})}{2\pi k_{glaze}}$$

$$TR_{\_out\_glaze} = \frac{Ln(\frac{R_{\_out\_glaze}}{R_{\_out\_refractory}})}{2\pi k_{glaze}}$$

$$q = \frac{T_{\_in} - T_{\_out\_air}}{TR_{\_in\_total} + TR_{\_in\_glaze} + TR_{nozzle} + TR_{\_out\_glaze} + TR_{\_out\_total}}$$

$$TR_{measure\ point} = \frac{Ln(\frac{R_{\_out\_glaze} - 10.67}{R_{\_in\_refractory}})}{2\pi k_{nozzle}}$$

$$T_{measure\ point} = T_{\_in} - q.(TR_{\_in\_total} + TR_{\_in\_glaze} + TR_{measure\ point})$$

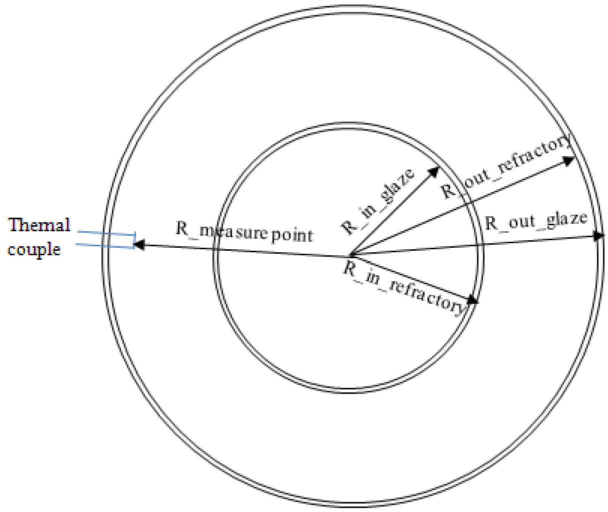

Figure.C.1 Schematic of Steady State Model

Arrows pointed the corresponding temperature are at the some surface. For example, T_out_glaze is the temperature of the surface with R_out_glaze radius.

Approach of Sensitivity Analysis

1) Choose standard conditions of all variables to get standard result
2) For each variable, choose a reasonable engineering estimate of its most extreme value
3) For each variable, calculate a new result using its new value while keeping the same constant standard conditions for all of the others
4) Compare the new results with the standard result

All standard conditions used in the Steady State Radiation Model are listed in Table.C.1.

Independent variable	Standard condition
T_in (℃)	1200
T_out_air(℃)	20
h_in_convect(W/m^2K)	70
h_out_convect	20
Gas emissivity	0.1
Emissivity for glaze and refractory	0.5

k_refractory (W/m K)	20
k_glaze	1
R_in_glaze(mm)	36.6
R_in_refractory(mm)	37.3
R_out_refractory(mm)	77.3
R_out_glaze(mm)	78
T_in_wall(℃) (guess for radiation calculation for uncoupled model)	700
T_out_wall(℃) (guess for radiation calculation for uncoupled model)	550
R_measure point(mm)	67.2

Table.C.1 Standard conditions for Steady State Radiation Model in sensitivity analysis

Results:

Table.C.2 shows the effect of ~15 different variables on the measured TC temperature, relative to standard conditions, which were chosen based on best estimates, but over-predict the measurement by 160C.

Independent variable					Standard(618℃) Diff Temp(℃)	Measured(458℃) Diff Temp(℃)
No.	Xi	Standard	Estimated uncertainty	New condition		
1	T_in (℃)	1200	-500	700	-283	-123
2	T_out_air(℃)	20	-15	5	-4	+156
3	h_in_convect(W/m^2K)	70	-50	20	-154	+5
4	h_out_convect(W/m^2K)	20	-15	5	+115	+275
5	Gas emissivity	0.1	-0.099	0.001	-111	+49
6	Gas emissivity	0.1	+0.4	0.5	+152	+311
7	Emissivity for glaze and refractory	0.5	-0.4	0.1	+120	+280

8	Emissivity for glaze and refractory	0.5	+0.4	0.9	-92	+68
9	k_refractory (W/m K)	20	+20	40	+12	+171
10	k_glaze	1	+1	2	+5	+165
11	k_glaze (glaze is replaced by refractory)	1	+19	20	+10	+170
12	R_in_glaze(mm) (2.7mm inner-glaze thickness)	36.6	-2	34.6	-63	+97
13	R_in_glaze(mm) (no inside glaze layer)	36.6	+0.7	37.3	+24	+184
14	R_in_refractory(mm)	37.3	+2	39.3	-45	+114
15	R_out_refractory(mm)	77.3	-2	75.3	+23	+183
16	R_out_glaze(mm)	78	-0.7	77.3	-6	154
17	R_measure point(mm)	67.2	+2	69.2	-3	157
18	R_measure point(mm)	67.2	-2	65.2	3	163
19	T_in_wall(℃) (guess for radiation calculation for uncoupled model)	700	+3	703	+1	+161
20	T_out_wall(℃) (guess for radiation calculation for uncoupled model)	550	+22	572	-10	+150

Table.C.2 Sensitivity analysis for steady state radiation model

Notes and explanation on the above table:

1. The “standard-diff-temp” column in the above table means the difference between standard result and new estimated variable result. The last column in the above table means the difference between the new result and measurement.

2. Variable No. 1. (row 1 of Table 2) The gas product temperature inside the nozzle, T_in, ranges from 885-1432 C with 1262C average (from "Flame profile across SEN Bore at 1432degC" in LWB report. 500degC is chosen as the estimated uncertainty. The sensitivity result shows that the difference between standard and new estimate is around 300degC. So the gas temperature inside the nozzle is a major variable.

3. The heat convection coefficients of the inside gas and outside air in No. 3 and No. 4 are major variables.

4. I assume the product gas emissivity is quite low in No.5 and high in No.6. The same assumption is made in No. 7 and No. 8. The reason why we cannot simply change gas emissivity into zero is in the following equation, which used to calculate two body radiation emissivity. The second to last column shows that all these four new estimate variables cause around 100degC difference.

In long concentric cylinder, $\frac{A_1}{A_2} = \frac{r_1}{r_2}$ and $F_{12} = 1$
Emissivity equation [1]

$$\varepsilon_{12} = \frac{1}{\frac{1}{\varepsilon_1} + \frac{1-\varepsilon_2}{\varepsilon_2}\left(\frac{r_1}{r_2}\right)}$$, where r_1=r_2

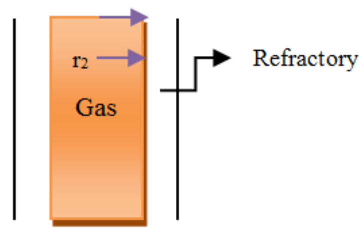

Figure.C.2 Schematic of radiation inside the nozzle

5. No. 9, the reason for the new estimate of conductivity of refractory is 40 W/m K is AG conductivity domain is from 18.2 to 35.5 W/m K. Small difference means that it is a very small effect variable on sensitivity analysis.

6. No. 11, considering the possible replacing glaze by alumina in mistake, I chose the new estimate value of conductivity of glaze to be 20 W/m K. It causes about 10degC difference from the standard result.
7. No. 12 is the case that the actual inside glaze is 2.7mm, 2mm thicker than it should be. This case will cause the temperature at the measured point drops 63degC.
8. No.13 is the case of no glaze at the inside wall, because glaze maybe melt in casting. The difference is small.
9. No. 14 and No. 15 show that the thickness of the refractory is not a major variable.
10. No. 16 is the case that there is no glaze outside the nozzle wall. The difference is small.
11. No.19 and No.20 show the effect of depth of thermocouple. When the depth of the thermocouple shallower or deeper 2mm, the difference between the standard results with the new estimated value result is 3degC. So varying thermocouple depth is a minor effect parameter.
12. No.19 and No.20 are the estimate of possible error in temperature of inside and outside wall. The effect of these two is small.

Thermocouple contact problem sensitive analysis

Account for heat removal through the thermocouples and thermocouple wires, the adjust temperature is given by [2]

$$T_{adjusted} = T_{measured} + \frac{(T_{measured} - T_{out_{air}})d_{gap}\sqrt{h\pi D k_{TC}}}{\sqrt{\pi}k_{air}D/2}$$

where $T_{adjusted}$ is the adjusted measured temperature (^{o}C),

$T_{measured}$ is the measured temperature (^{o}C),

T_{out_air} = 20℃ is the ambient temperature,

d_{gap} is the approximate calibrated air gap thickness (m), assumed to be 0.5 mm.

k_{air} is thermal conductivity of the air gap between the thermocouple tip and the drilled hole, taken as 1 W/m K,

h = 20 W/m² K is the heat transfer coefficient of the air along the TC,

k_{TC} = 200W/mK is the copper-constantan thermocouple thermal conductivity,

D = 4 mm is the thermocouple diameter.

The following is the table of sensitivity analysis for Thermocouple contact problem.

Independent variable					Standard(618℃) Diff Temp(℃)	Measured(458℃) Diff Temp(℃)
No.	Xi	Standard	Estimated uncertainty	New condition		
1	d_{gap}(mm)	0.5	+0.5	1	+1194	+1354
2	k_{gap}(W/m K)	1	+9	10	+60	+219
3	h(W/m^2 K)	20	-15	5	+300	+458
4	k_{TC}(W/m K)	200	-190	10	+134	+293
5	T_{amb}(℃)	20	+200	220	+397	+556

Table.C.3 Sensitivity analysis for Thermocouple contact problem

Discussion

From this sensitive analysis for contact problem of thermocouple, we can see that all these variables affect the measured temperature largely, especially d_{gap}, which is the size of the gap between the thermocouple tip and the mold copper.

Conclusion

- From the table, the sensitivity analysis reveals that the most important variables are: temperature of gas product inside the nozzle; inside gas product convection coefficient; outside air convection coefficient.

- The important variables are: emissivity of gas, emissivity of glaze and refractory and contact problem of thermocouple.
- The unimportant variables are: temperature of the air outside the nozzle, thermal conductivity of glaze and refractory, radius of inside and outside glaze, radius of inside and outside of refractory, location of the thermocouple and the guessed inside and outside wall temperature.

References:

[C.1] Fundamentals of heat and mass transfer, 833
[C.2] L. Hibbeler, Thermocouple comparison report, 2011
[C.3]S.J. Kline, F.A. McClintock, Describing uncertainties in single-sample experiments, Mechanical Engineering, 75 (1953) 3-8.

Nomenclature:

h_in_convect: The convection heat transfer coefficient of the inside nozzle

h_out_convect: The convection heat transfer coefficient of the outside nozzle

h_in_radi: The radiation heat transfer coefficient of the inside nozzle gas

h_out_radi: The radiation heat transfer coefficient of the outside nozzle gas

h_in_total: The sum of convection and radiation heat transfer coefficient of the inside nozzle

h_out_total: The sum of convection and radiation heat transfer coefficient of the outside nozzle

T_in: The gas product temperature of the inside nozzle

T_out_air: The air temperature outside the nozzle

T_in_wall: The temperature of the inside wall of the nozzle

T_out_wall: The temperature of the outside wall of the nozzle

k_refractory: The thermal conductivity of the refractory

k_glaze: The thermal conductivity of the glaze

R_in_glaze: The radius of the glaze at the inside nozzle

R_in_refractory: The radius of the inside of the refractory

R_out_refractory: The radius of the outside of the refractory

R_out_glaze: The radius of the glaze of the outside nozzle

R_measure point: The location of the thermocouple

TR_in_total: The thermal resistance of the convection and radiation inside the nozzle

TR_out_total: The thermal resistance of the convection and radiation outside the nozzle

TR_refractory: The thermal resistance of the refractory

TR_in_glaze: The thermal resistance of the inside of the glaze

TR_out_glaze: The thermal resistance of the outside of the glaze

TR_measure point: The thermal resistance at the measured point

q: heat flux through the nozzle

Appendix D

D. Transient Heat Transfer of Submerged-Entry Nozzle immersion during Continuous Casting

The objective of this appendix is to investigate heat flux from molten steel to SEN inner and outer wall and temperature distribution during casting, when SEN is submerged into molten steel. A finite volume 1D conduction program is implemented to study heat flux at inner and outer wall of SEN and temperature distribution. This study needs to answer the following question: material properties (conductivity) difference effect on heat flux, freezing time; preheating and cool-down time effect on casting heat flux; the correlation between steel superheat and freezing time. In addition, heat flux in high velocity molten steel is compared with low velocity one.

Background

SEN (submerged entry nozzle) is the passageway of molten steel pour down from tundish to mold in continuous casting. So the thermal shock between hot steel liquid with the SEN at room temperature is extremely high. This will cause crack of the SEN and much more impurities enter into the liquid steel and decrease the quality of the steel product. In order to prevent this happening and increase the lifetime of SEN, preheating of the SEN is widely used in industry. Figure 1 shows preheating in experimental condition, which is similar in industry.

After preheated by burning gas for around 2hours, the hot SEN will be transferred from preheating spot to casting mode, which usually takes around 5 minutes. It is called cool-down process. Then SEN will be connected with upper tundish nozzle with slide gate, finally casting process starts. The schematic of continuous casting is shown in figure 2.

In the continuous casting process, clogging is caused by buildup of non-metallic inclusion on the nozzle wall. SEN clogging decreases productivity, increases cost and decreases steel quality. Previous research suggests that heat loss from the nozzle refractories is likely to cause steel solidified in the nozzle [1, 2]. In Araromi [3] paper, he modeled and validated doloma can be used in SEN refractory material to prevent clogging.

In order to improve the SEN quality and avoid clogging, a refractory company produces new Doloma-graphite (DG) SEN instead of traditional Alumina-graphite (AG). But the DG thermal conductivity is smaller (~4 W/mK) than AG. At the place where SEN submerged into molten steel, higher thermal conductivity of SEN increases higher heat flux from the molten steel into SEN wall, which may cause fluid pattern changed and hook structure formed at the short beginning of casting. Lower thermal conductivity of the SEN has lower heat flux, which means less heat loss from the steel at the first beginning, which also means longer time needed to reach steady state of SEN. Then it may cause more steel in defects. In conclusion, it is concerned that conductivity may change the flow pattern and cause steel defects. Other than conductivity of refractory, preheating time, superheat of molten steel, and molten steel fluid velocity are main concerns in casting process.

In order to help refractory designer to understand and improve heat transfer properties in the whole process, the user friendly 1D heat transfer model by using Visual Basic Application Macro code is developed. The model has features: changeable refractory material, changeable SEN geometry and coatings, three processes (preheating, cool-down and casting) time and conditions control and so on. This model preheating and cool down processes was programmed [4, 5] and validated with FLUENT software and experiment. The casting model is validated with FLUENT in one test problem. Zero heat flux boundary conditions at centerline and outer steel should be tested.

Figure.D.1 Preheating experiment photo[6]

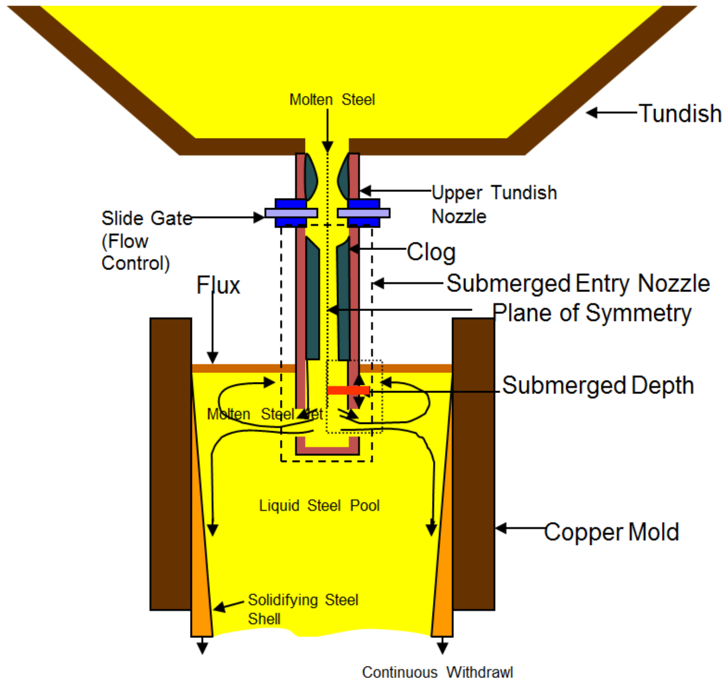

Figure.D.2 Schematic of continuous casting tundish-mold part

Rough Scaling

In 2D heat conduction governing equation:

$$\frac{\partial}{\partial t}(\rho C_p T) = \frac{1}{r}\frac{\partial}{\partial r}\left(rk\frac{\partial T}{\partial r}\right) + \frac{\partial}{\partial z}\left(rk\frac{\partial T}{\partial z}\right)$$

Initial condition: T (t = 0) = T1

Boundary conditions: T(r = 0) = T0; T(r = R) = T0; T (z = 0) = T0; T (z = L) = T0.

Scaling:$r^* = \frac{r}{R}$, $z^* = \frac{z}{L}$, $t^* = \frac{t}{t\_c}$, $\theta = \frac{T-T0}{T1-T0}$

The governing equation can be reformed as: $(\frac{\rho C_p R^2}{k t_c})\frac{\partial\theta}{\partial t^*} = \frac{1}{r^*}\frac{\partial}{\partial r^*}\left(r^*\frac{\partial\theta}{\partial r^*}\right) + (\frac{R^2}{L^2})\frac{\partial}{\partial z^*}\left(\frac{\partial\theta}{\partial z^*}\right)$

Let $t_c = \frac{\rho C_p R^2}{k}$, then the governing equation is $\frac{\partial\theta}{\partial t^*} = \frac{1}{r^*}\frac{\partial}{\partial r^*}\left(r^*\frac{\partial\theta}{\partial r^*}\right) + (\frac{R^2}{L^2})\frac{\partial}{\partial z^*}\left(\frac{\partial\theta}{\partial z^*}\right)$.

and outer wall of SEN can be transformed into a 1-D cylindrical coordinate computational model

If $\frac{R^2}{L^2} \ll 1$, then $\frac{\partial\theta}{\partial t^*} = \frac{1}{r^*}\frac{\partial}{\partial r^*}\left(r^*\frac{\partial\theta}{\partial r^*}\right)$.

In my project, R is the radius of outer molten steel, around 120mm. And L is the length of SEN, around 712mm. So $\frac{R^2}{L^2} = 0.028 \ll 1$. So the heat conduction in r-direction is important, and z-direction conduction is neglected. In conclusion, the approximation of only 1D r-direction heat conduction is reasonable in casting model.

Model Description

<u>Governing Equation</u>

The heat flux at inner and outer wall of SEN can be transformed into a 1-D cylindrical coordinate computational model of transient heat conduction in an SEN wall using the VBA macros in MS excel. Use the Finite Volume Method to discretize explicit governing equations.

Changeable geometry and multiple layers are two of the features in the VBA model. Users expect glaze layers at the inner and outer of SEN refractory. The thermal properties of SEN are temperature dependent.

The discretized equations [7] are listed as following.

Discretized equation for interface cell:

$$T_p^{n+1} = T_p^n + \frac{[\frac{k_e r_e}{\Delta r_{PE}}(T_{P+1}^n - T_p^n) - \frac{k_w r_w}{\Delta r_{PW}}(T_p^n - T_{P-1}^n)]\Delta t}{\left[\rho_w C_{pw}\left(\frac{r_p^2 - r_w^2}{2}\right) + \rho_e C_{pe}\left(\frac{r_e^2 - r_p^2}{2}\right)\right]}$$

Discretized equation for interior cell:

$$T_p^{n+1} = \left(1 - \frac{2\alpha\Delta t}{\Delta r^2}\right)T_p^n + \alpha\Delta t[\left(\frac{1}{\Delta r^2} - \frac{1}{2r_p\Delta r}\right)T_{p-1}^n + \left(\frac{1}{\Delta r^2} + \frac{1}{2r_p\Delta r}\right)T_{p+1}^n]$$

Discretized equation for inner boundary cell:

$$T_1^{n+1} = (1 - \frac{2k\Delta t}{\rho c_p r\Delta r^2}\left(r + \frac{\Delta r}{2}\right) - \frac{2\Delta t h_g}{\rho c_p \Delta r})T_1^n + \frac{2\Delta t h_g}{\rho c_p \Delta r}T_2^n + \frac{2k\Delta t}{\rho c_p r\Delta r^2}\left(r + \frac{\Delta r}{2}\right)T_{steel}$$

Discretized equation for outer boundary cell:

$$T_m^{n+1} = \left(1 - \frac{2\Delta t k}{\rho c_p r\Delta r^2}\left(r - \frac{\Delta r}{2}\right) - \frac{2\Delta t h_a}{\rho c_p \Delta r}\right)T_m^n + \frac{2\Delta t k}{\rho c_p r\Delta r^2}\left(r - \frac{\Delta r}{2}\right)T_{m-1}^n + \frac{2\Delta t h_a}{\rho c_p \Delta r}T_{steel}$$

Simplifying Assumptions

In order to simplify the problem to explore heat flux, several assumptions are made as following.

1) Only conduction in the radial direction

2) Moving liquid steel conductivity is 7 times of solid steel.

3) Inner and outer molten steel domain is far enough to set the boundary temperature as pour temperature.

Initial Conditions

The initial conditions of casting model are from the end temperature distribution in cool-down process. It is necessary to mention the preheating and cool-down schematic and domain, boundary conditions. Force convection at SEN inner bore and outer air natural convection define boundary conditions in both preheating and casting.

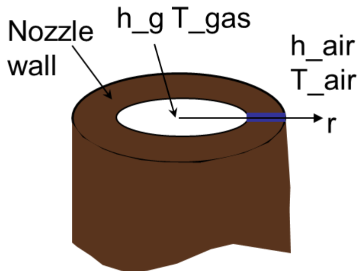

Figure.D.3 Schematic of preheating nozzle

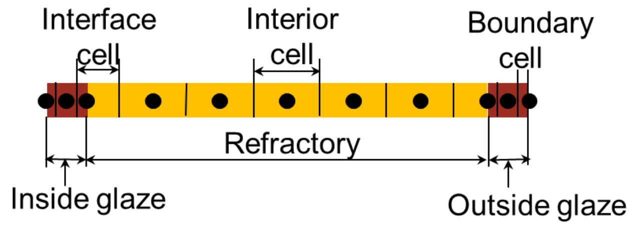

Figure.D.4 preheating & cool-down model domain

Boundary conditions at inner node: $k\frac{\partial T}{\partial r} = h_g \Delta T$

Boundary conditions at outer node: $-k\frac{\partial T}{\partial r} = h_a \Delta T$

Initial conditions in preheating: T(r, t=0) = T_air (19degC)

Initial conditions in cool-down: T = T(r, t=preheating time)

The initial conditions in casting:

T_SEN=T(r, t=cool-down time); T_Steel = pour temperature.

<u>Boundary Conditions</u>

The boundary conditions in casting process are:

T_inner = pour temperature (1550degC)	T_outer = pour temperature (1550degC)

The "inner" and "outer" mean inner and outer boundary in casting model domain, which also shows in Figure. D.5.

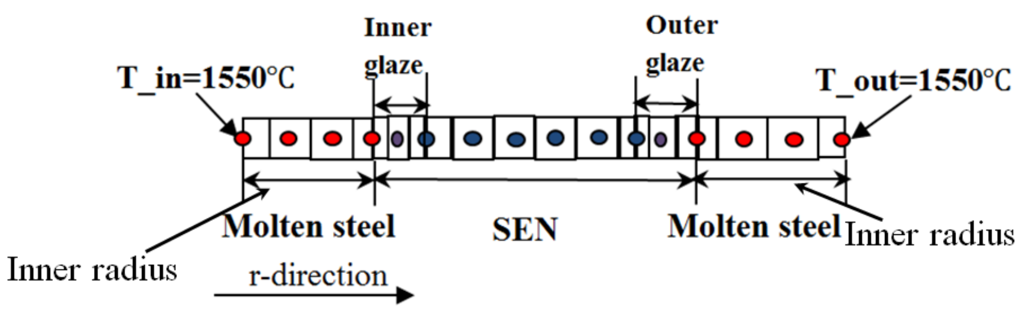

Figure.D.5 Sketch of 1-D conduction casting model domain

<u>Material Properties</u>

Material properties for SEN are listed in table D.1, 2, 3, and ones for molten steel are in Table D.4.

Temperature(degC)	Thermal conductivity(W/m K)	Specific Heat (J/kg K)
25	0.90	821
200	1.20	1035
550	1.67	1281
1075	1.00	1611
1425	0.40	1836

Table D.1 Glaze material properties (2000 kg/m^3)

Temperature(degC)	Thermal conductivity(W/m K)	Specific Heat (J/kg K)
25	26.5	750
500	21.8	1228
750	19.75	1294
1000	17.7	1360
1500	14.6	1481

Table D.2 Doloma-Graphite material properties (2330 kg/m^3)

Temperature(degC)	Thermal conductivity(W/m K)	Specific Heat (J/kg K)
25	35.5	708
500	25.5	1282
750	23.2	1376.5
1000	20.9	1471
1500	18.2	1595

Table D.3 Alumina-Graphite properties (2460 kg/m^3)

Density (kg/m^3)	7015
Thermal conductivity (W/m K) of liquid	231
Thermal conductivity (W/ m K) of solid	33
Specific Heat (J/kg K)	682
Thermal Diffusivity (m^2/s)	0.0055

Table D.4 Molten Steel material properties

<u>Complete conditions for every run</u>

VBA Input conditions	Value	Source
Initial temperature	19 ^oC	LWB measurements
Inner gas temperature	885-432*Exp (-time in second/1066) (^oC)	Concluded from gas temperature histories from experiment
Outer air temperature	19 ^oC	LWB Experiment data
Inner h_convection	50.89 W/ m2K	Combustion Model result

Outer h_convection	35.25 W/ m^2K	Combustion Model result
Emissivity of outer glaze	0.82	LWB Emissivity Testing
Emissivity of inner flame	1	Black body of inner SEN
Thermal properties	Table 4,5,6	LWB measurements
Preheat time	114.5	LWB Experiment data

Table D.5 VBA Preheating Model input conditions

VBA Input conditions	Value	Source
Initial temperature	Temperature at the end of preheating	Preheating VBA model
Inner gas temperature	20+126*Exp (-time in second*2.92e-4) (^{o}C)	Concluded from gas temperature histories from experiment
Outer air temperature	19 (^{o}C)	LWB Experiment data
Inner h_convection	7.54 W/ m^2K	Churchill & Chu Equation[9] [10]
Outer h_convection	7.24 W/ m^2K	Churchill & Chu Equation
Thermal properties	Table 4,5,6	LWB measurements
Cool-down time	4.5 min	LWB Experiment data

Table D.6 VBA Cool-down Model input conditions

VBA Input conditions	Value		Source
Initial temperature	Temperature at the end of cool-down		Cool-down VBA model
Pouring temperature	1550 ^{o}C		
Solidification Temperature	1525 ^{o}C		
Outer air temperature	19 ^{o}C		LWB Experiment data
Thermal properties	DG case	Table 1,2,4	LWB measurements
	AG case	Table 1,3,4	
Casting time	80 min		Approximately
Time step	0.001s		

Table D.7 VBA Casting Model input conditions

The convergence criteria used in 1D conduction model is: thermal diffusivity*dt/(dx*dx) < 0.5. Due to small cell size in the glaze layer and explicit algorithm, the time step is 0.001s approximately. Casting VBA Model 60mins process simulations took 10 min to run on 4GB 64-bit Operating System.

<table>
<tr><td>Cell size</td><td>Inner glaze</td><td>Refractory</td><td>Outer glaze</td><td>molten steel</td><td>time step</td></tr>
<tr><td>Preheating</td><td rowspan="3">0.175mm</td><td rowspan="3">1mm</td><td rowspan="3">0.175mm</td><td rowspan="2">None</td><td>0.0015s</td></tr>
<tr><td>Cool-down</td><td>0.0016s</td></tr>
<tr><td>Casting</td><td>0.375mm</td><td>0.0010s</td></tr>
</table>

Table D.8 Cell size and time step for each process

Mesh Study

The cell size of glaze layers effect the results a lot. The least number of nodes in glaze layer is 3, with this number; the preheating temperature is unreasonable, and far away from validated result. While, when the nodes number is equal or larger than 5, the preheating temperature matches with preheating experiment result. So the least number of node in glaze layers is 5.

	Inner glaze No. of nodes	Refractory No. of nodes	Outer glaze No. of nodes
Case 1	5	38	5
Case 2	3	38	3

Table D.9 Mesh study in preheating process of DG

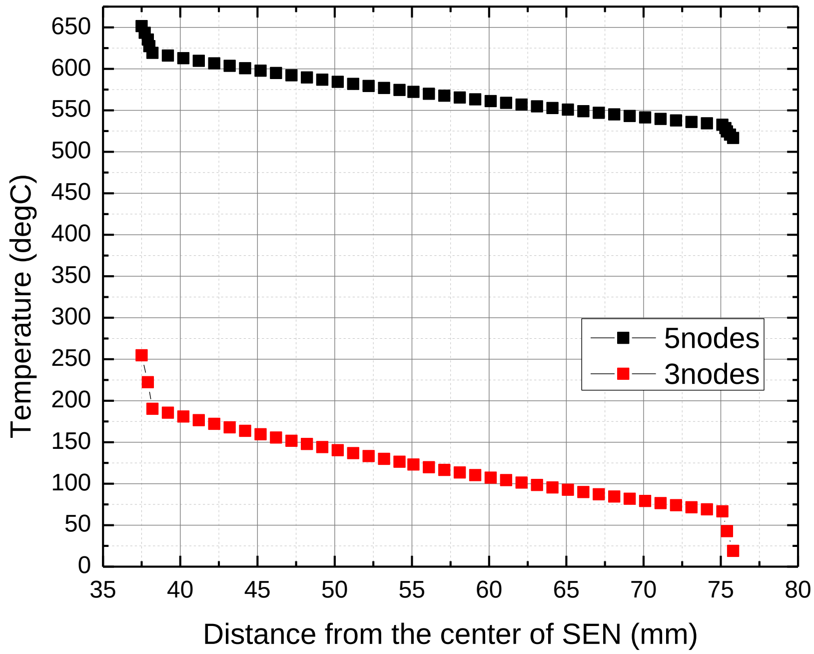

Figure D.6 Temperature comparisons of case 1&2 for mesh study in preheating

Model validation

For the 1D heat conduction model, I will program by using Visual Basic Application Micro in MS office excel, because the user friendly interface feature and light computation task in one dimension.

FLUENT 3D transient model with same size and number of mesh, properties, and conditions is used to validate VBA model. The initial temperature of the test problem is 500 ^{o}C in whole domain except two boundaries. The FLUENT model has been validated in “glaze-refractory-glaze” SEN heat conduction model with temperature dependent properties and convection boundary conditions. The test problem conditions, mesh schematic and validated results are listed as following.

<table>
<tr><th colspan="2">Test conditions</th><th>Input value</th></tr>
<tr><td colspan="2">Initial temperature</td><td>500℃</td></tr>
<tr><td colspan="2">Inner steel temperature</td><td>1550 ℃</td></tr>
<tr><td colspan="2">Outer steel temperature</td><td>1550 ℃</td></tr>
<tr><td colspan="2">SEN inner radius</td><td>38mm</td></tr>
<tr><td colspan="2">Thickness of inner glaze layer</td><td>1 mm</td></tr>
<tr><td colspan="2">Thickness of refractory</td><td>36 mm</td></tr>
<tr><td colspan="2">Thickness of outer glaze layer</td><td>1 mm</td></tr>
<tr><td colspan="2">SEN outer radius</td><td>76 mm</td></tr>
<tr><td colspan="2">Outer steel radius</td><td>114mm</td></tr>
<tr><td colspan="2">Time step</td><td>0.001s</td></tr>
<tr><td colspan="2">Time duration</td><td>1min</td></tr>
<tr><td rowspan="3">Steel</td><td>Heat conductivity</td><td>231 W/m K</td></tr>
<tr><td>Density</td><td>7015 kg/m^3</td></tr>
<tr><td>Specific heat</td><td>682 J/kg K</td></tr>
<tr><td>Glaze</td><td colspan="2">As Table 12.</td></tr>
<tr><td>Doloma-Graphite</td><td colspan="2">As Table 11.</td></tr>
</table>

Table D.10 Test conditions for test problem in both FLUENT and VBA Model

Temperature(degC)	Thermal conductivity(W/m K)	Specific Heat (J/kg K)
25	26.45	753.35
500	21.82	1252.40
750	19.74	1360.48
1000	17.91	1422.91
1500	15.01	1598.29
Properties used in FLUENT	k(T)=(2e-6)T^2-0.0119T+29.823	$Cp(T)=125.61+2.6275T-0.0019T^2+(5e-7)T^3$

Table D.11 Doloma-Graphite material properties (2330 kg/m^3)

Temperature(degC)	Thermal conductivity(W/m K)	Specific Heat (J/kg K)
25	0.86	835.04
200	1.29	1031.06
550	1.54	1345.60
1075	0.83	1768.43
1425	0.01	2130.19
Properties used in FLUENT (SI unit)	$k(T)=-0.4856+0.0059T-(5e-6)T^2+(e-9)T^3$	$Cp(T)=406.77+1.6781T-0.0009T^2+(3e-7)T^3$

Table D.12 Glaze material properties (2000 kg/m^3)

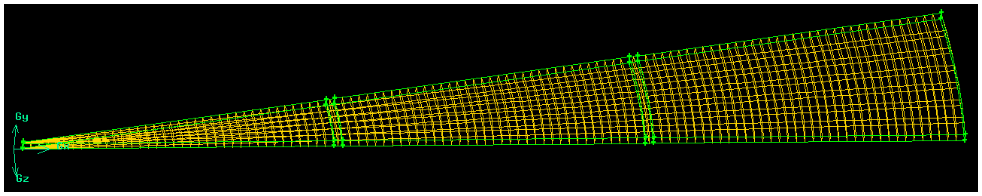

Figure D.7 Test problem mesh schematic in FLUENT

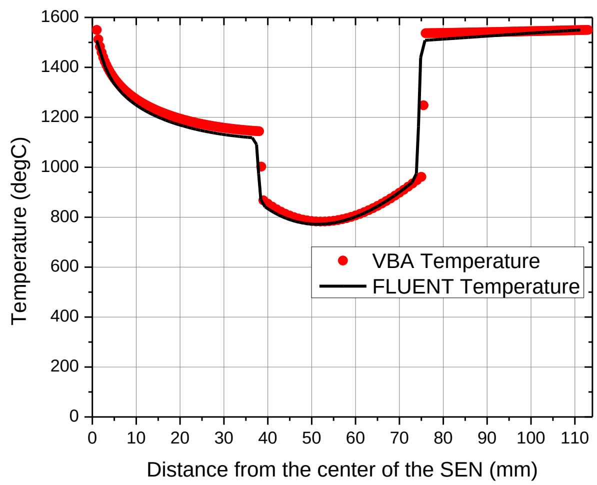

Figure D.8 Comparison of FLUENT and VBA transient test problem after 1min

Results

<u>Preheating results</u>

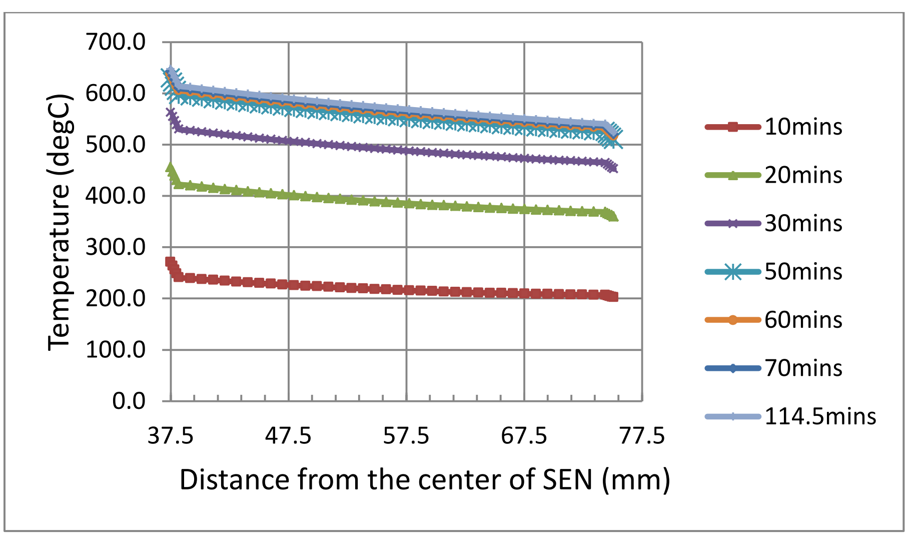

Figure D.9 AG Preheating Process Temperature History

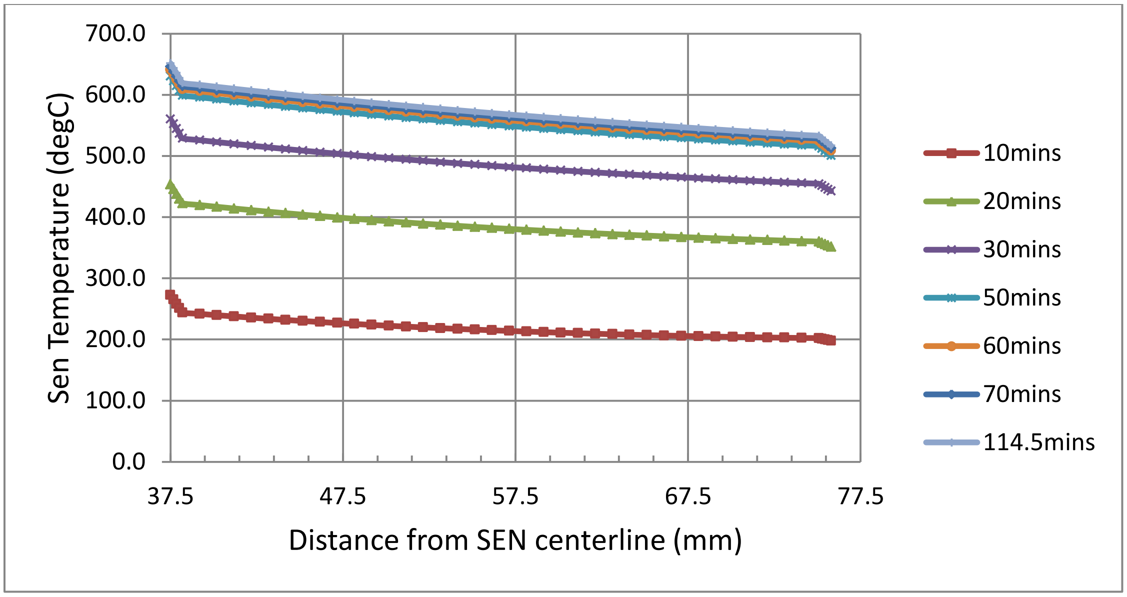

Figure D.10 DG Preheating Process Temperature History

<u>Cool-down results</u>

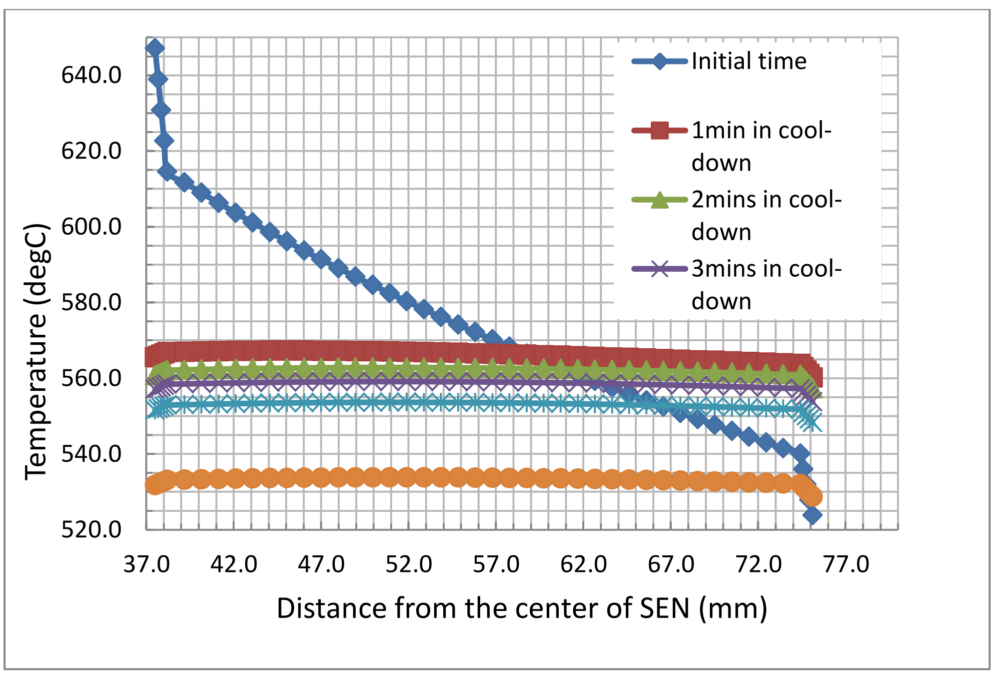

Figure D.11 AG Cool-down process temperature history

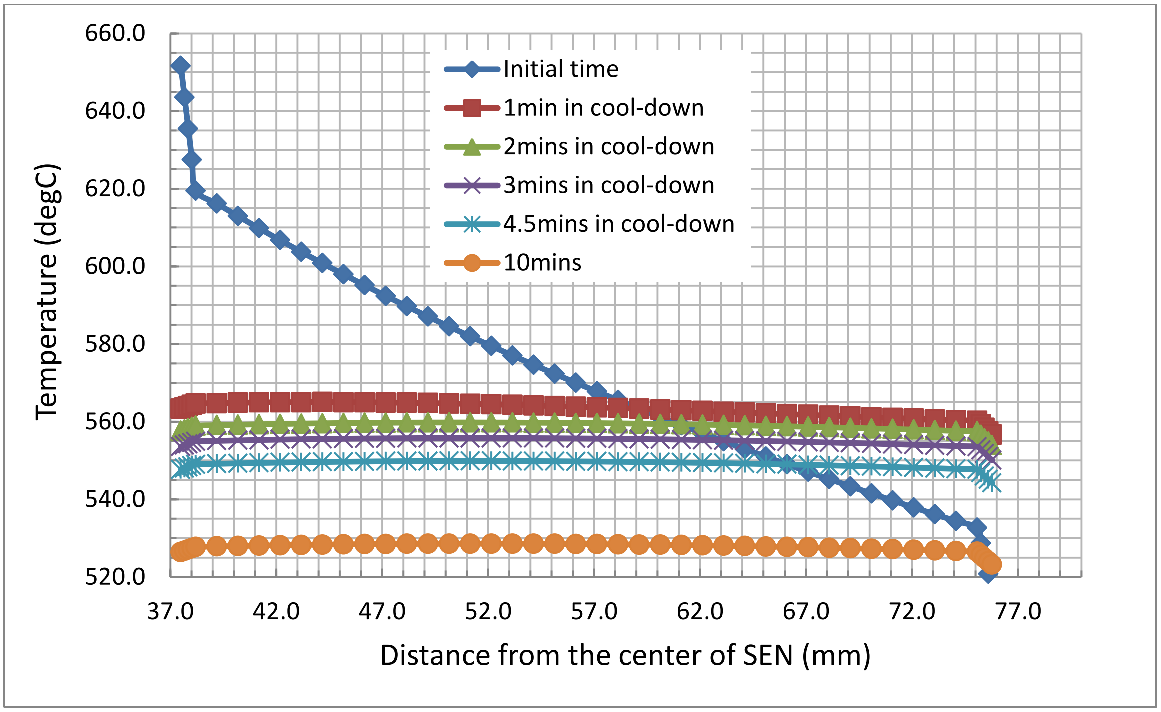

Figure D.12 DG Cool-down process temperature history

<u>Casting results</u>

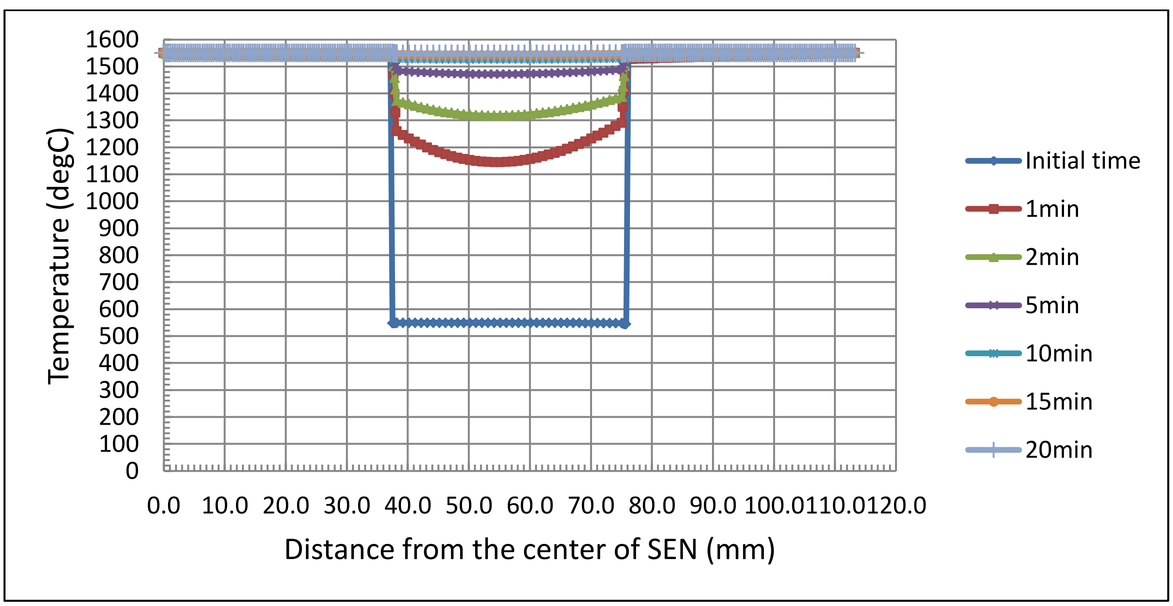

Figure D.13 DG transient temperature distribution in casting

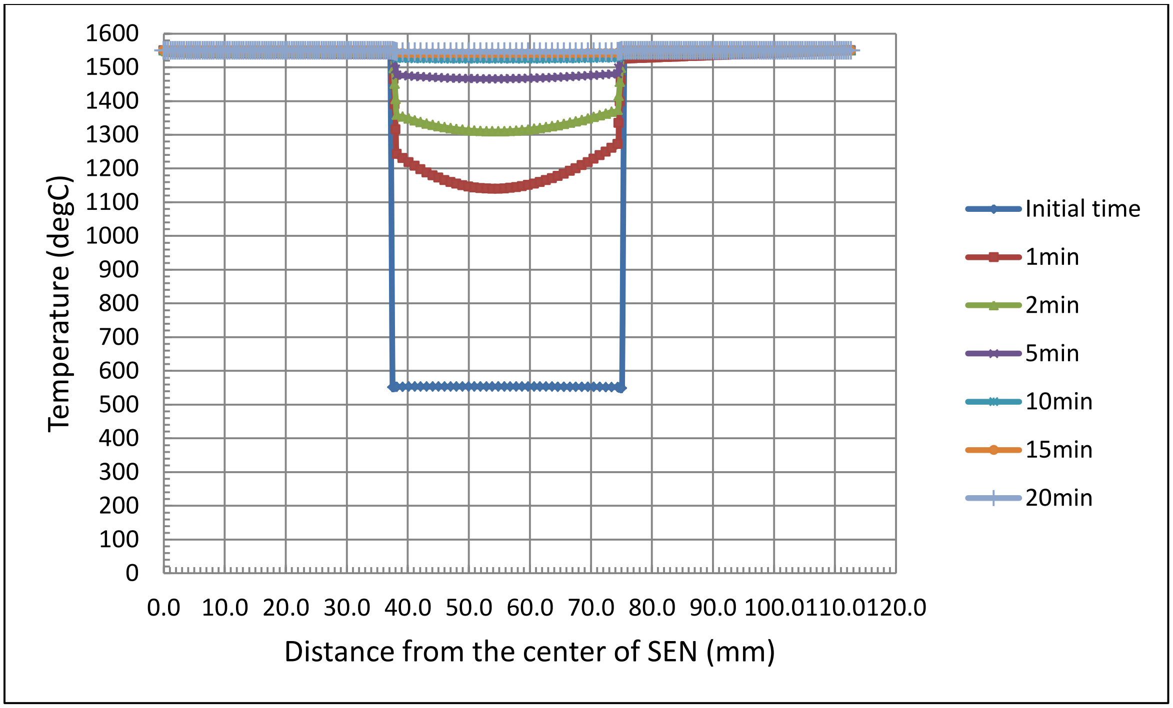

Figure D.14 AG transient temperature distribution in casting

In Figure D.13 &14, the temperature changes rapidly at the beginning of casting, the minimum temperature in SEN jumps from about 560degC to 1120degC in the first one minute for both AG and DG material. Compared with difference of minimum temperature in DG SEN from 2min to 5min, it only changes 152degC, from 1320degC to 1472degC. In addition, temperature profile at 15min almost overlaps with 20min distribution, which means casting process almost reaches steady state. From the casting VBA model results, all components in the model domain reach pour temperature at 45mins for AG case, 42min for DG case. Moreover, outer SEN tends to higher temperature during casting. This is because outer molten steel contains more energy.

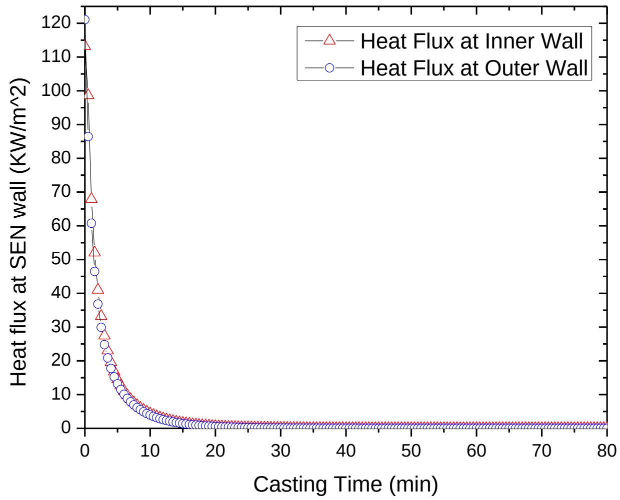

Figure D.15 Heat Flux of DG SEN at inner and outer wall in casting

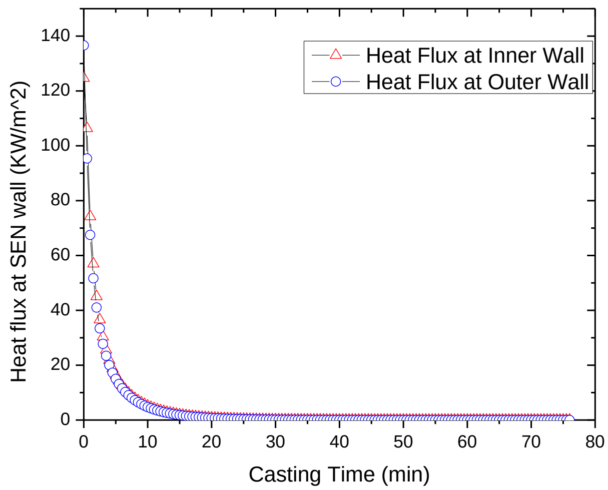

Figure D.16 Heat Flux of AG SEN at inner and outer wall in casting

From Figure D.15 & 16, the maximum heat flux appears at the beginning of casting, and decreases exponentially. The heat flux drops dramatically at the beginning of casting, then decreases slows as time goes on. The heat flux at wall is calculated by two adjacent cells in glaze layer. In DG case, after 42mins, the heat flux on both side walls reaches zero, which also means casting process reaches steady state. While in AG case it will take 45mins. The beginning heat flux of AG is 20KW/m^2 bigger than DG case.

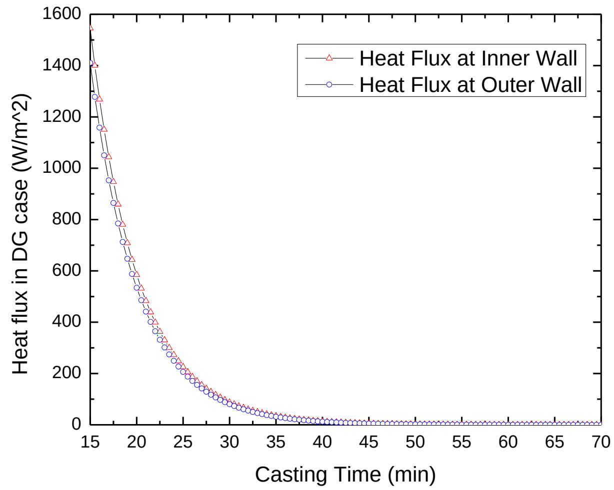

Figure D.17 Zoomed in heat flux of DG SEN at inner and outer wall

Figure D.17 shows after 15mins casting, heat flux at inner wall decreases to 1545.8W/m^2, outer wall is 1410 W/m^2. With the casting goes on, the difference between outer and inner wall heat flux decreases. Finally, casting domain reaches steady state at 42mins.

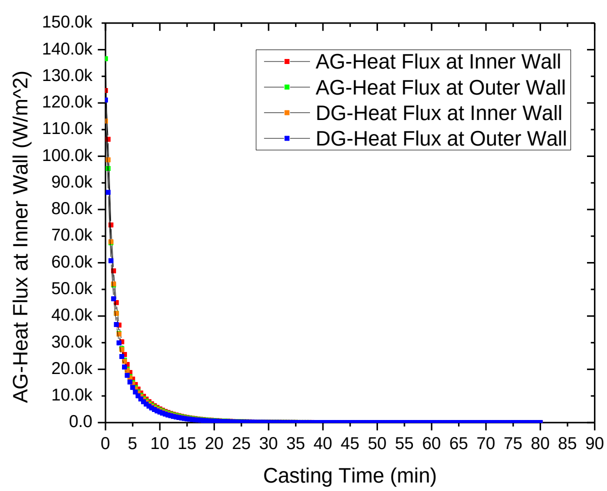

Figure D.18 Comparison of AG and DG SEN at inner and outer wall in casting

Figure D.18 shows the similar heat flux profile of AG and DG SEN.

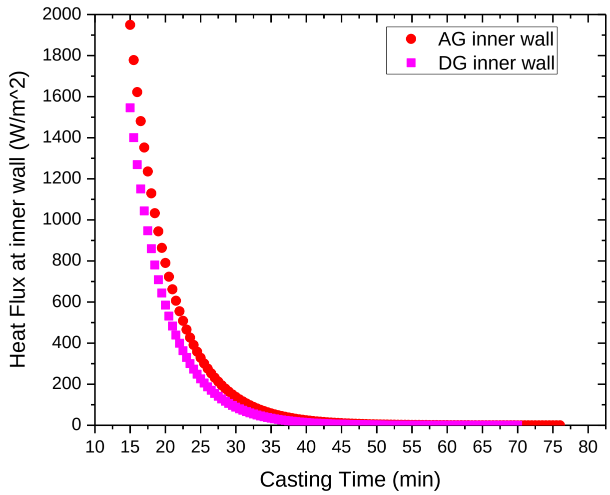

Figure D.19 Zoomed in heat flux at AG and DG SEN at inner wall

From Figure D.18, it displays that the heat flux of AG is larger than DG at inner wall all. In the zoomed in figure 19, even at 15mins, the heat flux difference is 400 W/m^2. But both material heat fluxes go to zero around same casting time, 42-45mins. So lower conductivity material refractory cause lower heat flux at wall, but will not prolong time to reach steady state.

Parametric study

<u>Preheating time</u>

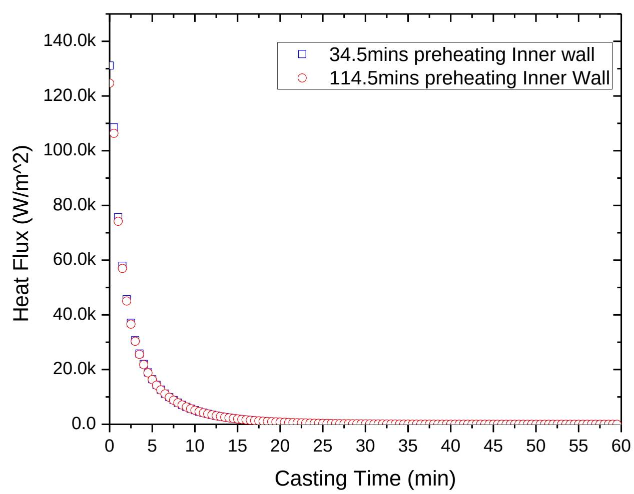

Figure D.20 Heat Flux Comparison between inadequate and steady state preheating of DG SEN

In experiment conditions of AG, the preheating model reaches steady state at around 70mins. So 34.5mins preheating is inadequate. From Figure 20, the heat flux at inner wall of inadequate preheating is larger than steady state one. In addition, the difference becomes smaller with casting time increasing.

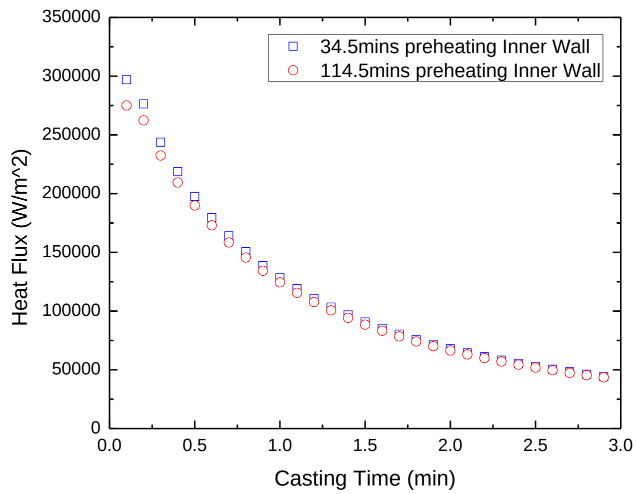

Figure D.21 Zoomed in Heat Flux Comparison between inadequate and steady state preheating of DG SEN

Zoom in the first 3mins heat flux comparison between 34.5mins and 114.5mins preheating. From Figure 21, the biggest heat flux difference between inadequate and steady state preheating is at the beginning of casting: 0.1min. The heat flux difference at 0.1min is around 50KW/m^2. After 3mins, the heat flux difference is 369 W/m^2, which seems tiny in this figure.

Remelt time

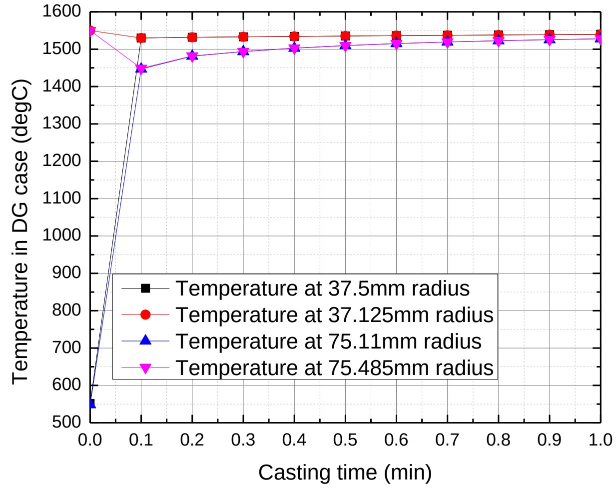

Figure D.22 Temperature distributions at inner and outer DG SEN wall and adjacent steel cell

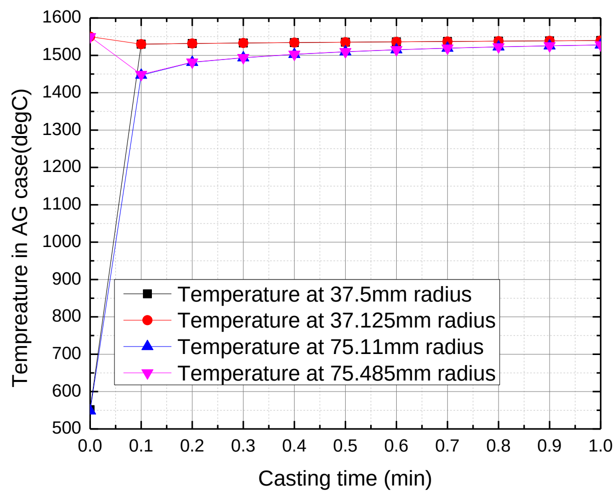

Figure D.23 Temperature distributions at inner and outer AG SEN wall and adjacent steel cell

In Figure 22 & 23, temperature distributions at inner and outer DG & AG SEN wall and adjacent steel node are plotted. In DG case, 37.5mm is inner SEN radius, 37.125mm is the inner adjacent steel node, 75.11mm is outer SEN radius, and 75.485mm is the outer adjacent steel node. For AG case, the outer SEN radius is 75.11mm, and 75.485mm is the outer adjacent steel node. Both inner and outer wall temperature increases dramatically from around 560degC to about 1500degC in the first two minutes. And the adjacent steel temperature decreases first and increases later.

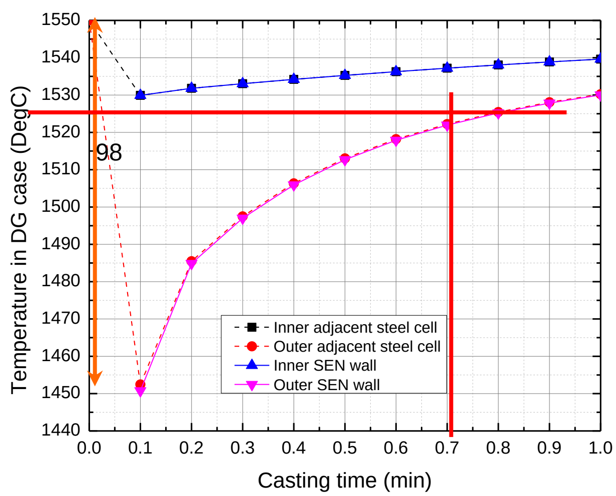

Figure D.24 Temperature distributions Zoom in DG SEN wall and adjacent steel cell

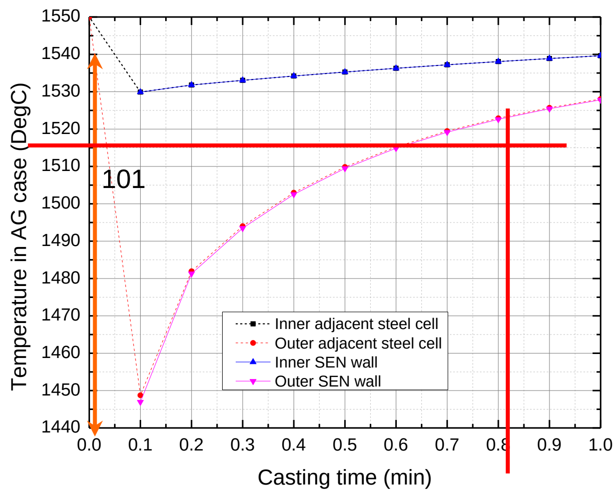

Figure D.25 Temperature distributions Zoom in AG SEN wall and adjacent steel cell

In Figure D.24 & 25, zoomed in temperature history at the first 1min of casting are shown. For DG case, at 0.8mins, the temperature at outer wall adjacent cell reaches back to 1525.5degC, above solidification temperature. So the remelting happens at 0.8mins in DG case. For AG case, at 0.9mins, the temperature at outer wall adjacent cell reaches back to 1525.7degC, above solidification temperature. The pour temperature is 1550degC. For DG case, in order to avoid freezing, 98degC higher temperature is needed. And for AG case, it is 101degC. Both AG and DG cases, remelting happens before 1min in casting, and the temperature is always above solidification temperature at the node of molten steel adjacent to inner wall.

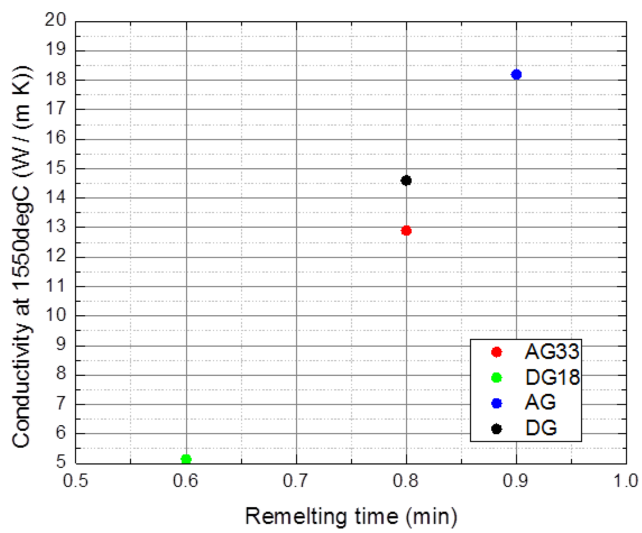

Figure D.26 Temperature distributions Zoom in AG SEN wall
and adjacent steel cell

In order to understand the material conductivity effect on remelting, Figure 26 is obtained by running AG33 and DG18 material in the same conditions as DG. The material properties of AG33 and DG18 are in appendices. These two materials are commonly used to make SEN refractory. From these total four samples, the remelting time is always within 1min, for conductivity at 1550degC at the range of 5-18.3W/m K.

<u>Superheat VS. Remelting time</u>

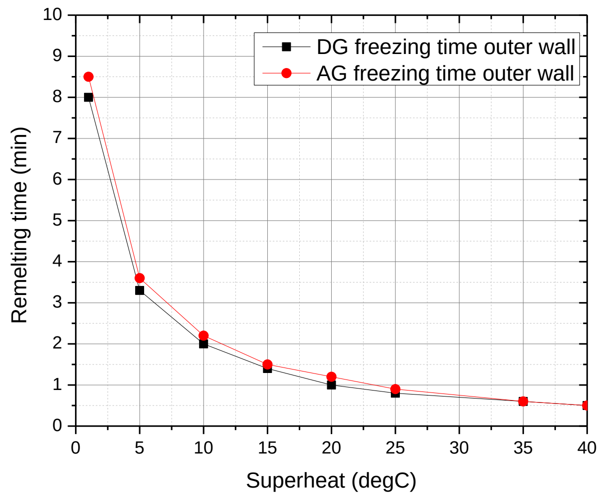

Figure D.27 Correlation between Superheat and Remelting time in AG and DG

Figure D.27 illustrates DG freezing time is slightly shorter than AG under same conditions. The lower the superheat of molten steel, the longer time it takes to remelt. Take 35degC superheat as an example, with solidification temperature 1525degC, then the pour temperature is 1560degC. The freezing time is around 0.53min. With 25degC superheat, the freezing time is smaller than 0.9min. From 1degC to 5degC superheat, the freezing time drops more than 5mins. But from 10degC to 15degC, the freezing time only decreases 0.5mins. So the higher the superheat is, the less effect on shorting freezing time.

High speed (liquid) steel VS. Low speed (solid) steel

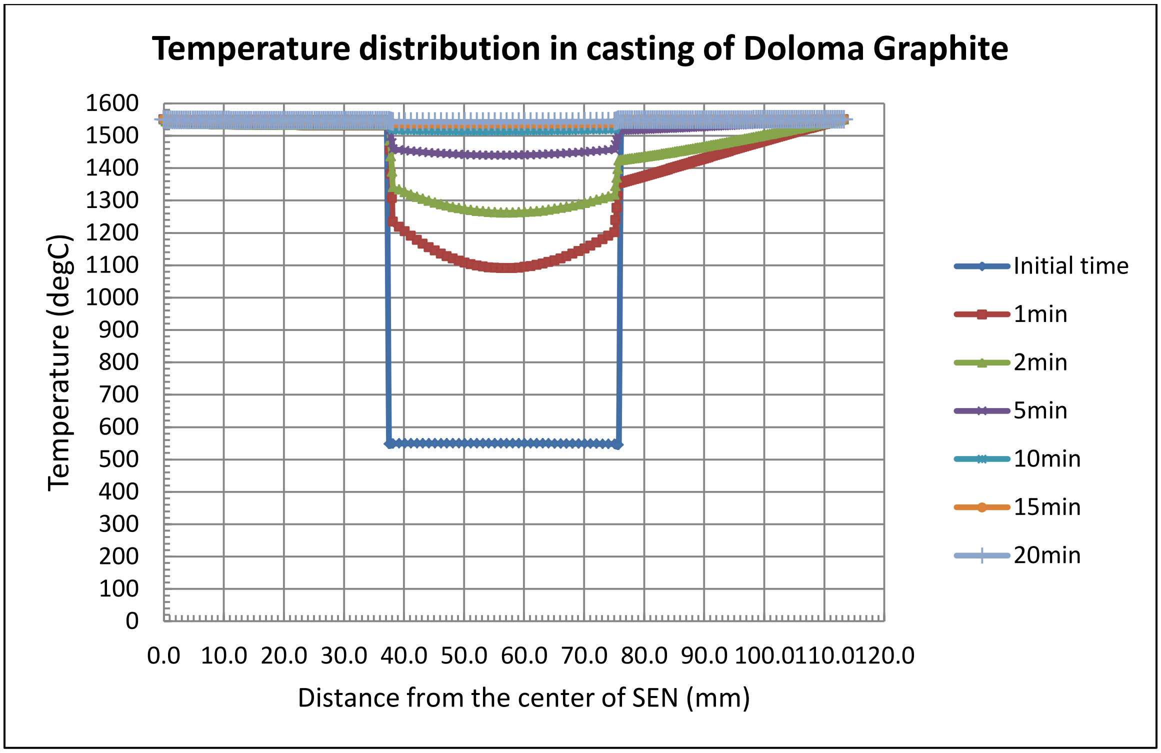

Figure D.28 Low speed steel in DG case, with solid steel conductivity

By using the conductivity of solid steel under same conditions as DG case, temperature history is obtained in Figure 28. The outer SEN wall temperature is much lower than pour temperature. For example, in 1min casting, the outer wall temperature is around 200degC lower than pour temperature. It is around 175degC lower than liquid steel (DG or AG) case.

Cool-down time

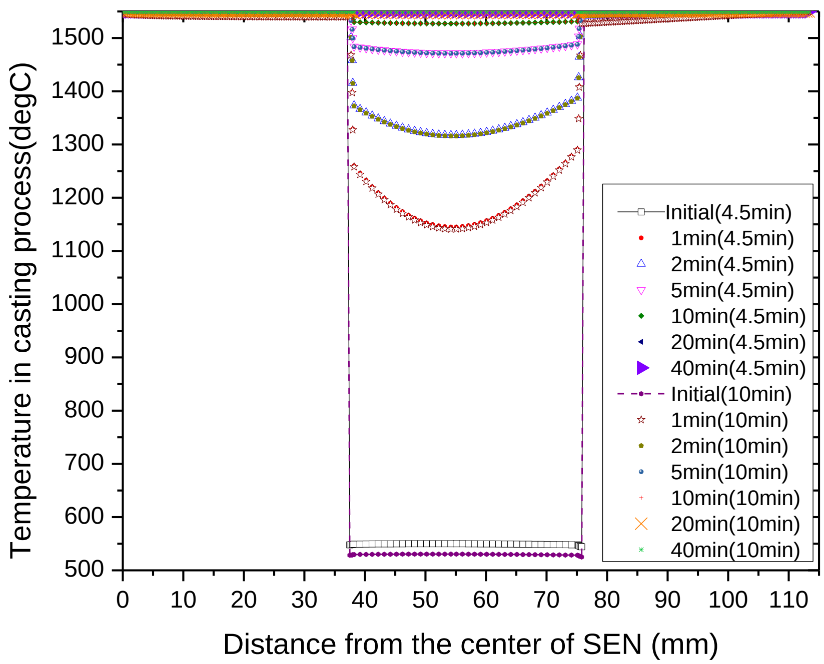

Figure D.29 Comparisons of 4.5min Vs.
10 min cool-down process effect in casting temperature

By changing cool-down time in DG case, casting temperature history comparisons between 4.5min and 10min is obtained in Figure 29. From Figure 12, we could see clearly that the temperature difference between two cool-down processes is around 20degC. Figure 29 illustrates that all corresponding sample time temperature profiles overlap. So the casting process is not affected by cool-down time changed from 4.5min to 10min.

Discussions

From rough scaling, the assumption that only r-direction conduction needs simulating is proofed. The mesh study is very important due to reveal the nodes number in glaze layers change results a lot.

From the preheating and cool-down temperature distribution, the temperature drops in the inner and outer glaze layers are much bigger than refractory layer. The reason is much lower conductivity (0.40W/m K at 1425degC) of glaze layer, compared with refractory conductivity (14.6 W/m K at 1500degC), which makes higher thermal resistance. Then bigger temperature drop is required to keep the same heat flux through each layer.

In the casting temperature history, the right side temperature is not symmetrical to the left one. The reason is outer steel contains more energy than inner steel, due to difference on volume, which will cause outer SEN receives more energy than inner part.

The heat flux at the beginning of casting is very large, around 120-140 KW/m K. The heat flux drops in exponential pattern dramatically in the first 15mins. During this time, the steel fluid pattern may be changed and hook structure may form.

The heat flux of AG case is larger than DG case. The conductivity of AG is larger than DG, then the thermal resistant of AG SEN is smaller than DG. At the constant temperature boundary conditions, the higher heat flux is in the AG case, shown in Figure 19. On average, AG conductivity is 4 W/m K larger than DG. But both cases reach steady state in casting before 45mins. And also, the remelting time for both cases is below 1min. So lower conductivity SEN has lower heat flux, with almost the same time needed to reach steady state in casting. If DG SEN can prevent clogging better than AG, then DG material is highly recommended based on my studies.

The inadequate preheating causes higher heat flux in casting process. For my study in Figure D.20 & 21, half time of needed in preheating will cause 50 KW/m K higher heat flux than steady state preheating, which may cause hook structure. In order to avoid this, more than 1.5 hours preheating is recommended.

Based on Figure D.22-25, inner SEN wall and adjacent steel do not freeze all the time during casting. While, the outer adjacent wall steel freezes from the beginning of casting to 0.8 or 0.9 min. From the reality, the inner SEN port is not freezing due to hot (close to pour temperature) steel always coming. But the outer SEN steel may freeze a while due to lower convection of hot steel and lost heat to SEN and shell. From Figure D.26, it shows freezing at the outer SEN adjacent steel is not concerned with common range refractories.

Figure D.27 shows DG SEN freezing time is slightly shorter than AG case. And the higher the superheat is, the less effect it is on shortening remelting time. In addition, it provides a chart for casting operator to get the acknowledge of remelting time based on the superheat. In order to predict more accurate on plant operation, the clogging of upper tundish nozzle and SEN, the radiation, convection, heat loss from slide gate etc. are needed in this model.

The temperature of outer SEN steel is very peculiar. At the end of the outer steel, the heat flux is not close to zero, then it is not reasonable to force the boundary condition to be constant temperature. In order to fix this problem, two means are possible: the longer domain, heat flux boundary conditions.

From Figure D.29, casting process is not effected by cool-down time changed from 4.5min to 10min.

Conclusions

- The heat flux from molten steel to SEN wall at casting process, from beginning to 15mins, decreases from 120 KW/m^2 to 1600 W/m^2. It may cause significant effects on fluid pattern.
- The heat flux and temperature change faster at the beginning the casting process, and reach steady state at around 45mins.
- Lower conductivity refractory causes lower heat flux from molten steel to SEN wall.
- Inadequate preheating (34.5mins) causes higher heat flux at the beginning of casting. After 3mins, there is no significant difference between inadequate and steady state preheating. The higher the preheating temperature is, the lower heat flux is.
- Freezing only happens in the outer SEN wall, after 0.9mins, the freezing disappears in both AG & DG cases.
- Casting temperature is slightly changed by 4.5min or 10min cool-down process.

Implementation

- Under the assumption that DG SEN can prevent clogging better than AG, DG material is highly recommended based on lower heat flux and almost the same time to reach steady state in casting.
- More than 1.5 hours preheating is recommended. Insulation layer and outer box are recommended to increase SEN temperature.
- The conductivity of SEN refractory is not the main factor to change remelting time. But lower conductivity needs shorter remelting time. So lower conductivity refractory SEN is recommended.

Future work

- The casting VBA needs to be validated with experiment data.
- Preheating with insulation layer need to be simulated, and the effect of insulation layer in casting heat flux should be considered.
- Model domain can be extent to the mode.
- Heat flux boundary at centerline of SEN, and convection & conduction boundary conditions at inner side of mode could be considered, and compare with current model.

Nomenclature

Symbol	**Variable**	**Unit**
V	volume	m^3
t	time	s
Δt	time step	s
r	radius	m
r_w	west node radius	m
r_e	east node radius	m
Δr	neighbor node distance	m
Δr_{PE}	east side node distance	m
Δr_{PW}	west side node distance	m
T	temperature	℃
T_p^{n+1}	temperature of node p at new(n+1) time step	℃
T_p^n	temperature of node p at old (n) time step	℃
T_{gas}	inside gas temperature	℃
T_{air}	outside air temperature	℃
ρ	density	kg/m^3
C_p	specific heat	J/kg K
k	heat conductivity	W/m K
k_w	west side cell conductivity	W/m K
k_e	east side cell conductivity	W/m K
h_g	inside gas convective coefficient	W/m^2K
h_a	out air convective coefficient	W/m^2K

Reference

[D.1] K. Rackers, “Mechanism and Mitigation of Clogging in Continuous Casting Nozzles” (Masters Thesis, University of Illinois, 1995).

[D.2] J. Szekely and S.T. DiNovo, “Thermal Criteria for Tundish Nozzle or Taphole Blockage,” Metall. Trans., 5(March) (1974), 747-754.

[D.3] O. Araromi and B. G. Thomas, “Modeling of Clogging and Erosion of Nozzle Refractories in Steel Casting”, Materials Science and Technology Conference, Oct 25-29, 2009, Pittsburgh

[D.4] V. Singh and B.G. Thomas, “User-friendly Model of Heat Transfer in Submerged Entry Nozzles during Preheating, Cool down and Casting,” CCC meeting proceeding, (August) (2010) UIUC

[D.5] Yonghui Li, “Modeling Heat Transfer in SEN during Preheating & Cool-down”, CCC meeting proceeding, (August) (2012), UIUC

[D.6] K. Uemura et. al.: “Filtration Mechanism of Non-metallic Inclusions in Steel by Ceramic Loop Filter”, 1992, vol. 32 (1), pp. 150-156.

[D.7] Yonghui Li, Discretized governing equation in Yonghui’s VBA Model

[D.8] AG_DG thermal data_Feb 2011, Magnesita Refractories Research report

[D.9] Churchill,S.W., and H.H.S. Chu, Correlating Equations for Laminar and Turbulent Free Convection from a Vertical Flat Plate, Trans. ASME, 78,435,1956

[D.10] Singh, V. Flame Temperature Model, Master research, UIUC, 2010

Appendices

Temperature(degC)	Thermal conductivity(W/m K)	Specific Heat (J/kg K)
25	45.72	757
500	32.85	1330
750	23.99	1420
1000	15.13	1510

1500	12.90	1600

Table D.1 Alumina-Graphite33 properties [8] (2500 kg/m^3)

Temperature(degC)	Thermal conductivity(W/m K)	Specific Heat (J/kg K)
25	9.28	808
500	5.83	1170
750	5.48	1230
1000	5.13	1290
1500	5.14	1360

Table D.2 Dolomite-Graphite18 properties [8] (2460 kg/m^3)

Author's Biography

Yonghui Li was born on February 12, 1986 in Hebei, China. She obtained her Bachelor's degree in the Department of Nuclear Engineering at the Harbin Engineering University in 2008. After graduation, she continued her study in the Nuclear Engineering Department at Tsinghua University in Beijing. Then she continued her study in Nuclear, Plasma and Radiological Engineering Department (NPRE) at University of Illinois at Urbana-Champaign (UIUC). During August 2010 ~ May 2010, she worked as a teaching assistant in NPRE. After that, she obtained a research assistant position in Professor Brian G. Thomas' laboratory. Under the direction of Professor Thomas, she has worked on SEN heat transfer during preheating, cool-down and casting. She was a coop in SSAB R&D from January to May in 2013. During 2014 summer, she works as an intern in Vesuvius at Champaign. In August 2014, she will obtain his Master's degree in the Mechanical Engineering.